DAHLGREN DIVISION
NAVAL SURFACE WARFARE CENTER
Silver Spring, Maryland 20903-5640

NSWCDD/TR-94/20

FAR FIELD BOUNDARY CONDITIONS FOR UNDERWATER EXPLOSIONS

BY A. B. WARDLAW

SYSTEMS RESEARCH AND TECHNOLOGY DEPARTMENT

22 DECEMBER 1994

Report Documentation Page

Form Approved
OMB No. 0704-0188

1. REPORT DATE	2. REPORT TYPE	3. DATES COVERED
22 DEC 1994		**00-00-1994 to 00-00-1994**

4. TITLE AND SUBTITLE	5a. CONTRACT NUMBER
Far Field Boundary Conditions for Underwater Explosions	5b. GRANT NUMBER
	5c. PROGRAM ELEMENT NUMBER
6. AUTHOR(S)	5d. PROJECT NUMBER
	5e. TASK NUMBER
	5f. WORK UNIT NUMBER
7. PERFORMING ORGANIZATION NAME(S) AND ADDRESS(ES) **Dahlgren Division,Naval Surface Warfare Center,Silver Spring,MD,20903-5640**	8. PERFORMING ORGANIZATION REPORT NUMBER
9. SPONSORING/MONITORING AGENCY NAME(S) AND ADDRESS(ES)	10. SPONSOR/MONITOR'S ACRONYM(S)
	11. SPONSOR/MONITOR'S REPORT NUMBER(S)

12. DISTRIBUTION/AVAILABILITY STATEMENT
Approved for public release; distribution unlimited

13. SUPPLEMENTARY NOTES

14. ABSTRACT

15. SUBJECT TERMS

16. SECURITY CLASSIFICATION OF:			17. LIMITATION OF ABSTRACT	18. NUMBER OF PAGES	19a. NAME OF RESPONSIBLE PERSON
a. REPORT	b. ABSTRACT	c. THIS PAGE			
unclassified	**unclassified**	**unclassified**	**Same as Report (SAR)**	**94**	

FOREWORD

This report describes an enhancement to the DYSMAS/E hydrocode which provides an improved capability to simulate nonreflective boundary conditions. These conditions, which minimize the disturbance created by the exiting of the explosive shock from the computational domain, allow the DYSMAS/E code to be operated using a smaller mesh. Such a capability should be of particular importance in reducing the computational requirements for a 3–D simulation.

This work was supported by Dale Houser of the Office of Naval Research, through the Explosives and Undersea Warheads Technology Program, mangaged by C. Dickinson of the Naval Surface Warfare Center, White Oak. The author expresses his appreciation to these individuals for their support.

Approved by:

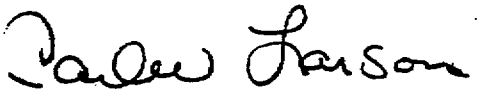

CARL LARSON, Division Head
System Research &Technology Division

CONTENTS

ILLUSTRATIONS

ILLUSTRATIONS (CONTINUED)

ILLUSTRATIONS (CONTINUED)

ILLUSTRATIONS (CONTINUED)

ILLUSTRATIONS (CONTINUED)

TABLES

CHAPTER 1
INTRODUCTION

A factor controlling the computational resources required to model an underwater explosion is the extent of the mesh. Generally, the outer boundary of the computational domain is located sufficiently far from the explosive to prevent the initial explosion shock from reflecting off of the boundary and arriving back at the vicinity of the explosion prior to the end of the computation. Due to the relatively high speed of sound in water and the long time scale of some of the phenomena of interest, such as bubble pulsing, the necessary mesh domain can be very large. The issue of mesh sizing is particularly acute in three dimensions where even a nominal mesh size in each direction can create a problem with taxing computational requirements. One method of reducing the size of the computational mesh is to employ far field boundary conditions which do not reflect incidence shocks. This would allow the outer boundaries to be placed closer to the explosion, reducing the extent of the mesh in each direction.

An examination of the literature for nonreflective boundary conditions (also termed nontransmissive, radiating, and absorbing) indicates that this is a recurring problem which is of interest to many fields. A recent review of the subject is provided by Givoli.[1] Literally speaking, a nonreflecting boundary condition (NRBC) allows shocks and other disturbances to pass out of the boundary of the computational domain without producing spurious reflections. Such boundary conditions can be constructed for some problems of interest; for example, a planar shock. However, it fails under circumstances where the outgoing shock or wave creates an incoming disturbance.[2,3] Additionally, NRBC are inappropriate when outgoing disturbances interact mutually after leaving the computational domain and produce a reflection which is incident on the computational domain.[1]

The implicit requirement underlying the application of NRBC is the absence of information propagating into the computational domain at the nonreflecting boundary. However, as pointed out by Thompson,[2,3] this is not the case for a spherical explosion, the problem of primary interest in this report. Here the spherical structure of the shock requires that waves pass into and out of any spherical surface inside the shock and imposition of a true NRBC will produce unsatisfactory results.[2,3,4] The objective of this study then, is to develop far field boundary condition (FFBC) which allows the computational domain to be truncated without introducing unacceptable errors into the solution.

Development of the FFBC is based on characteristics, such as that in References 2 and 3. For nonlinear, hyperbolic problems which are of interest, signals travel along characteristic surfaces in known directions and the correct formulation of any type of boundary condition consists of replacing characteristics which emanate from outside the computational domain with an appropriate constraint. In the case of a FFBC, the constraint defines the incoming

wave properties which are usually unknown and vary with different problems. For some problems there are no incoming waves while in others, such waves must be approximated or estimated using an asymptotic solution[5] or heuristics.

The objective of this work is to develop and validate FFBC for the DYSMAS/E code.[6,7] The characteristic analysis necessary for formulating the FFBC is developed in Chapter 2, while Chapter 3 discusses its specialization to far field boundaries, and Chapter 4 outlines the numerical implementation for the DYSMAS/E algorithm. One-dimensional results are given in Chapter 5 while the application to multiple dimensions is discussed in Chapter 6. Appendices A and B provide user instructions and a description of the code changes necessary to implement the FFBC in DYSMAS/E. Numerical experiments with different types of meshes are reviewed in Appendix C.

CHAPTER 2
1–D CHARACTERISTIC ANALYSIS

The analysis is restricted to 1–D and includes the influence of gravity, g. The conservation equations are:

$$\mathrm{I}\frac{\partial q}{\partial t}+\mathrm{B}\frac{\partial q}{\partial r}=\mathrm{C} \tag{1}$$

where:

$$q=\begin{bmatrix}\rho\\ u\\ s\end{bmatrix};\ \mathrm{B}=\begin{bmatrix}u & \rho & 0\\ \frac{c^2}{\rho} & u & \frac{K_1}{\rho}\\ 0 & 0 & u\end{bmatrix};\ \mathrm{C}=\begin{bmatrix}-\frac{n\rho u}{r}\\ g\\ 0\end{bmatrix} \tag{2}$$

with $K_1 = (\partial p/\partial s)_\rho$, and n = 0, 1, 2 for planar, cylindrical and spherical coordinates respectively. Here the energy equation is replaced by the equivalent statement that entropy is constant along streamlines. Finding the eigenvalues and left eigenvectors of:

$$[\lambda\mathrm{I}-\mathrm{B}]=0 \tag{3}$$

yields:

$$\begin{aligned}&\lambda_o = u; \qquad \mathrm{l}_o = (0,\ 0,\ 1)\\ &\lambda_+ = (u+c);\ \mathrm{l}_+ = \left(c,\ \rho,\ \frac{K_1}{c}\right)\\ &\lambda_- = (u-c);\ \mathrm{l}_- = \left(-c,\ \rho,\ -\frac{K_1}{c}\right)\end{aligned} \tag{4}$$

The characteristic equations arise by multiplying Equation (1) by l_n and using $\mathrm{l}_n\mathrm{B} = \lambda_n\mathrm{l}_n$ which yields:

$$\mathrm{l}_n\left[\frac{\partial q}{\partial t}+\lambda_n\frac{\partial q}{\partial r}\right]=\mathrm{l}_n\mathrm{C}. \tag{5}$$

Evaluating this equation for each pair of $(\mathrm{l}_n, \lambda_n)$ results in the characteristic equations:

$$\left[\frac{\partial p}{\partial t}-\rho c\frac{\partial u}{\partial t}\right]+\lambda_-\left[\frac{\partial p}{\partial r}-\rho c\frac{\partial u}{\partial r}\right]=-\frac{n\rho uc^2}{r}-c\rho g \tag{6}$$

$$\left[\frac{\partial s}{\partial t}\right]+\lambda_o\left[\frac{\partial s}{\partial r}\right]=0 \tag{7}$$

$$\left[\frac{\partial p}{\partial t}+\rho c\frac{\partial u}{\partial t}\right]+\lambda_+\left[\frac{\partial p}{\partial r}+\rho c\frac{\partial u}{\partial r}\right]=-\frac{n\rho uc^2}{r}+c\rho g \tag{8}$$

Figure 1 illustrates the direction of applicability of each of these characteristic relations. Note that if a far field boundary is located at $\mathrm{r_r}$, where the computational domain consists of $\mathrm{r_l} \le \mathrm{r} \le \mathrm{r_r}$, Equation (6) must be modified to account for the absence of information outside of the computational domain.

CHAPTER 3
FAR FIELD BOUNDARY CONDITIONS FOR 1–D FLOWS

Equations (6), (7) and (8) can be used to advance the flow properties at points interior to the computational domain. To accomplish this, these equations are written in the form:

$$\left[\frac{\partial p}{\partial t} - \rho c \frac{\partial u}{\partial t}\right] = Q_- - c\rho g \tag{9}$$

$$\left[\frac{\partial s}{\partial t}\right] = Q_o \tag{10}$$

$$\left[\frac{\partial p}{\partial t} + \rho c \frac{\partial u}{\partial t}\right] = Q_+ + c\rho g \tag{11}$$

where:

$$Q_- = -\lambda_- \left[\frac{\partial p}{\partial r} - \rho c \frac{\partial u}{\partial r}\right] - \frac{n\rho u c^2}{r} \tag{12}$$

$$Q_o = -\lambda_o \left[\frac{\partial s}{\partial r}\right] \tag{13}$$

$$Q_+ = -\lambda_+ \left[\frac{\partial p}{\partial r} + \rho c \frac{\partial u}{\partial r}\right] - \frac{n\rho u c^2}{r} \tag{14}$$

Simultaneous solutions of Equations (9) to (11), using Equations (12), (13) and (14) to evaluate the right hand sides, produces $\frac{\partial p}{\partial t}$, $\frac{\partial u}{\partial t}$ *and* $\frac{\partial s}{\partial t}$ which can be used to update p, u, s and hence the flow field. Each characteristic is associated with the particular direction given in Figure 1 and it is necessary to respect that direction when evaluating the r derivatives of the related Q. Otherwise, information is being taken from the wrong direction and the calculation is likely to be unstable. A first order evaluation of the r derivatives results in the following expressions:

$$Q_- = -\frac{n\rho_i u_i c_i^2}{r_i} + \frac{(p_{i+1} - p_i)}{(r_{i+1} - r_i)} - \rho c \frac{(u_{i+1} - u_i)}{(r_{i+1} - r_i)} \tag{15}$$

$$Q_o = \begin{cases} \frac{s_i - s_{i-1}}{r_i - r_{i-1}} & u > 0 \\ \frac{s_{i+1} - s_i}{r_{i+1} - r_i} & u \leq 0 \end{cases} \tag{16}$$

$$Q_+ = -\frac{n\rho_i u_i c_i^2}{r_i} + \frac{(p_i - p_{i-1})}{(r_i - r_{i-1})} + \rho c \frac{(u_i - u_{i-1})}{(r_i - r_{i-1})} \tag{17}$$

At any boundary, the characteristic relations originating outside of the computational domain can not be evaluated; there is no information at i+1 to compute the r derivative with.

This relation must be replaced with another constraint. In the case of flow against a solid wall, the characteristic relation originating outside of the computational domain is replaced with the u = 0 constraint. At a far field boundary, one or more of Equations (9) to (11) may be invalid. The number of invalid equations is determined by the velocity and speed of sound at the boundary. As is indicated in Figure 1, the orientation of the characteristics changes as these parameters vary. If the computational domain is the interval $r_l \le r \le r_r$, then the possibilities are as follows:

1. Supersonic outflow
   a. at r_r: ($u > c$), all equations are valid;
   b. at r_l: ($-c > u$), all equations valid.
2. Subsonic outflow
   a. at r_r: ($c \ge u > 0$), Equation (9) invalid;
   b. at r_l: ($0 \ge u > -c$), Equation (11) invalid.
3. Subsonic inflow:
   a. at r_r: ($0 \ge u > -c$), Equations (9) and (10) invalid;
   b. at r_l: ($c \ge u > 0$), Equations (10) and (11) invalid;
4. Supersonic inflow:
   a. at r_r: ($-c \ge u$), Equations (9), (10) and (11) are invalid;
   b. at r_l: ($u \ge c$), Equation (9), (10) and (11) invalid;

Far field boundaries are distant enough from the explosion to preclude supersonic flow and hence the situation of interest is subsonic outflow or inflow. These cases require the replacement of either one and two characteristic relations.

By definition, a truly non-reflecting boundary condition presumes that the incoming wave amplitude is zero.[5] This assumption implies that for outflow:

$$\begin{aligned} at\ r_r: &\ \left[\frac{\partial p}{\partial r} - \rho c \frac{\partial u}{\partial r}\right] = 0 \\ at\ r_l: &\ \left[\frac{\partial p}{\partial r} + \rho c \frac{\partial u}{\partial r}\right] = 0 \end{aligned} \tag{18}$$

which reduces $Q_{\pm}$ to:

$$\begin{aligned} at\ r_r: &\ Q_- = \frac{-n\rho c^2 u}{r} \\ at\ r_l: &\ Q_+ = \frac{-n\rho c^2 u}{r} \end{aligned} \tag{19}$$

This condition is likely to be fulfilled only under very special circumstances such as a uniform, gravity free flow, (n =0, g=0). The spherical explosion case features varying conditions behind the shock and does not satisfy this constraint. Under these circumstances, a replacement to Equation (9) must be constructed by other means. In the case of inflow,

Equation (10) is also invalid. This poses less of a problem since the flow is nearly isentropic at a far field boundary which implies $Q_o \simeq constant$.

Hagstrom and Harigan[5] have constructed asymptotic approximations to the deleted portion of the flow field which resides outside of the far field boundary. In particular, three different solutions are obtained which provide the following definitions for the Q value associated with the invalid equation:

$$Q_{\pm} = -\frac{\rho c c_{\infty} u}{R} \tag{20}$$

$$Q_{\pm} = -\frac{\rho c c_{\infty} \overline{c}}{R} ln\left(\frac{\rho}{\rho_{\infty}}\right) \tag{21}$$

$$Q_{\pm} = -\frac{\rho c c_{\infty}}{2R}\left(u + \overline{c} ln\left(\frac{\rho}{\rho_{\infty}}\right)\right) \tag{22}$$

To arrive at Equation (21) and (22), from the form given by Reference 5, the following approximation has been introduced:

$$\int_{\rho_{\infty}}^{\rho} \frac{c d\rho}{\rho} = \overline{c}\, ln\left(\frac{\rho}{\rho_{\infty}}\right) \tag{23}$$

These solutions assume isentropic flow and an outward moving shock.

Note that Equations (20), (21) and (22) can be written as:

$$Q_{\pm} = k\frac{\rho c c_{\infty}}{R} U \tag{24}$$

where k is an adjustable constant and U alternately takes the form u, $\overline{c}\, ln(\rho/\rho_{\infty})$, and $.5(u + \overline{c}\, ln(\rho/\rho_{\infty}))$. This form is similar to that of Equation (19) with k set to $-$n and c *to* c_{∞}.

CHAPTER 4
NUMERICAL IMPLEMENTATION

1-D IMPLEMENTATION

A special solution is constructed for the cells lying on the far field boundaries using Equations (9) and (11). Here the flow is assumed to be isentropic which removes the necessity of satisfying Equation (10). Simultaneous solution of Equations (9) and (11) produces:

$$\frac{\partial p}{\partial t} = \frac{(Q_+ + Q_-)}{2} \tag{25}$$

$$\frac{\partial u}{\partial t} = \frac{(Q_+ - Q_-)}{2\rho c} + g \tag{26}$$

which allows p and u to be advanced. At the r_l and r_r boundaries, Q_+ and Q_- respectively, are evaluated from an empirical expression constructed from Equation (24):

$$Q_\pm = k_t \frac{\rho c^2}{R}\left(k_u u + (1-k_u) c\, ln\left(\frac{\rho}{\rho_\infty}\right)\right). \tag{27}$$

Here k_t *and* k_u are adjustable parameters. The Q_- and Q_+ associated with the valid characteristic at the r_l and r_r boundaries, respectively, are computed from:

$$Q_\pm = -\lambda_\pm\left[\frac{\partial p}{\partial r} \pm \rho c \frac{\partial u}{\partial r}\right] - \frac{k_c \rho u c^2}{r} \tag{28}$$

Here k_c is an adjustable parameter which would normally have a value of 0, –1 and –2 in Cartesian, cylindrical and spherical meshes. This parameter is introduced to allow tuning the results in multi-dimensional problems.

Use of the isentropic condition in combination with the sound speed defines the change in ρ, $d\rho = dp/c^2$ while first law of thermodynamics, $Tds = de - (p/\rho^2)d\rho = 0$, specifies the change in e. The final scheme for advancing the boundary points thus becomes:

$$\begin{aligned}
p^{n+1} &= p^n + \frac{(Q_+^n + Q_-^n)}{2}\Delta t^n \\
u^{n+1} &= u^n + \frac{(Q_+^n - Q_-^n)}{2\rho^n c^n}\Delta t^n + g\Delta t^n \\
\rho^{n+1} &= \rho^n + \frac{(p^{n+1} - p^n)}{(c^n)^2} \\
e^{n+1} &= e^n + 2\frac{(p^{n+1} + p^n)}{(\rho^{n+1} + \rho^n)^2}(\rho^{n+1} - \rho^n)
\end{aligned} \tag{29}$$

Alternatively, if entropy changes were included, Equations (25) and (26) would be solved in combination with Equation(10) to produce the new values of p, u and s. Using p and s, the values of e and ρ can be determined from the equation of state.

Equations (29) are implemented at boundary points prior to executing each computational step. The computational step is then completed at all points using the standard algorithm which includes zero order extrapolation at the boundary points. After the completion of the step, the results from Equations (29) are used to overwrite the boundary values.

CHAPTER 5
NUMERICAL EXPERIMENTS IN 1–D

The above boundary conditions have been implemented in the DYSMAS/E code.[6] Attention is focused on three different types of cases. The first are the truly nonreflective examples where the amplitude of the incoming waves is zero. Here, with the appropriate choice of constants, good results are expected. The second two examples deal with the spherical explosions where the amplitude of the incoming waves is not zero. For these cases numerical experiments will be conducted to determine the choice of constants in Equation (27) which gives the best results. Two different types of problems are considered: a short time scale problem of an exiting shock and a long time scale problem which terminates following the first bubble minimum.

NONREFLECTING CASE

A planar Riemann problem is considered which consists of two initial states featuring different pressure, density and energy. For simplicity, the velocity is assumed to be zero. The parameters k_t, k_u *and* k_c are set to zero. The first three Riemann problems feature water only and differ by the extent of the property jumps between the two initial states. Results for these cases are given in Figures 2, 3 and 4 which feature pressure ratios between the two initial states of 6.82:1, 62.9:1 and 175:1, respectively. In each problem a shock propagates to the right and an expansion to the left. The nonreflecting boundary conditions should allow these waves to exit from the computational domain leaving the constant middle state to the Riemann problem covering the computational domain. An examination of these figures indicates that this is nominally true, although a distortion of the final profile is visible in Figure 3, which featured the largest jump between the two initial states.

The final Riemann problem considered is shown in Figure 5 and consists of TNT and water initial states with a pressure ratio of 7225:1. The water is located on the right side of the figure and air at the left. A significant error is induced by the shock as it exits the right boundary while the correct constant condition is recovered at the left boundary as the expansion exits the left side of the computational domain.

The results achieved with these nonreflecting cases are in good agreement with the actual solution, provided that the strength of the exiting shock is not too large. Errors for strong shocks likely arise from several sources. As derived above, the FFBC assume isentropic flow which is not realistic in these situations. Also, the shock profile contains spurious oscillations which may contaminate the outflow solution. Numerical experiments indicate that increases in the DYSMAS/E FCT parameter values which reduce these oscillations also reduce the FFBC error.

SPHERICAL SHOCKS

The explosion of a spherical TNT charge in a uniform water environment is modeled in spherical coordinates. The TNT is described using a JWL equation of state while the water is modeled using a modified Tait equation of state.[6] The TNT is assumed to combust instantaneously and the initial state corresponds to an energy of $4.2814(10^{10})$ ergs/gm and density of 1.63 gm/cc.

The spherical explosion problem does not give rise to a nonreflecting boundary and it is necessary to prescribe the incoming information along the characteristic which originates outside of the computational domain. This is accomplished using Equation (27). The task here is to select optimum values for the two parameters in this equation, k_t *and* k_u. The value of k_c was fixed at -2. To accomplish this, tests were conducted on a trial, uniform mesh with 300 points. These results were compared to a reference solution on a stretched mesh with 1000 points. The outer boundary of the reference mesh was far enough from the explosion to avoid being influenced of the explosion. The pressure and impulse time history for a point on the trial mesh is compared to the reference mesh results using difference values of k_t *and* k_u.

Figures 6 to 11 contain the results of the comparisons between the trial and reference mesh results for k_u values of 0, .5 and 1, respectively. Each figure considers a specific point and illustrates the influence on pressure and impulse of varying k_t . Figures 6 to 8 provide results for a depth of 103.66m while Figures 9 to 11 illustrate the solutions at 15.26m. In each figure the reference solution produces a pressure trace which decays smoothly from the peak value produced by the passing initial explosion shock. The trial pressure trace deviates from the reference trace near 17 msecs, denoting the arrival of the disturbance created when the explosion shock reached the mesh boundary. For $k_u = 1$, this initial discrepancy can be minimized by selecting $k_t = .5$; however, this depresses pressures at t > 30 msec. This under-prediction at longer times results in larger impulse errors. On the other hand, at $k_u = 0$, the trial pressure trace closely matches the reference value at $k_t = 1$.

To test the general effectiveness of the values, $k_t = 1$, $k_u = 0$, two additional test series have been conducted. In the first, the trial meshes are expanded to included the sizes 200, 400, and 500, while the points selected for comparison are increased to 6. Results are shown in Figures 12 to 16 for points 50, 100, 200, 300, and 400, respectively, at the depths of 15.24m and 103.6m. An examination of these results indicates that there is no discernible difference between the pressures and impulses on the trial and reference meshes.

The second series was accomplished on a series of four stretched meshes and consists of computations at 15.24m and 103.6m. The largest mesh served as a reference mesh while the other three are truncated versions of it which allowed the disturbance created by the shock at the outer boundary to reach test points prior to the end of the calculation. Results are presented in Figures 17 and 18 for trial grid points 40 and 80. Deviation between the trial and reference pressures are visible on the smallest mesh, grid A, when the shock disturbance first reaches the test points. However, this discrepancy disappears quickly. The disagreement between grids B and C results and those on the reference mesh, grid D, are very insignificant. A description of the four meshes used in Figures 17 and 18 is given in Table 1.

The tests conducted in this section indicate that use of Equation. (27) with $k_t = 1$, $k_u = 0$, yields a FFBC which introduces minimal errors into calculation containing an exiting spherical shock. In the case of a uniform mesh, significant distortions are eliminated. The errors introduced by the FFBC are visible on grid A of the stretched mesh case. However, this mesh was very small and the distortion in the pressure was mainly visible immediately following the arrival the reflected disturbance created at the outer boundary by the outgoing shock.

PULSATING BUBBLE

The final class of problem is the pulsating bubble which has a time duration greatly in excess of the shock problem. As in the preceding section, this problem is initiated by a spherical explosion. However, the focus is on later times, long after the shock has exited from the computational domain. The bubble created by the explosion expands and eventually contracts, forming a new bubble minimum. The expansion-contraction process continues for additional cycles with diminishing changes in the bubble radius.

The pulsating bubble is a case which does not admit a truly nonreflecting boundary condition and it is necessary to prescribe the missing characteristic information at the outflow boundary. However, this problem is more difficult than the explosion shock; during the expansion part of the cycle the flow is out of the computational domain, while during the contraction phase it is inwards. Furthermore, the longer duration of the problem provides an extended period for boundary error build up.

To test the and tune the FFBC, six cases have been constructed featuring different depths (15.24m and 103.6m) and bubble periods (~.150 second and ~.350 second). For each case a series of four meshes was constructed, the largest of which placed the boundary far enough away to prevent the reflected disturbance from the exiting shock from arriving back until late in the problem. This mesh serves as the reference mesh, while the remaining three meshes constituted the trial cases.

The bubble radius histories for these six cases are given in Figures 19 to 24, along with pressure and impulse histories at two points near the bubble. In addition, Tables 2 to 5 provide the detailed definition of each mesh sequence. The right hand columns in these tables indicates the ratio of the time required for the shock to reach the edge of the computational mesh to the length of the bubble pulse. For values of this ratio less than .5, the exiting shock disturbance has time to reflect back to the bubble and influence the calculation during the first bubble pulse. Successful performance of the FFBC if thus associated with a bubble radius history which is invariant to changes with mesh size.

A comparison of the results exhibited in Figures 19 to 24 are mixed. For the short duration case at the 103.6m depth (Figure 19), excellent performance of the FFBC is evident. This performance degrades with longer periods and decreasing depth as shown in Figure 23. It is hypothesized that this decrease in performance is attributable to two factors. At shallower depths the ratio of the explosive initial pressure to the ambient water pressure is greater which produces a stronger exiting shock. At the far field boundary, the exiting shock at 15.24m

is ~5 times stronger than that at 103.6m. Here the strength of the shock is taken to be the ratio of the pressure jump across the shock.

The longer period calculations require a larger number of integration steps, enhancing the opportunity for error buildup. To check the influence of the number of integration steps on the performance of the FFBC, the long period runs at 15.24m and 103.6m have been repeated on a coarser mesh, which decreases the number of integrations steps. As can be seen by comparing Figures 20 and 21 and Figures 23 and 24, the error on the coarser mesh is reduced noticeably in both cases.

CHAPTER 6
EXTENSION TO MULTIPLE DIMENSIONS

APPROACH

Two different approaches are considered for extending the previous developed 1–D FFBC to two- and three-dimensions. The simplest is to apply the previously developed 1–D analysis to multiply dimensioned cases. The assumption here is that the flow components tangent to the far field boundary can neglected. An alternative is to include the difference terms associated with the tangential components. This leads to a more complete method, but one with additional complexity and one which requires additional far field boundary information in the case of subsonic inflow. For 2–D subsonic inflow, assuming isentropic flow as was done in the 1–D case, two characteristic relations must be replaced with empirical relations. If the isentropic assumption is dropped, three relations are necessary. Moving to the 3–D case adds an additional invalid characteristic relation. The new characteristic relations which must be replaced in multidimensional flow concern the derivatives of the tangent velocity components.

The main disadvantage to applying the 1–D FFBC to multiple dimensions is the loss of the ability to treat the truly nonreflective case. A planar, constant strength shock moving obliquely through a three dimensional Cartesian mesh is an example of such a situation. However, this type of problem is not of particular interest here.

The approach taken here is to apply the 1–D FFBC to two and three dimensional problems. Test cases, similar to those used in the 1–D situation, are used to select appropriate values of k_t *and* k_u for two and three dimensional problems. Attention is restricted to the shock and bubble pulse problems which were examined in the 1–D case. Where possible, the same mesh applied in 1–D is applied to each of the dimensions of the multidimensional problem. The parameter k_c which appears in Equation (28) is set at -2, the value associated with spherical symmetry. The purpose of using this value is to capture the spherical symmetry associated with explosion problems on other types of meshes. Numerical experiments suggest that k_c has little influence on the performance of FFBC.

SPHERICAL SHOCK IN 2–D (CYLINDRICAL COORDINATES)

The optimum values for k_t *and* k_u are selected by conducting numerical experiments on a trial, uniform mesh with 200X200 points. These results were compared to a reference solution on a stretched mesh with 400X400 points. The outer boundary of the reference mesh was located far enough from the explosion to avoid being influenced of the explosion shock prior to the end of the computation. To minimize the extent of the meshes in these calculations, symmetry is assumed about the y=0 plane, and the wall boundary condition is applied here.

The pressure and impulse history for points on the trial mesh are compared to the reference mesh results for different values of k_t *and* k_u in Figures 25 to 28. An examination of these figures indicates that best results are obtained for $k_t = .875$ *and* $k_u = 0$.

To gain a broader view of the merits of this boundary condition in uniform flow, the FFBC is to trial meshes with $k_t = .875$ *and* $k_u = 0$. The trial meshes were uniform with 200X200, 300X300 and 400X400 cells while the reference mesh contained 400X400 stretched cells. Pressure and impulse histories on the trial meshes are compared to the reference results in Figures 29 to 32. Small deviations in the computed pressure are visible in each case following the arrival of the reflected disturbance from the exiting shock. In all cases the reference and trial impulses are very close to one another.

The final 2–D shock example uses a sequence of four stretched meshes. The mesh point distribution in each direction corresponds to those shown in Table 1, for the 1–D case, with the finest mesh serving as the reference mesh. The results for this case are shown at the depths of 301.6m and 15.24m in Figures 33, 34, and 35, covering mesh points (40,1), (80,1), and (100,1), respectively. The trial radius, pressure and impulse histories are not distinguishable from the reference trace except on the smallest mesh where small excursions can be seen.

The 2–D shock examples demonstrate excellent performance of the FFBC for the cylindrically symmetric case. The uniform mesh results are not quite as good as in the 1–D case; however, comparable performance is seen in the stretched mesh example (see Figures 17, 18, 33 and 34).

PULSATING BUBBLE IN 2–D (CYLINDRICAL COORDINATES)

To test the FFBC for the 2–D pulsating bubble, four of the cases completed in the 1–D tests have been revisited. The bubble radius history for these six cases are given in Figures 36 to 39, along with pressure and impulse histories at two points near the bubble. Tables 2 to 5 provide the detailed definition of each mesh sequences used in each case. The same point distribution was used in each direction and a symmetry plane was located at the x=0 and y=0 planes.

The final case considered includes the influence of gravity and features the application of the FFBC at the side boundaries. The radial mesh sequence used is shown in Table 2 while the vertical mesh is fixed. It consists of solid wall conditions above and below the computational domain and contains the three block of 91, 39 and 43 cells, with stretching ratios of 1.0, 1.02 and 1.14 respectively. The bottom wall condition prevents a downward flow of the fluid due to the hydrostatic pressure while the top wall simulates an obstacle. The results of this calculation are shown in Figure 40 for a deep, short period explosion bubble. Good agreement is obtained among calculations on all four meshes, similar to that achieved in Figure 36 for the radially symmetric, 2–D bubble.

In general, the FFBC applied to the 2–D pulsating bubble exhibits improved performance over the 1–D case. In the 2–D situation, the explosion shock does not arrive simultaneously at the boundaries which are located at varying distances from the explosion. Additionally, the boundaries are generally not perpendicular to the mesh, which prevents the shock, when it arrives at the far field boundary, from being reflected back to the bubble.

SPHERICAL SHOCK IN 3–D (CARTESIAN COORDINATES)

The performance of the FFBC is tested in three dimensions using a 61X61X61 uniform mesh. The mesh size and cell distribution in each direction is the same as that used in 1–D and 2–D (see Mesh A in Figures 17, 18, 34 and 35). Due to the computational resources required for 3–D calculations, the results are limited to this case.

An investigation of the influence of k_t has been carried out and results are shown in Figures 41 and 42 at depths of 15.24m and 103.6m, respectively. Based on the experience in the 1–D and 2–D cases k_u is fixed at 0. The reference curve in these figures is taken from the 2–D reference results of Figures 25 to 28. An examination of these curves indicates an optimal value of $k_t = .5$. For this k_t setting, the agreement between the trial and reference curve is similar to that obtained in the 1–D and 2–D cases.

CHAPTER 7
SUMMARY AND CONCLUSIONS

This report has investigated a far field boundary condition (FFBC) designed to suppress reflections from the exiting waves, including shocks and expansions, in the case of a spherical explosion. Under such circumstances, the outgoing wave generates an incoming wave and the task of creating a far field boundary condition reduces to constructing an empirical method to supply the missing incoming wave information. The general form for this condition is based on characteristic analysis and uses a nonreflecting formulation and asymptotic analysis to derive a general equation which contains adjustable parameters (see Equations (27) and (28)). This approach has been implemented in the DYSMAS/E hydrocode and the adjustable parameters have been determined by numerical experiments in one, two and three dimensions. Optimal values of these parameters are shown in Table 6. The resulting formulation is applied to the spherical shock problem in one and multiple dimensions. In the latter case, flow tangent to the far field boundaries is neglected, and the 1–D analysis is applied at the boundaries. The performance of this method is assessed for the short term shock phase and for the long term pulsating bubble problem.

For the short-term shock problem, the far field boundary condition yielded excellent results. This was determined by comparing pressure and impulse histories at selected points on meshes of varying size. The computations performed on the largest mesh placed the boundary far enough from the explosion to eliminate the boundary effect. The results of these comparisons are shown Figures 12 to 18, 29 to 35, 42, and 43.

Within the DYSMAS/E hydrocode, the alternatives to the far field boundary conditions are reflection (wall), nonreflection with damping and nonreflection without damping. The consequences of applying these conditions are illustrated in Figure 43 while the FFBC results for the same problem are shown in Figure 18. As anticipated, the reflection boundary condition strongly reflects the shock and produces distortions which overwhelm the desired decaying pressure profiles. The nonreflection option without damping results in an underprediction of the pressure following the arrival of the disturbance from the exiting shock. Inclusion of damping highly distorts the pressure traces and in many cases produces results similar to those associated with the wall boundary conditions. These results indicate that the new far field boundary condition represents an enhancement over existing DYSMAS/E options. The FFBC minimizes the error introduced by shock reflection at the outer boundary.

In the case of the long term pulsating bubble, results were mixed. The FFBC performed well for deep explosions with short periods (Figure 19). At shallow depths and for cases with a longer period (Figure 21), the accuracy of the FFBC decreases. Under these conditions, more integration steps were required and it is hypothesized that this increases the opportunity for error buildup at the far field boundaries. Decreasing the depth increases the strength of the

explosion shock (i.e. pressure jump across the shock) which increases the far field boundary condition error. Similar FFBC performance trends were evident in 2–D, Figures 35 to 38; however, the results were generally better. This improvement can likely be traced to the fact that in 2–D, the waves generated by the explosion bubble, including the shock, do not arrive at boundaries simultaneously and are not all reflected back to the bubble.

Figures 43 illustrates application of existing DYSMAS/E boundary conditions to the deep, short bubble problem, while the FFBC results for the same case are given in Figure 19. The new FFBC clearly offers improved performance in this case. However, as is illustrated by comparing Figure 44 to Figures 20 and 22, degradation in performance of the FFBC at small depths and for problems with an extended bubble period yields results which are similar in quality to the existing DYSMAS/E nonreflecting, damped boundary condition.

An alternative strategy for minimizing mesh size is the use a highly stretched mesh near the outer boundary. This approach, which is examined in Appendix C, yields results which degrade as the maximum mesh stretching ratio increases. In particular, the bubble period and peak pulse pressures are impacted. Accordingly, minimizing the mesh size for a bubble pulse problem requires use of the FFBC applied to a judiciously truncated mesh, as well as the selection of a mesh with a stretching factor not exceeding 1.15. The results of Figures 19 to 24 and 36 to 40 serve as a guide for selecting the mesh trunctation.

REFERENCES

1. Givoli, Dan, "Non-Reflecting Boundary Conditions", JCP , 94, 1, 1991.
2. Thompson, K. W., "Time Dependent Boundary Conditions for Hyperbolic Systems". JCP, 68, pp 1–24, 1987.
3. Thompson, K. W., "Time Dependent Boundary Conditions for Hyperbolic Systems, II". JCP, 98, pp 439–461, 1989.
4. Hagstrom, T., and Hariharan, S. I., "Accurate Boundary Conditions for Exterior Problems in Gas Dynamics", Math. Comp., 51, 184, pp 581–597, October, 1988.
5. G. W. Hedstrom, "Nonreflecting Boundary Conditions for Nonlinear Hyperbolic Systems", JCP, 30, 222, 1979.
6. "DYSMAS/E Theoretical Manual" IABG, March 1990.
7. "DYSMAS/E Input Manual" , IABG, March 1990.

GLOSSARY

c — speed of sound
g — acceleration due to gravity
k_c — adjustable constant in Equation (28).
k_t and k_u — adjustable constants in Equation (27)
K_1 — $\left(\frac{\partial p}{\partial s}\right)_\rho$
I — $\int_0^t p \, d\tau$
l — left eigenvectors
p — pressure
r — spherical radius
r,z — cylindrical coordinates
s — entropy
t — time
x,y,z — Cartesian coordinates
Ti — Time at which the disturbance created by exiting shock to arrives back at the explosion bubble.
Tr — Time required for the shock to reach the far field boundary.
Tp — length of the bubble period
Tt — length of the computation
u — velocity in the r or x direction
λ — eigenvalue
ρ — density

subscripts

i — cell index
o — associated with the central (streamline) characteristic
+ — associated with the right running characteristic
− — associated with the left running characteristic
∞ — ambient condition

superscripts

n — step number
— — average value

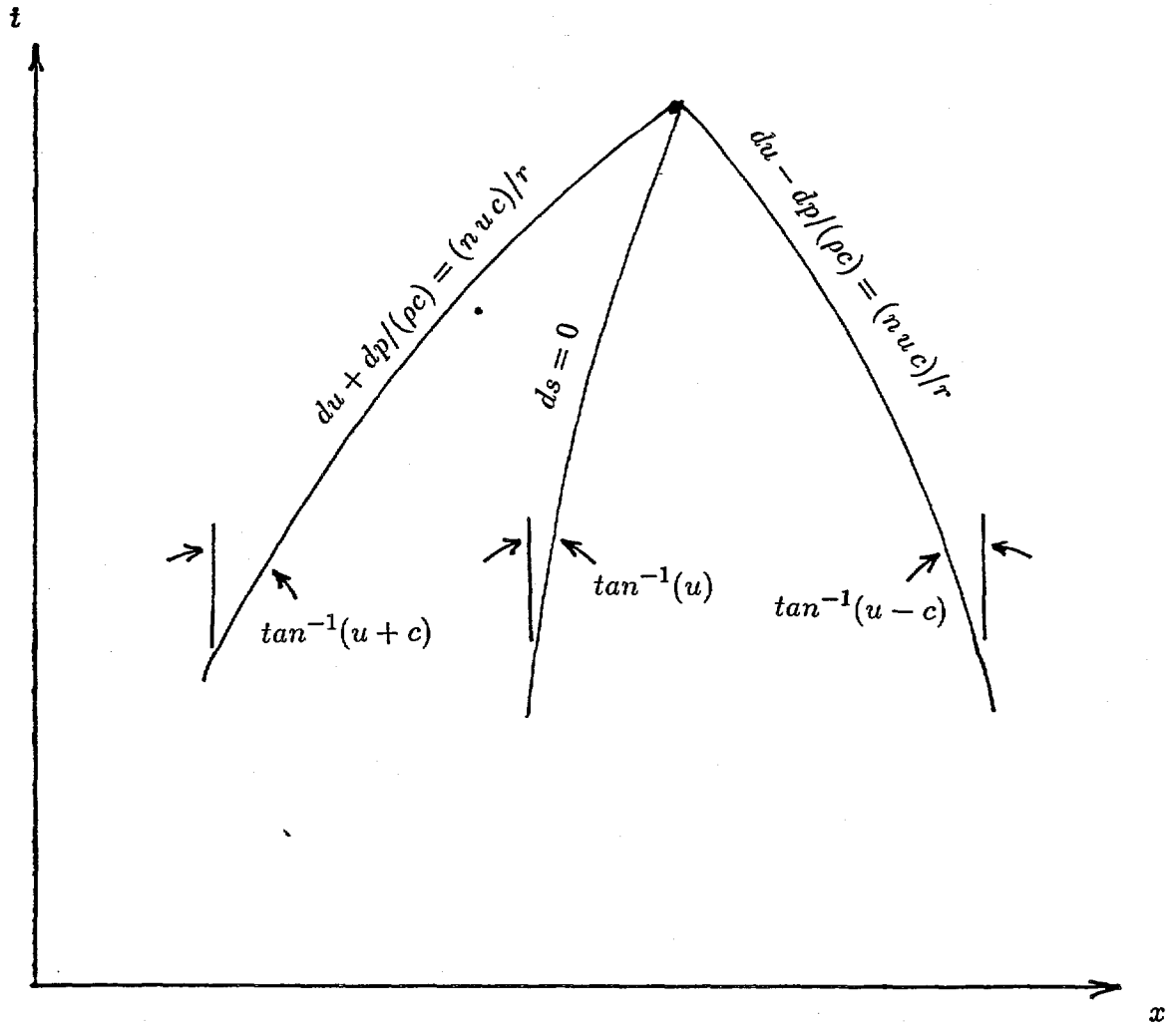

FIGURE 1. 1–D CHARACTERISTIC EQUATIONS AND DIRECTIONS

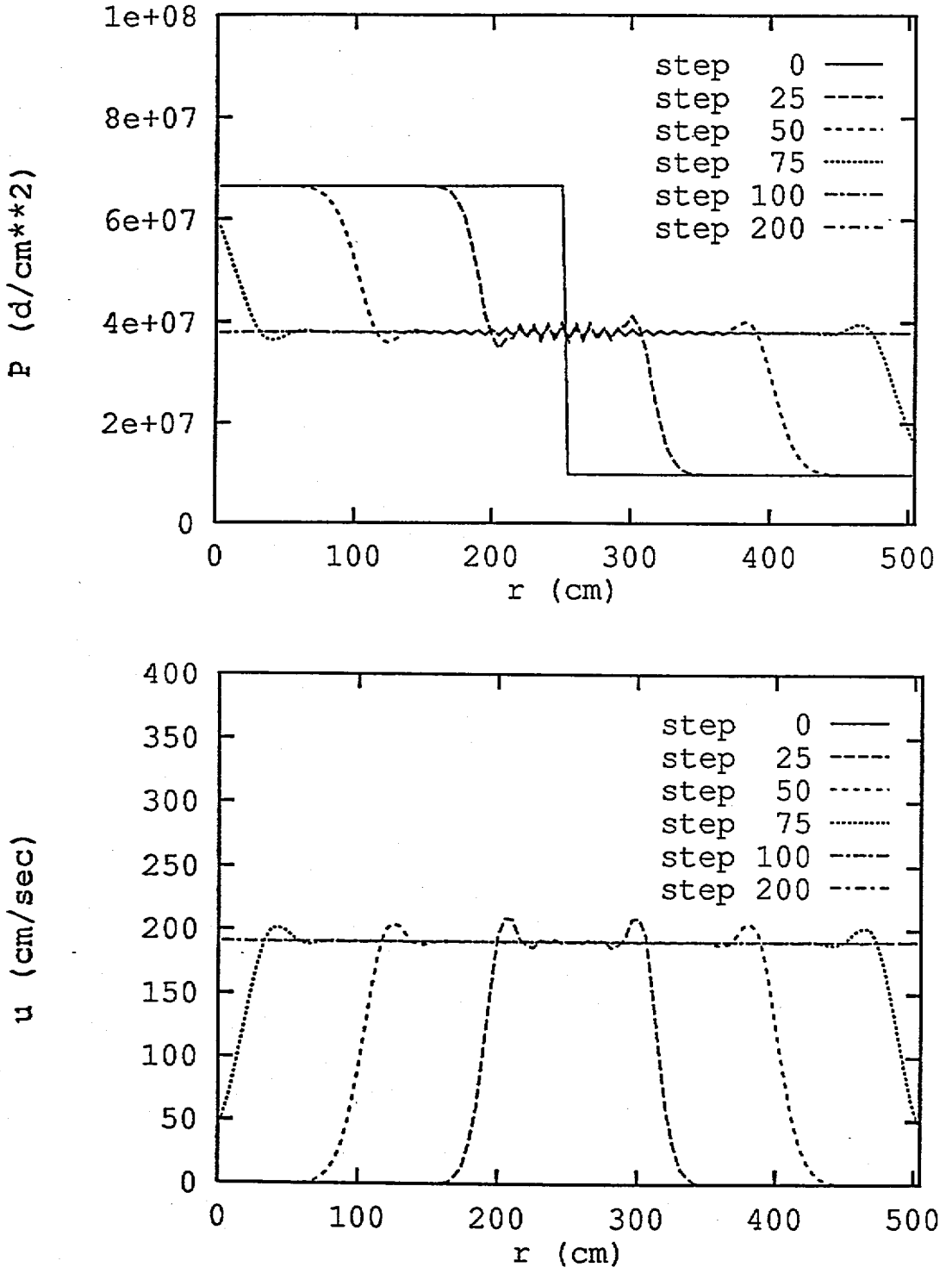

FIGURE 2. 1–D RIEMANN PROBLEM WITH INITIAL WATER STATES OF $p_l = 6.63(10^7)$d/cm^2, $\rho_l = 1.0030$ gm/cc, , $u_l = 0$, $p_r = 9.71(10^6)$d/cm^2, $\rho_r = 1.0004$ gm/cc, $u_r = 0$, COMPUTED WITH $k_t = 0$, $k_u = 0$, $k_c = 0$

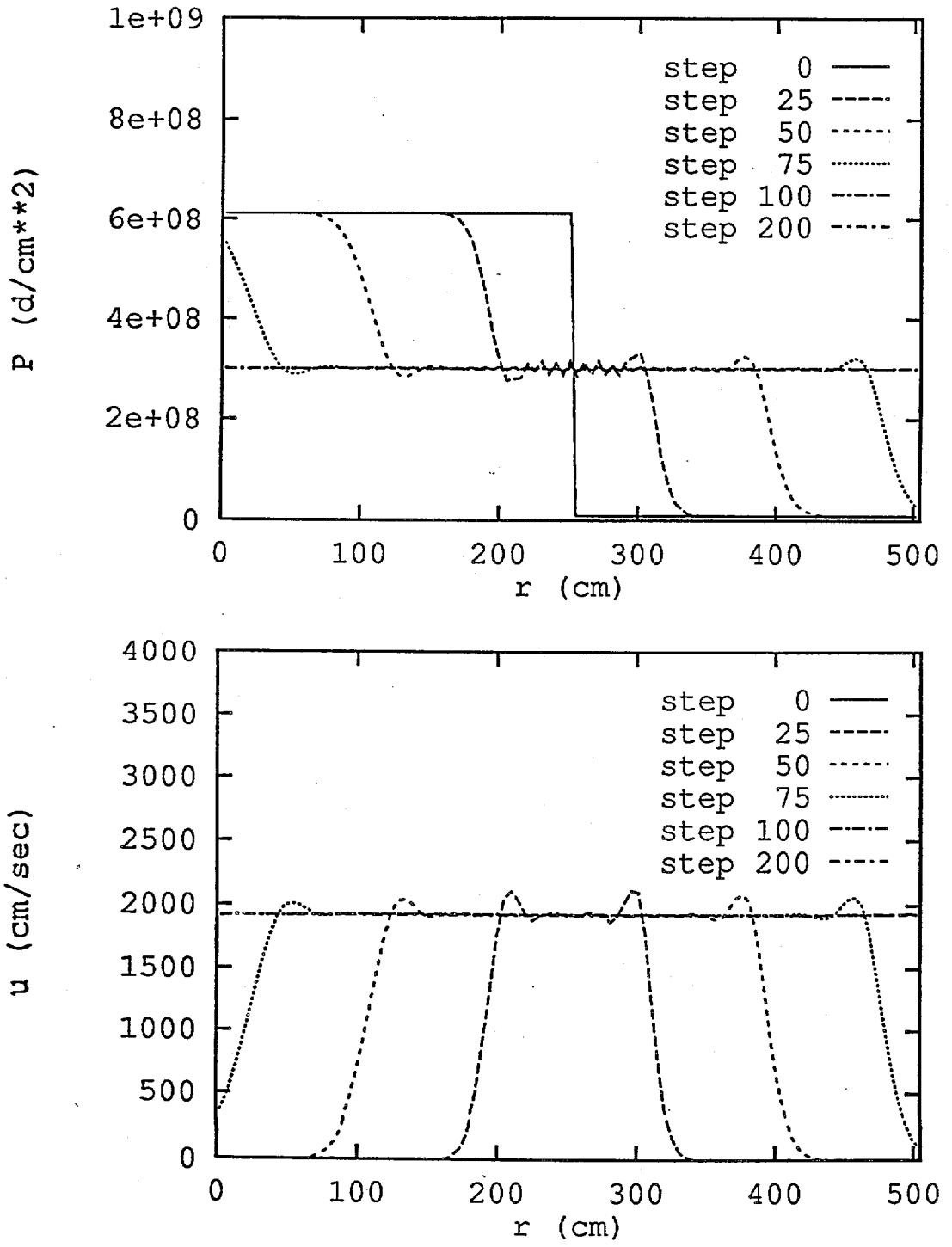

FIGURE 3. 1–D RIEMANN PROBLEM WITH INITIAL WATER STATES OF $p_l = 6.11(10^8)$d/cm^2, $\rho_l = 1.0280$ gm/cc, , $u_l = 0$, $p_r = 9.71(10^6)$d/cm^2, $\rho_r = 1.0004$ gm/cc, $u_r = 0$, COMPUTED WITH $k_t = 0$, $k_u = 0$, $k_c = 0$

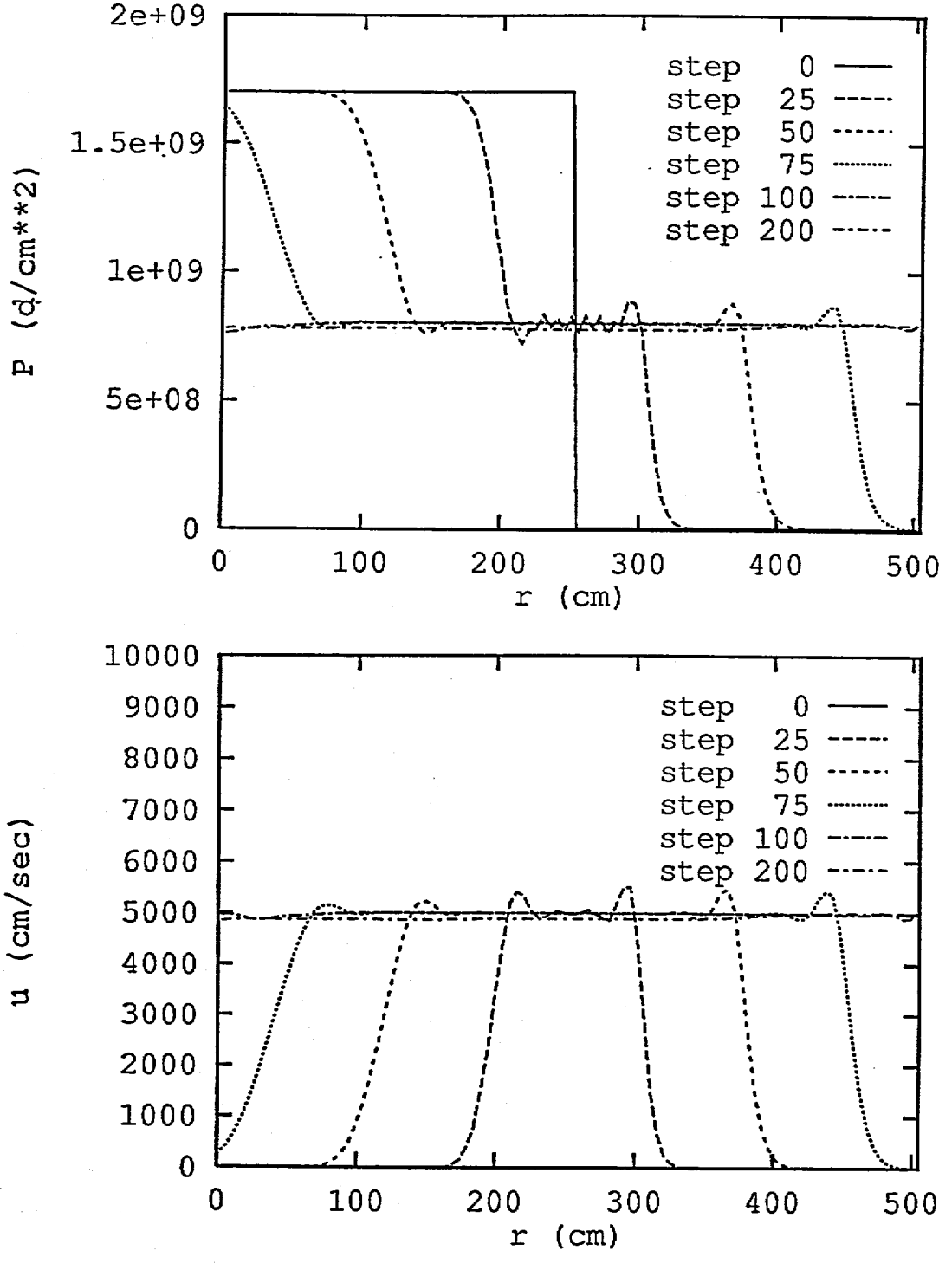

FIGURE 4. 1–D RIEMANN PROBLEM WITH INITIAL WATER STATES OF
$p_l = 1.70(10^9)$d/cm^2, $\rho_l = 1.0780$ gm/cc, , $u_l = 0$,
$p_r = 9.71(10^6)$d/cm^2, $\rho_r = 1.0004$ gm/cc, $u_r = 0$,
COMPUTED WITH $k_t = 0$, $k_u = 0$, $k_c = 0$

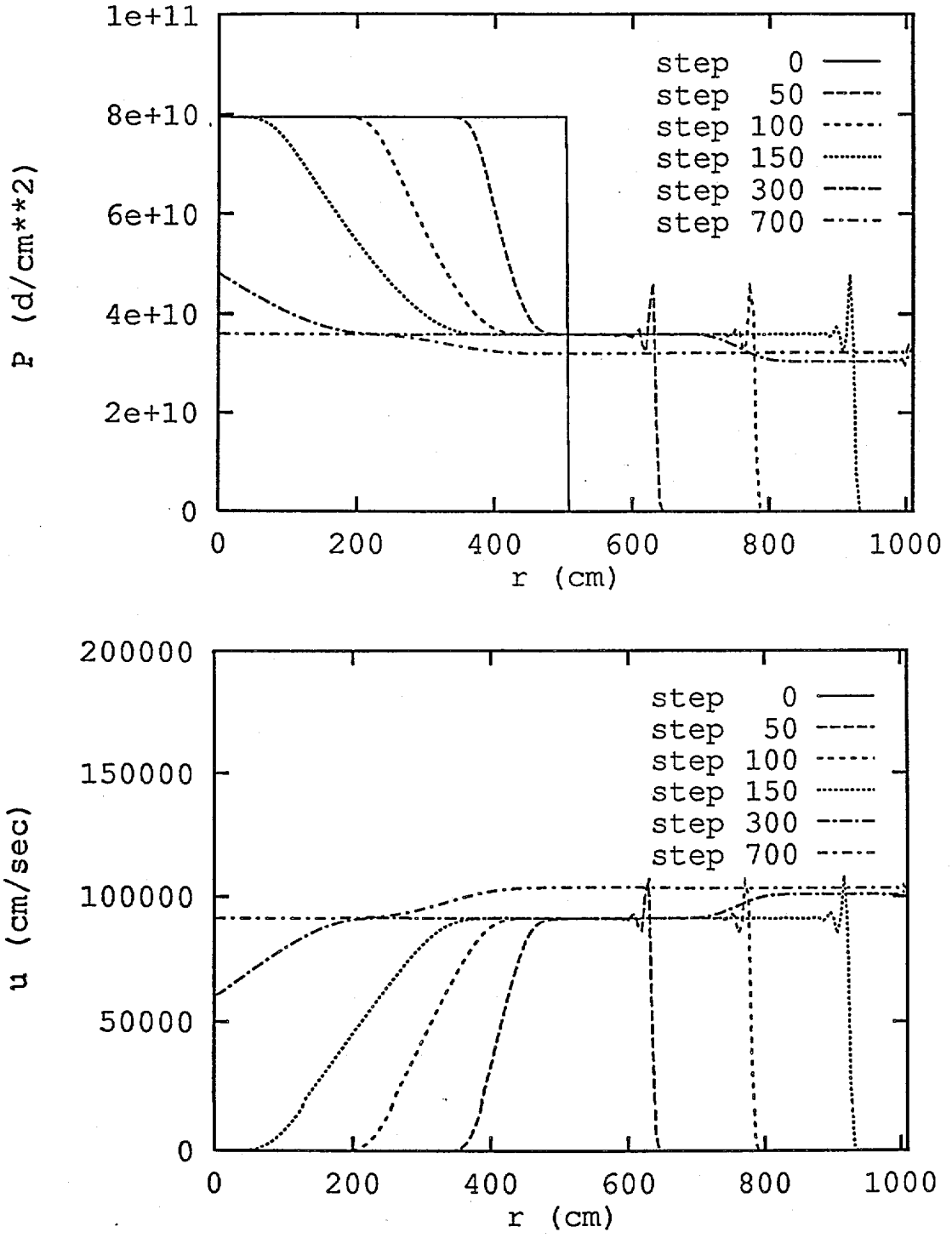

FIGURE 5. 1–D RIEMANN PROBLEM WITH INITIAL STATES OF TNT: $p_l = 7.95(10^{10})$d/cm^2, $\rho_l = 1.63$ gm/cc, $u_l = 0$; WATER $p_r = 1.1(10^7)$d/cm^2, $\rho_r = 1.000458$ gm/cc, $u_r = 0$, COMPUTED WITH $k_t = 0$, $k_u = 0$, $k_c = 0$

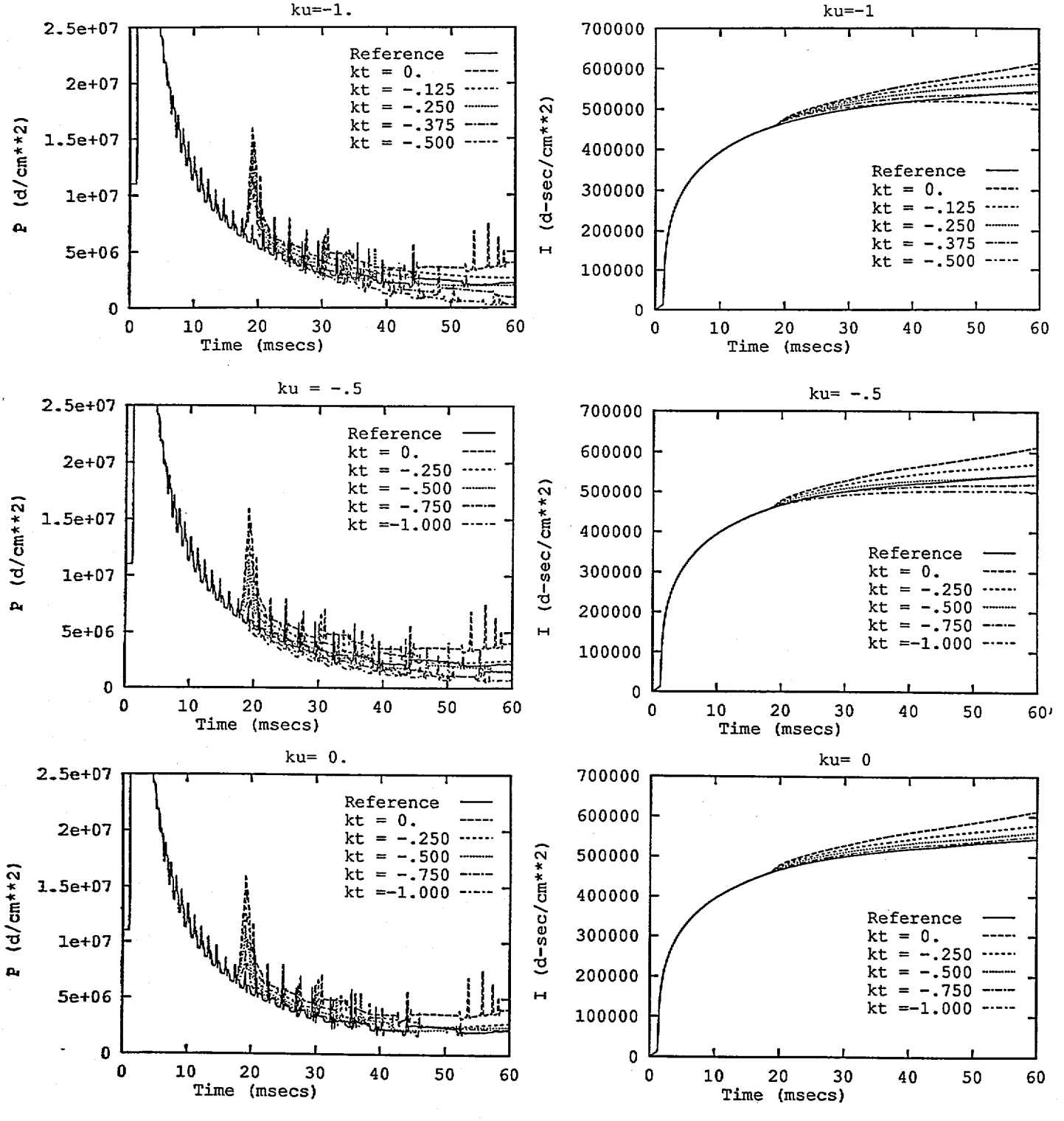

FIGURE 6. INFLUENCE OF k_t AND k_u ON THE 1–D SPHERICAL PRESSURE AND IMPULSE AT CELL 50 ON A 300 CELL UNIFORM MESH AT A DEPTH OF 103.6m

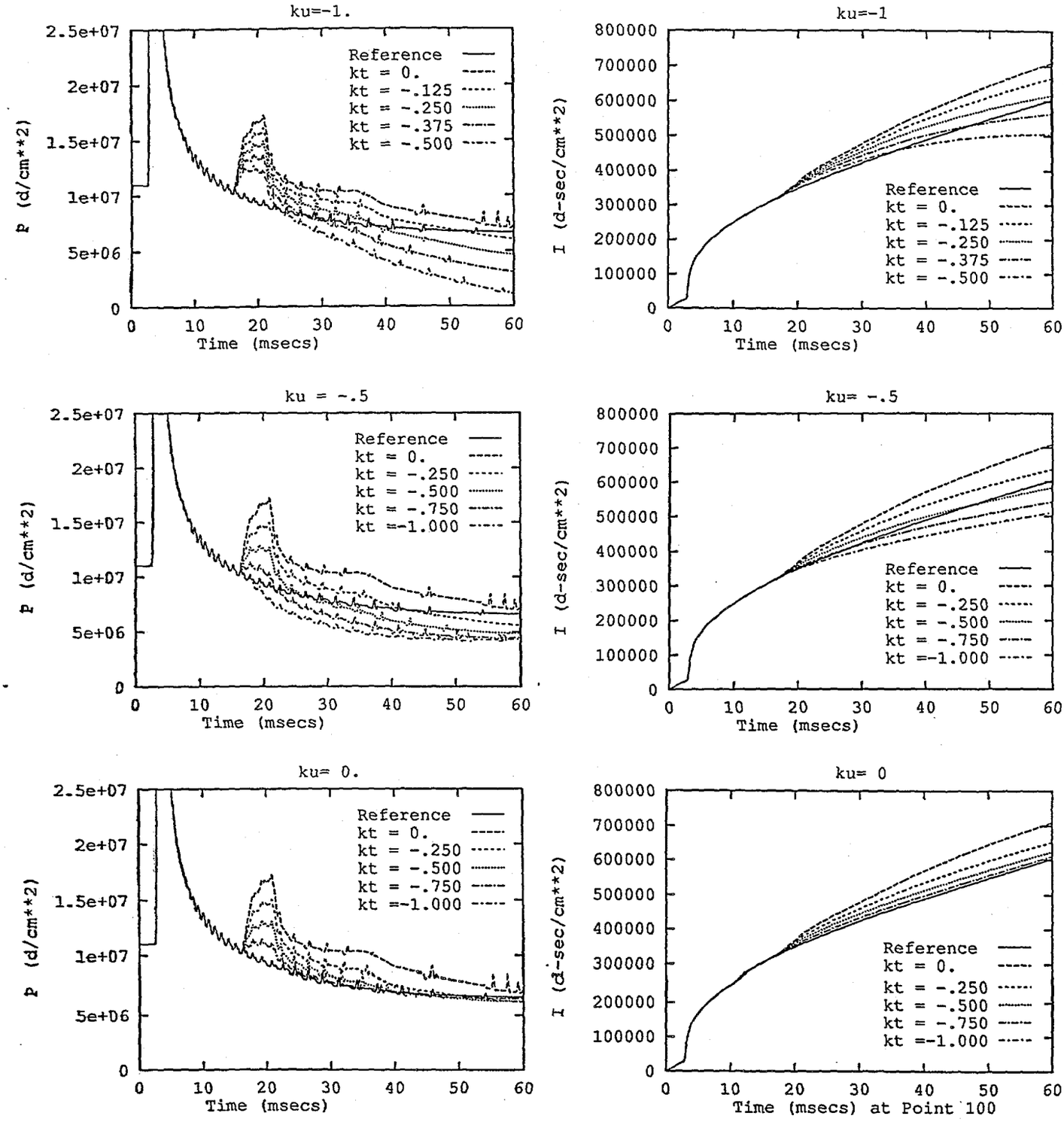

FIGURE 7. INFLUENCE OF k_t AND k_u ON THE 1-D SPHERICAL PRESSURE AND IMPULSE AT CELL 100 ON A 300 CELL UNIFORM MESH AT A DEPTH OF 103.6m

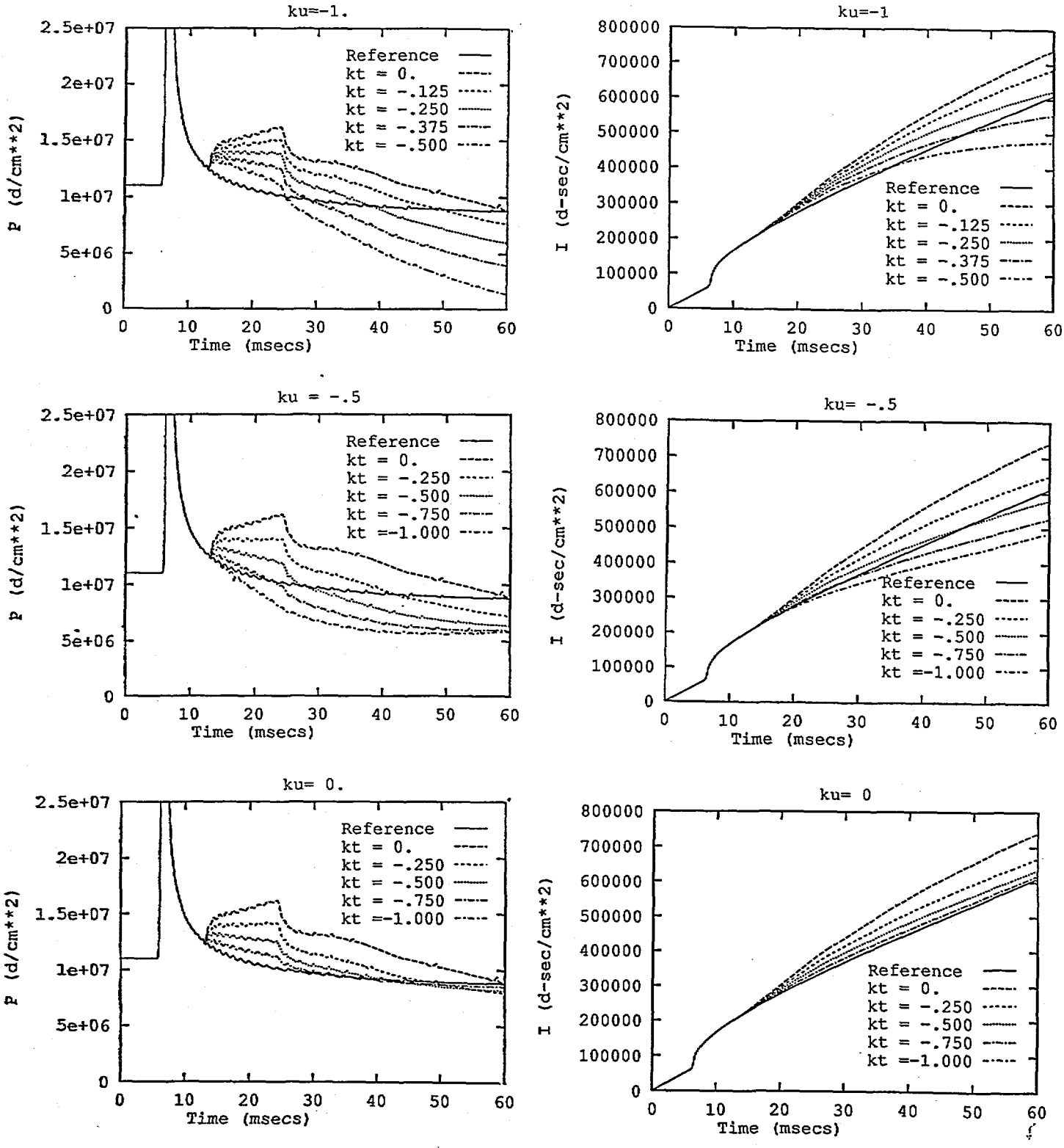

FIGURE 8. INFLUENCE OF k_t AND k_u ON THE 1-D SPHERICAL PRESSURE AND IMPULSE AT CELL 200 ON A 300 CELL UNIFORM MESH AT A DEPTH OF 103.6m

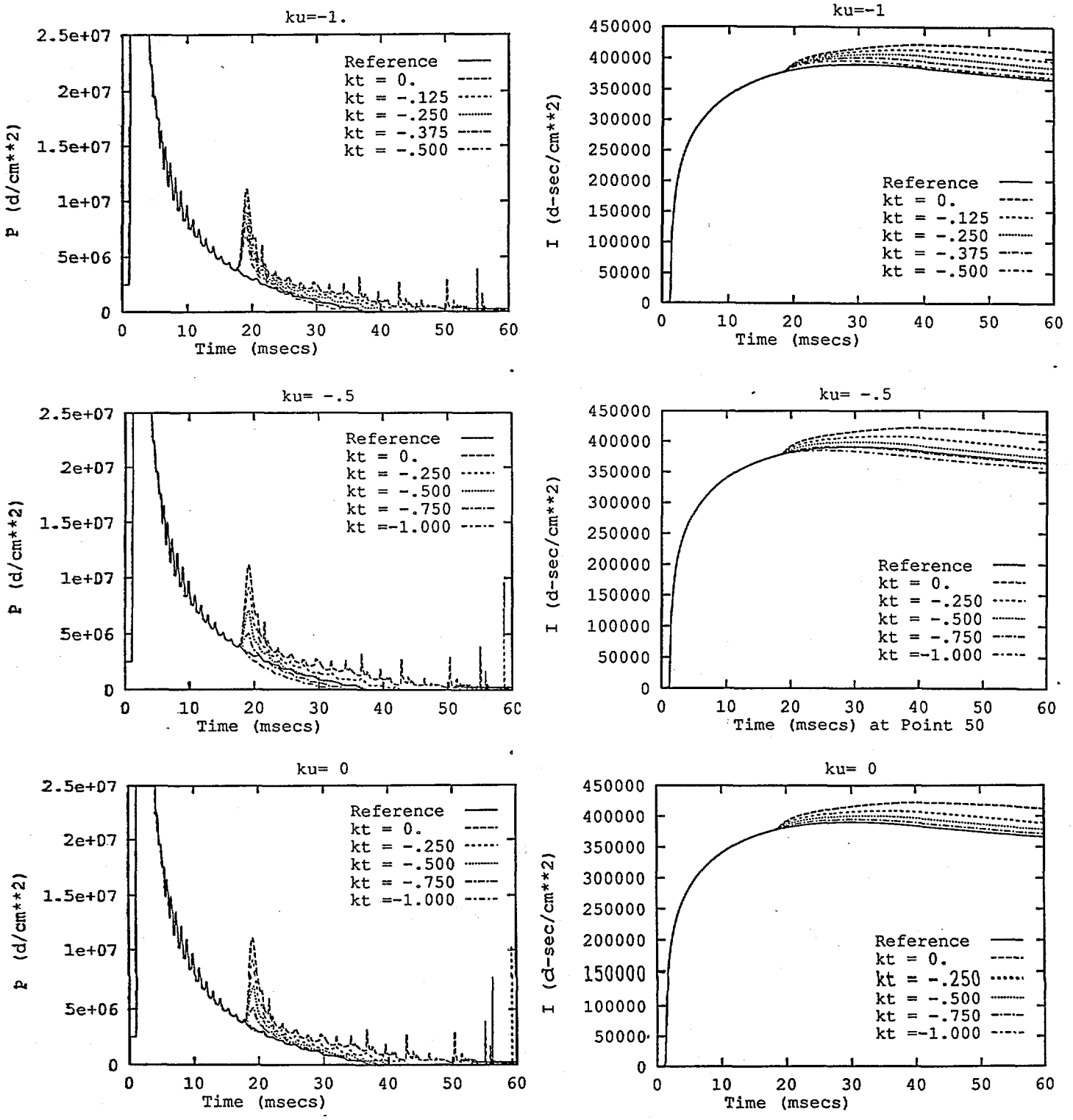

FIGURE 9. INFLUENCE OF k_t AND k_u ON THE 1–D SPHERICAL PRESSURE AND IMPULSE AT CELL 50 ON A 300 CELL UNIFORM MESH AT A DEPTH OF 15.24m

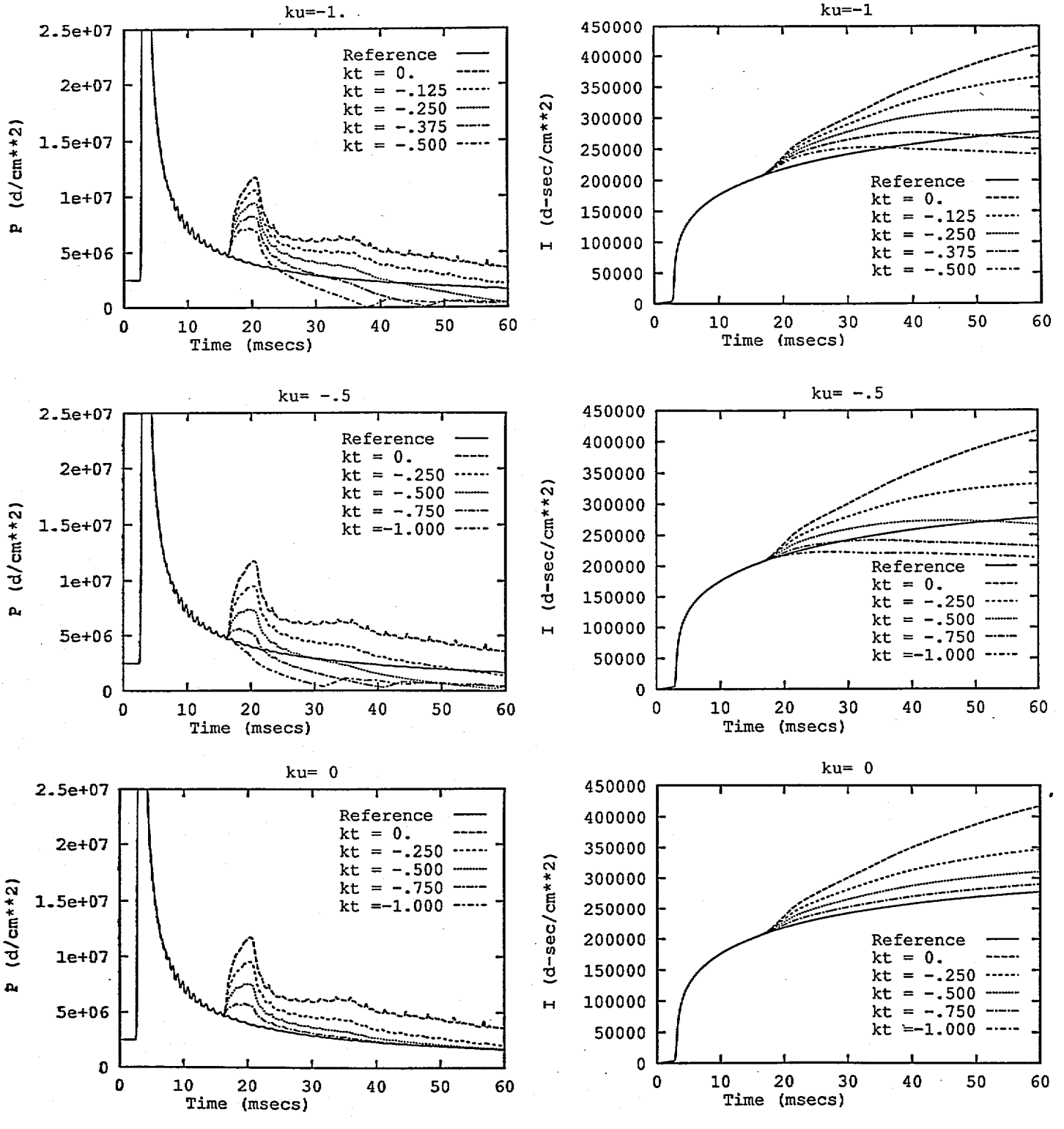

FIGURE 10. INFLUENCE OF k_t AND k_u ON THE 1–D SPHERICAL PRESSURE AND IMPULSE AT CELL 100 ON A 300 CELL UNIFORM MESH AT A DEPTH OF 15.24m

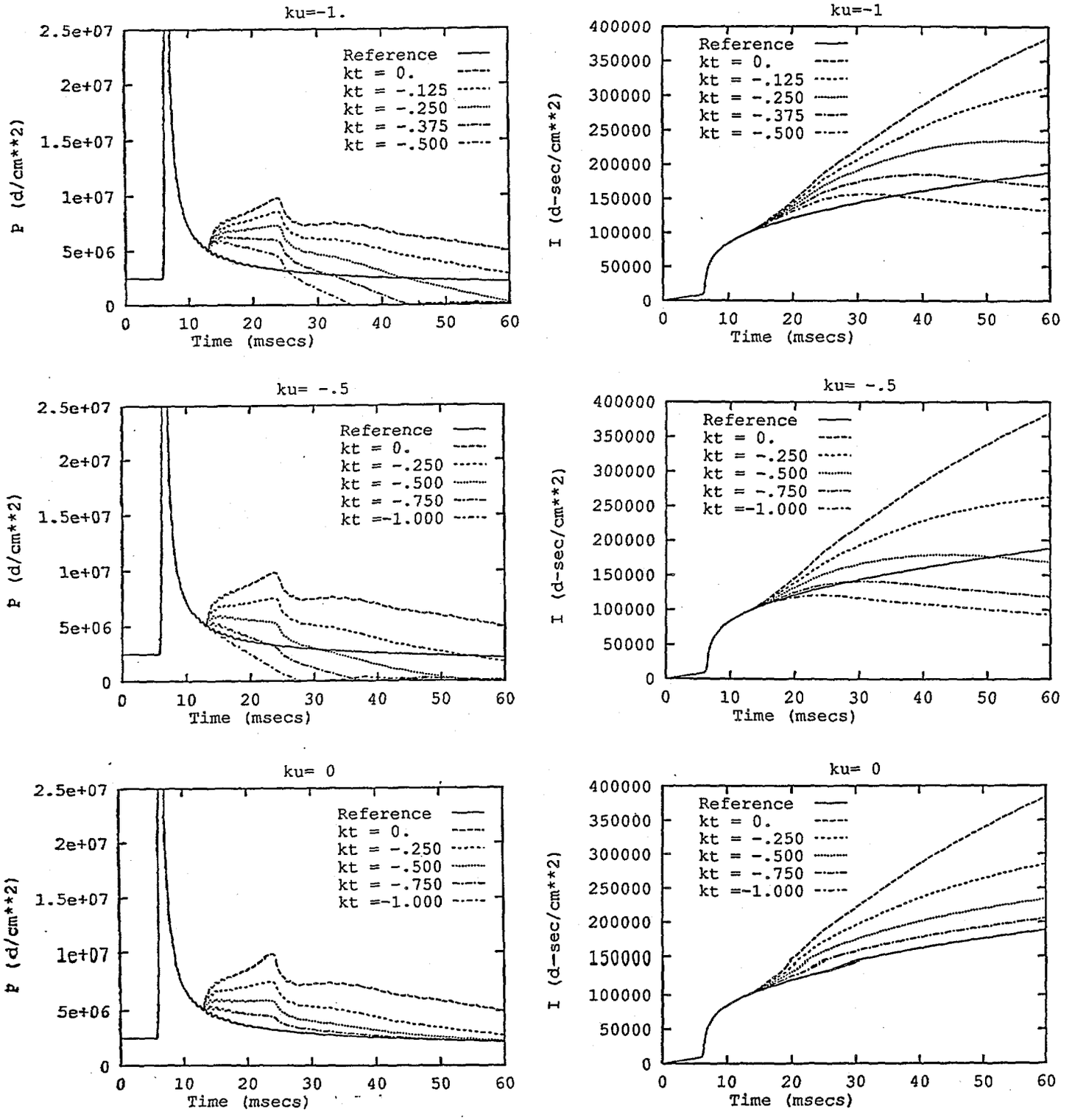

FIGURE 11. INFLUENCE OF k_t AND k_u ON THE 1-D SPHERICAL PRESSURE AND IMPULSE AT CELL 200 ON A 300 CELL UNIFORM MESH AT A DEPTH OF 15.24m

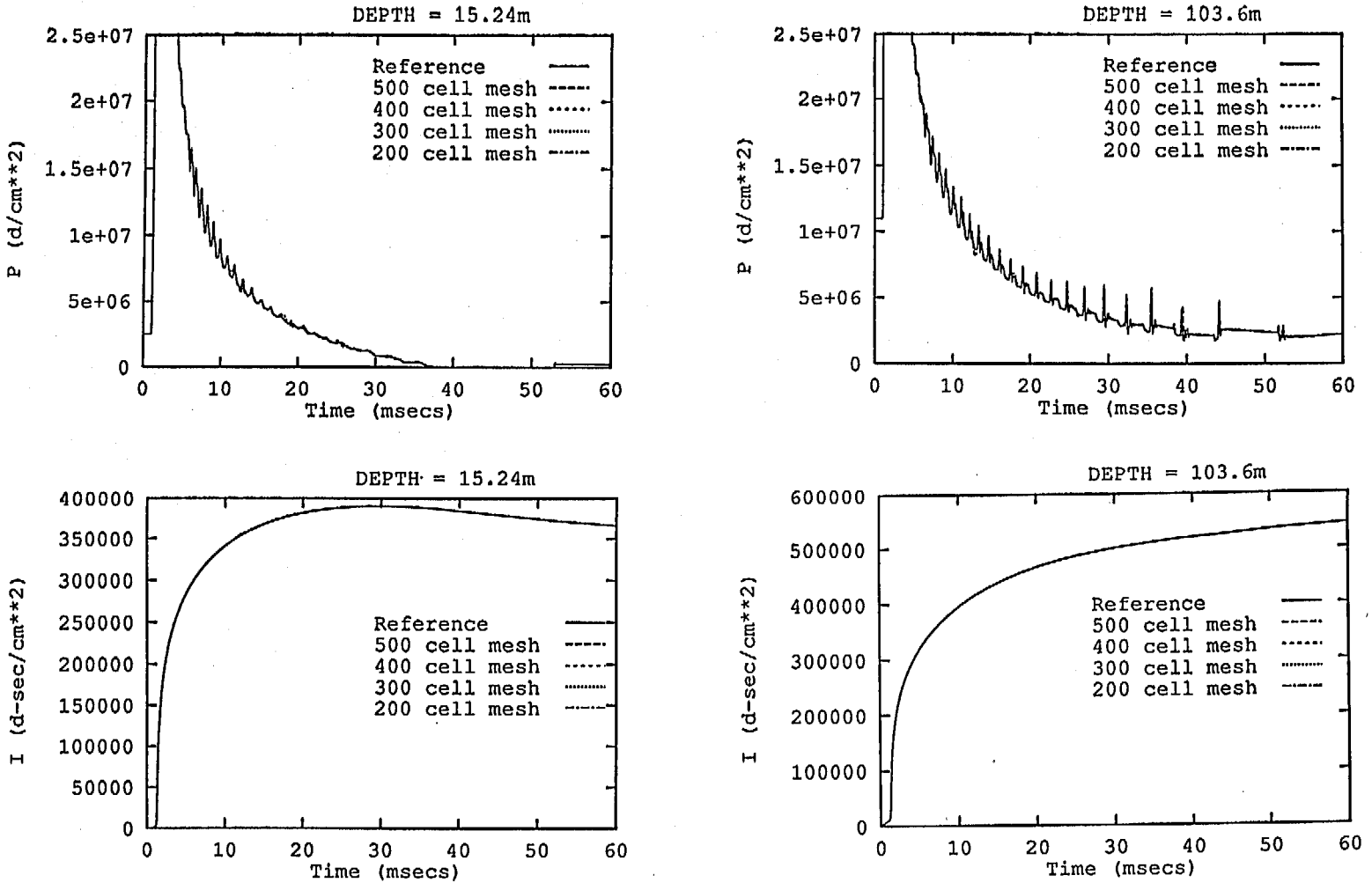

FIGURE 12. COMPARISON OF THE 1–D SPHERICAL REFERENCE AND TRIAL PRESSURE AND IMPULSE HISTORIES AT POINT 50, FOR DIFFERENT TRIAL MESHES AND DEPTHS, COMPUTED WITH $k_t = -1$, $k_u = 0$, $k_c = -2$

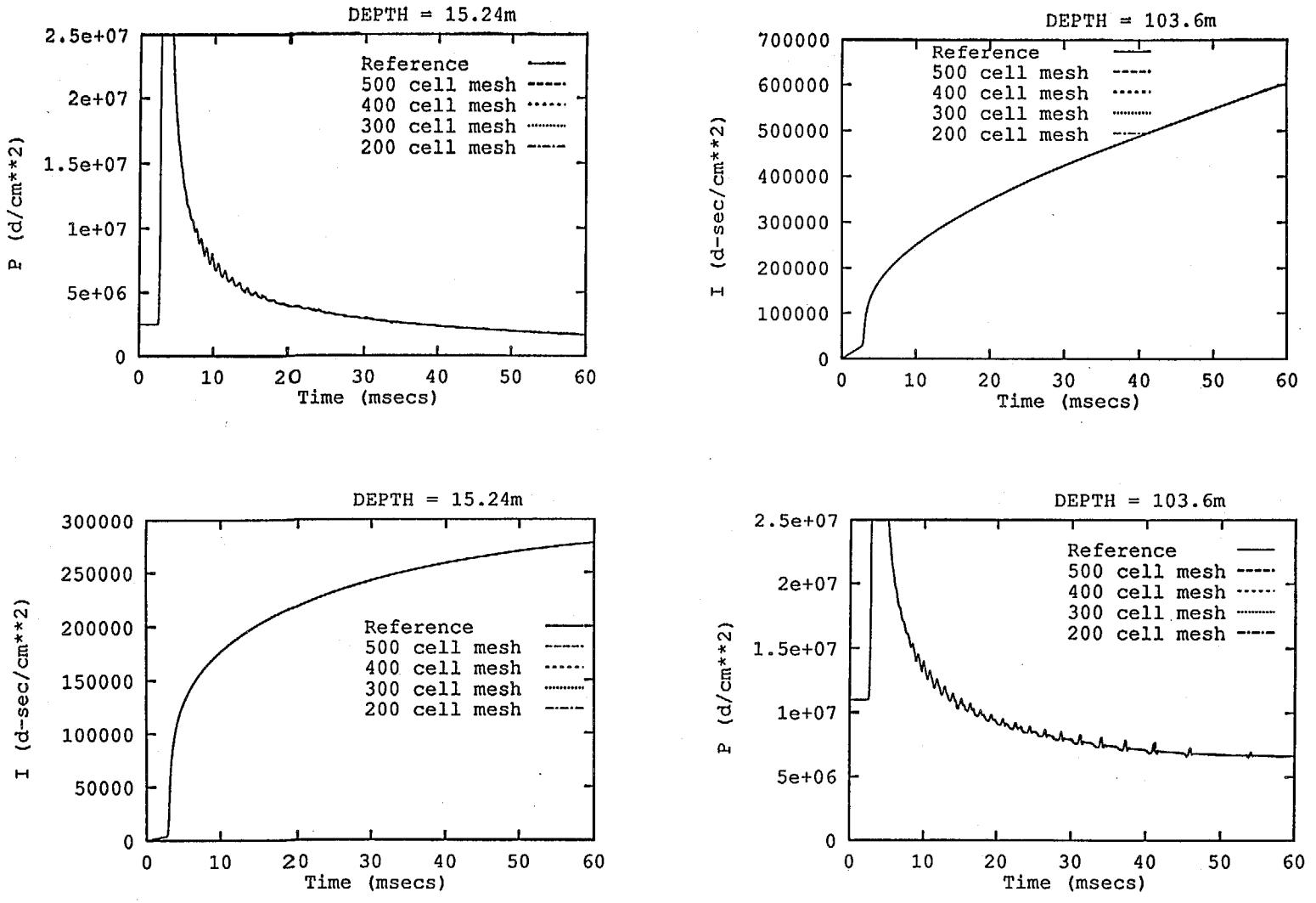

FIGURE 13. COMPARISON OF THE 1–D SPHERICAL REFERENCE AND TRIAL PRESSURE AND IMPULSE HISTORIES AT POINT 100, FOR DIFFERENT TRIAL MESHES AND DEPTHS, COMPUTED WITH $k_t = -1$, $k_u = 0$, $k_c = -2$

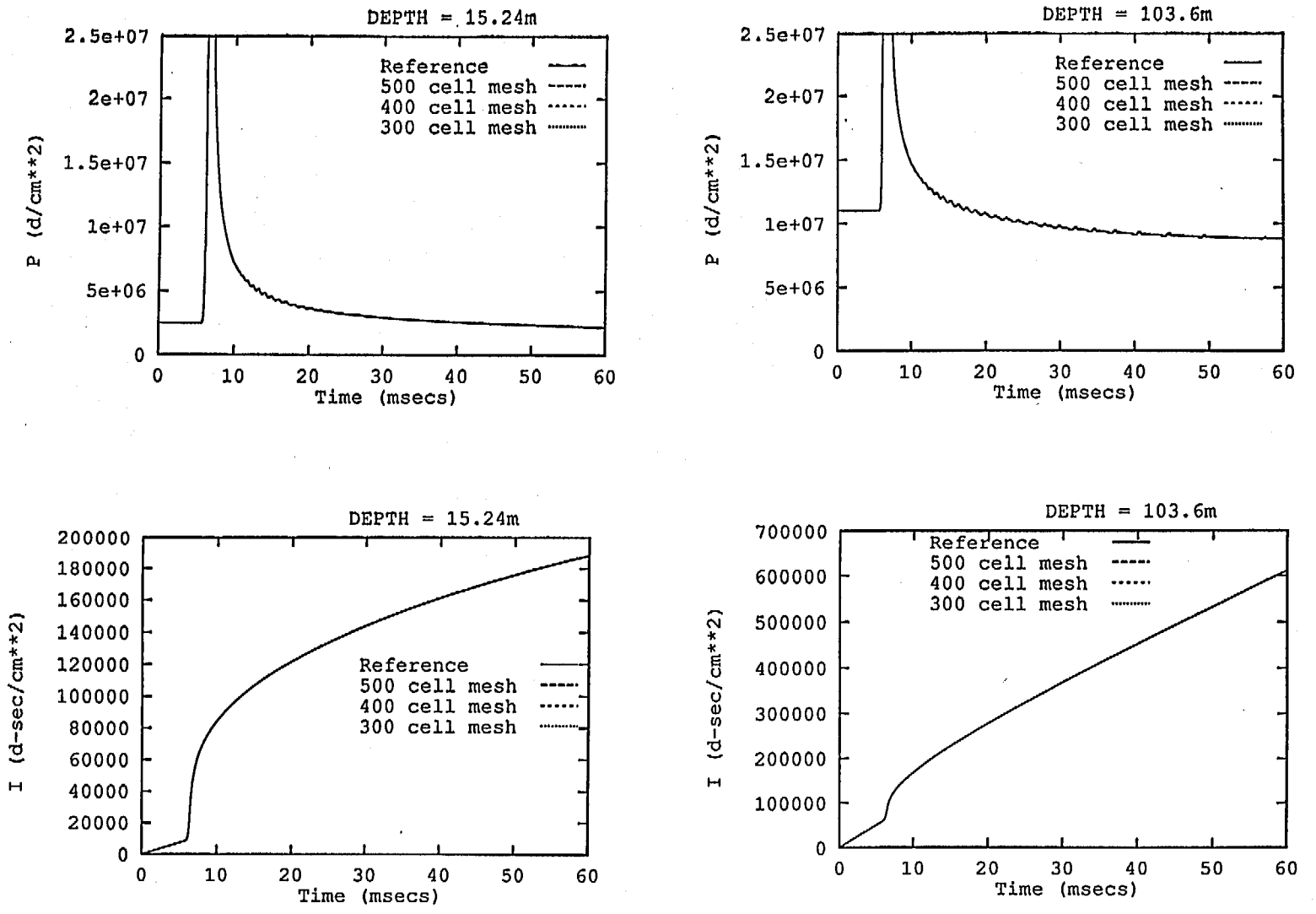

FIGURE 14. COMPARISON OF THE 1–D SPHERICAL REFERENCE AND TRIAL PRESSURE AND IMPULSE HISTORIES AT POINT 200, FOR DIFFERENT TRIAL MESHES AND DEPTHS, COMPUTED WITH $k_t = -1$, $k_u = 0$, $k_c = -2$

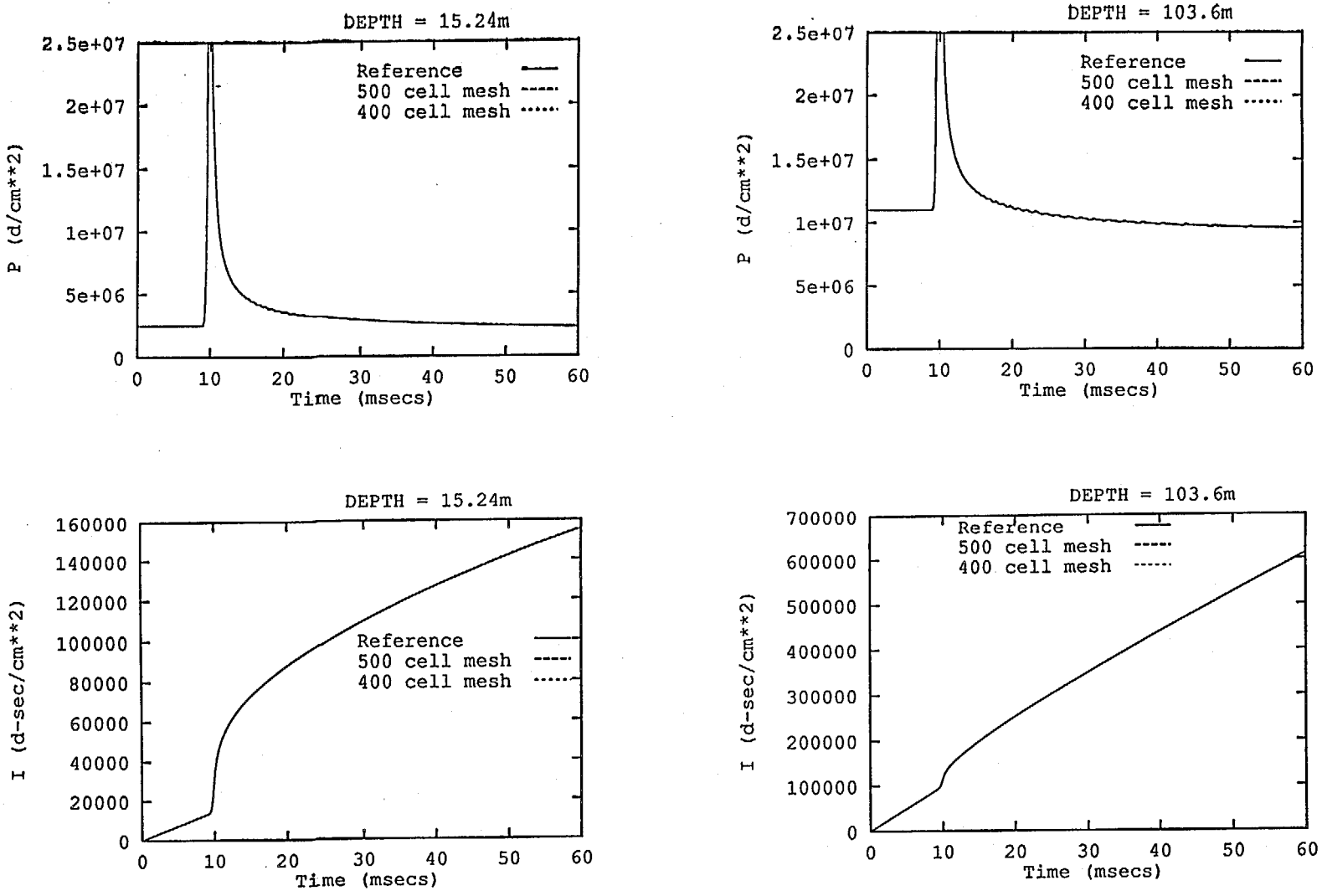

FIGURE 15. COMPARISON OF THE 1–D SPHERICAL REFERENCE AND TRIAL PRESSURE AND IMPULSE HISTORIES AT POINT 300, FOR DIFFERENT TRIAL MESHES AND DEPTHS, COMPUTED WITH $k_t = -1$, $k_u = 0$, $k_c = -2$

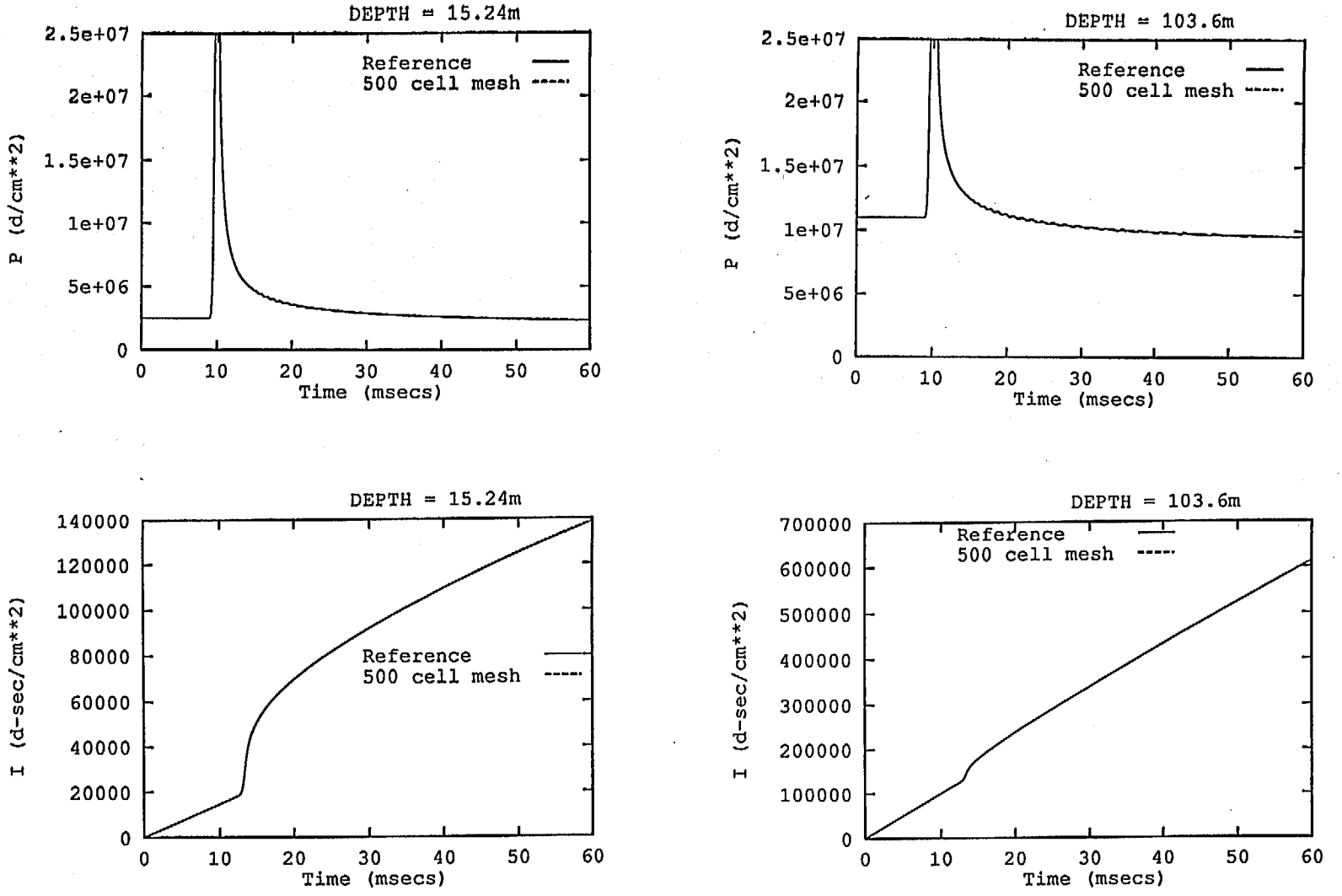

FIGURE 16. COMPARISON OF THE 1–D SPHERICAL REFERENCE AND TRIAL PRESSURE AND IMPULSE HISTORIES AT POINT 400, FOR DIFFERENT DEPTHS, COMPUTED WITH $k_t = -1$, $k_u = 0$, $k_c = -2$

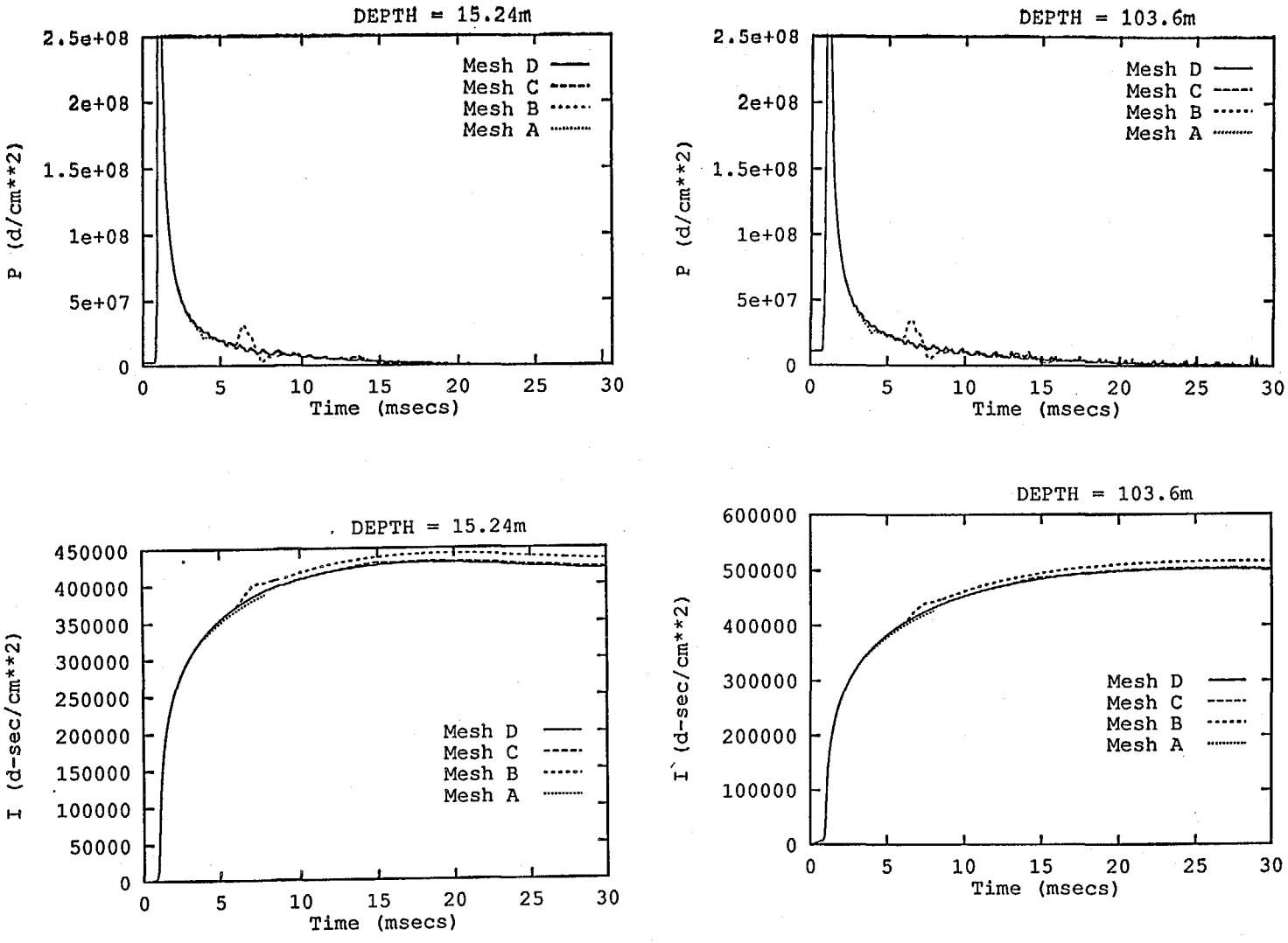

FIGURE 17. COMPARISON OF THE 1–D SPHERICAL REFERENCE AND TRIAL PRESSURE AND IMPULSE HISTORIES AT POINT 40, DEPTHS OF 15.24m AND 103.6m, COMPUTED WITH THE MESH SEQUENCE OF TABLE 1 AND $k_t = -1$, $k_u = 0$, $k_c = -2$

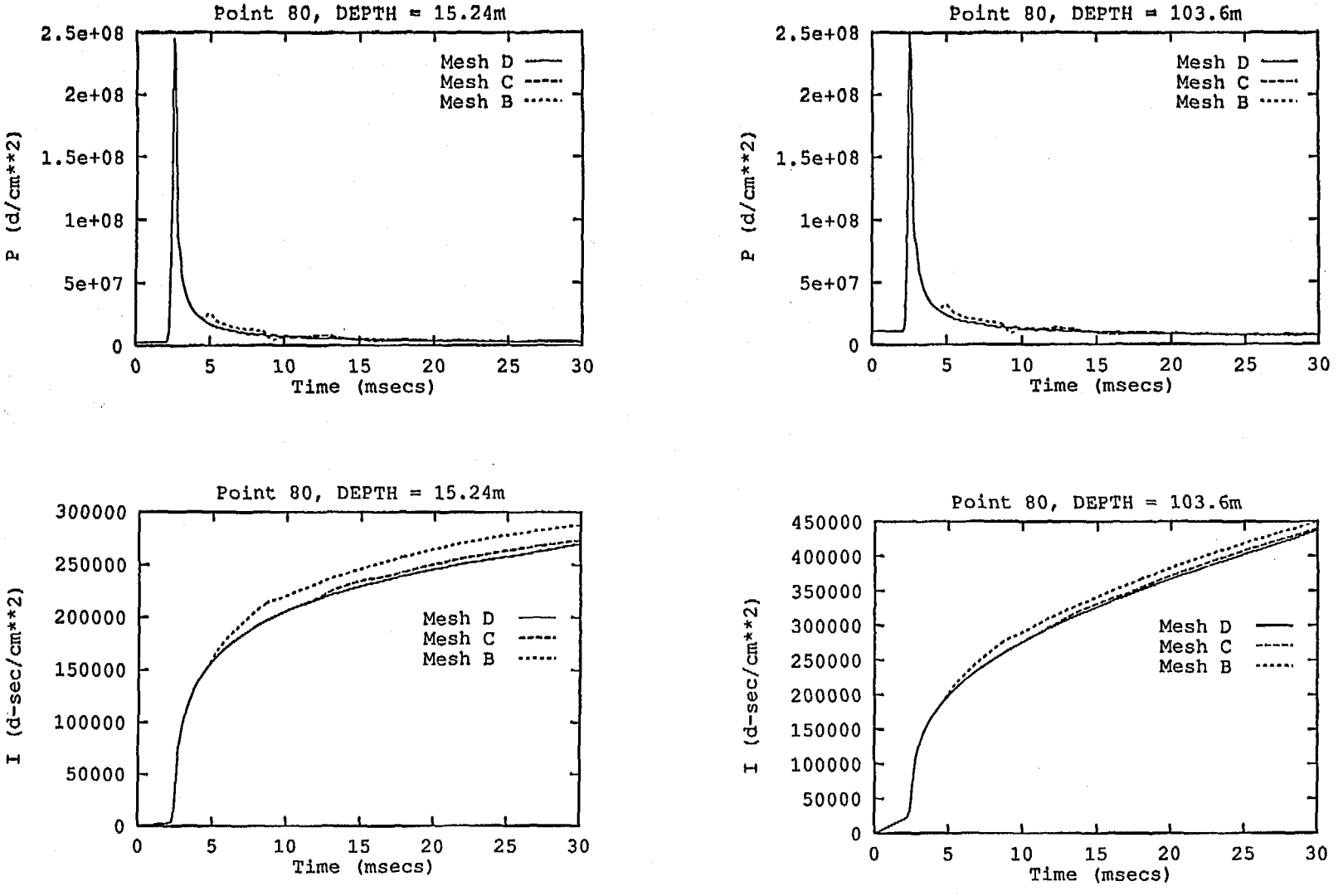

FIGURE 18. COMPARISON OF THE 1–D SPHERICAL REFERENCE AND TRIAL PRESSURE AND IMPULSE HISTORIES AT POINT 80, DEPTHS OF 15.24m AND 103.6m, COMPUTED WITH THE MESH SEQUENCE OF TABLE 1 AND $k_t = -1$, $k_u = 0$, $k_c = -2$

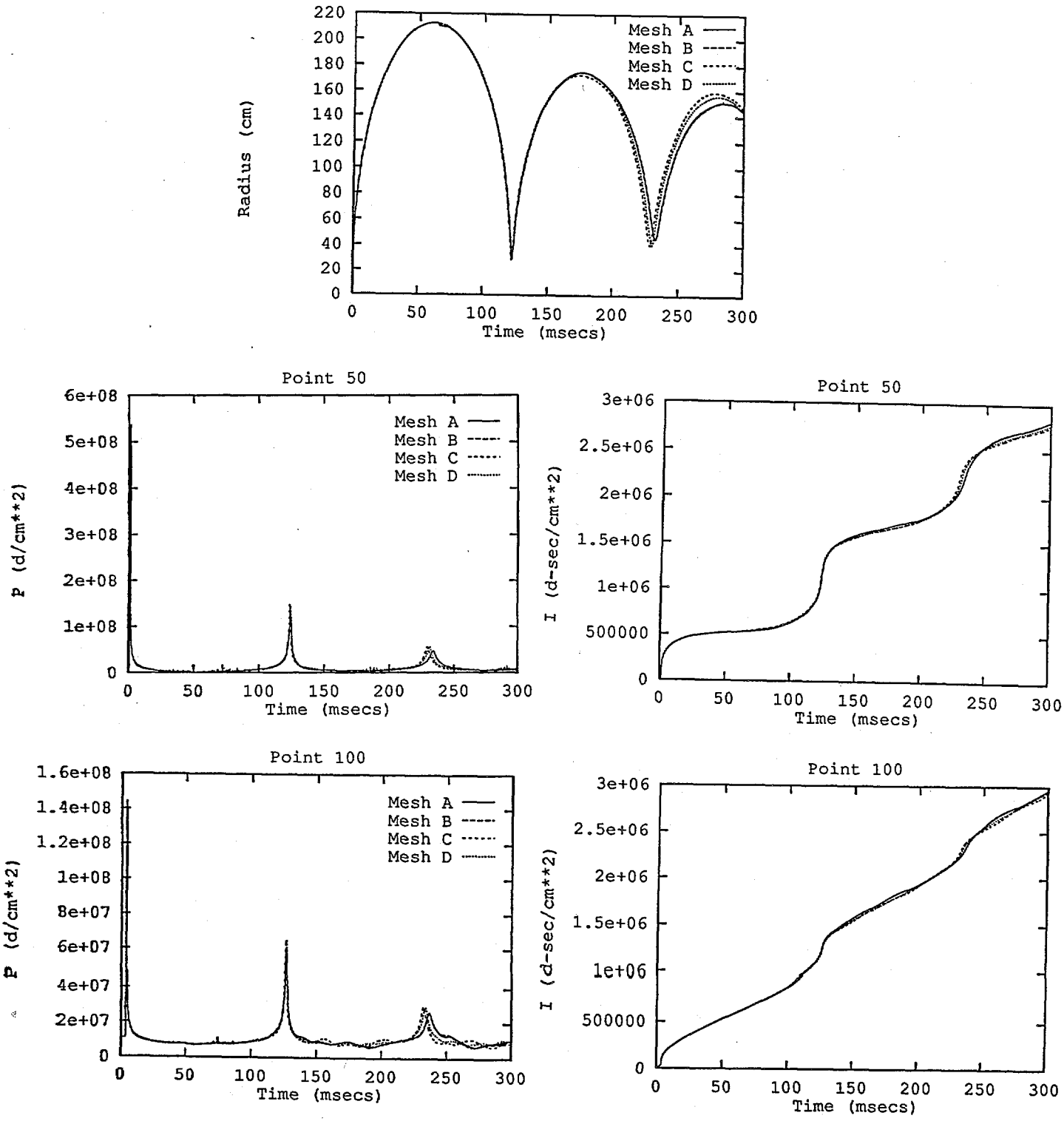

FIGURE 19. COMPARISON OF 1–D SPHERICAL BUBBLE PERIODS USING THE MESH SEQUENCE OF TABLE 2 FOR THE SHORT PERIOD BUBBLE AT A DEPTH OF 103.6m, COMPUTED WITH $k_t = -1$, $k_u = 0$, $k_c = -2$

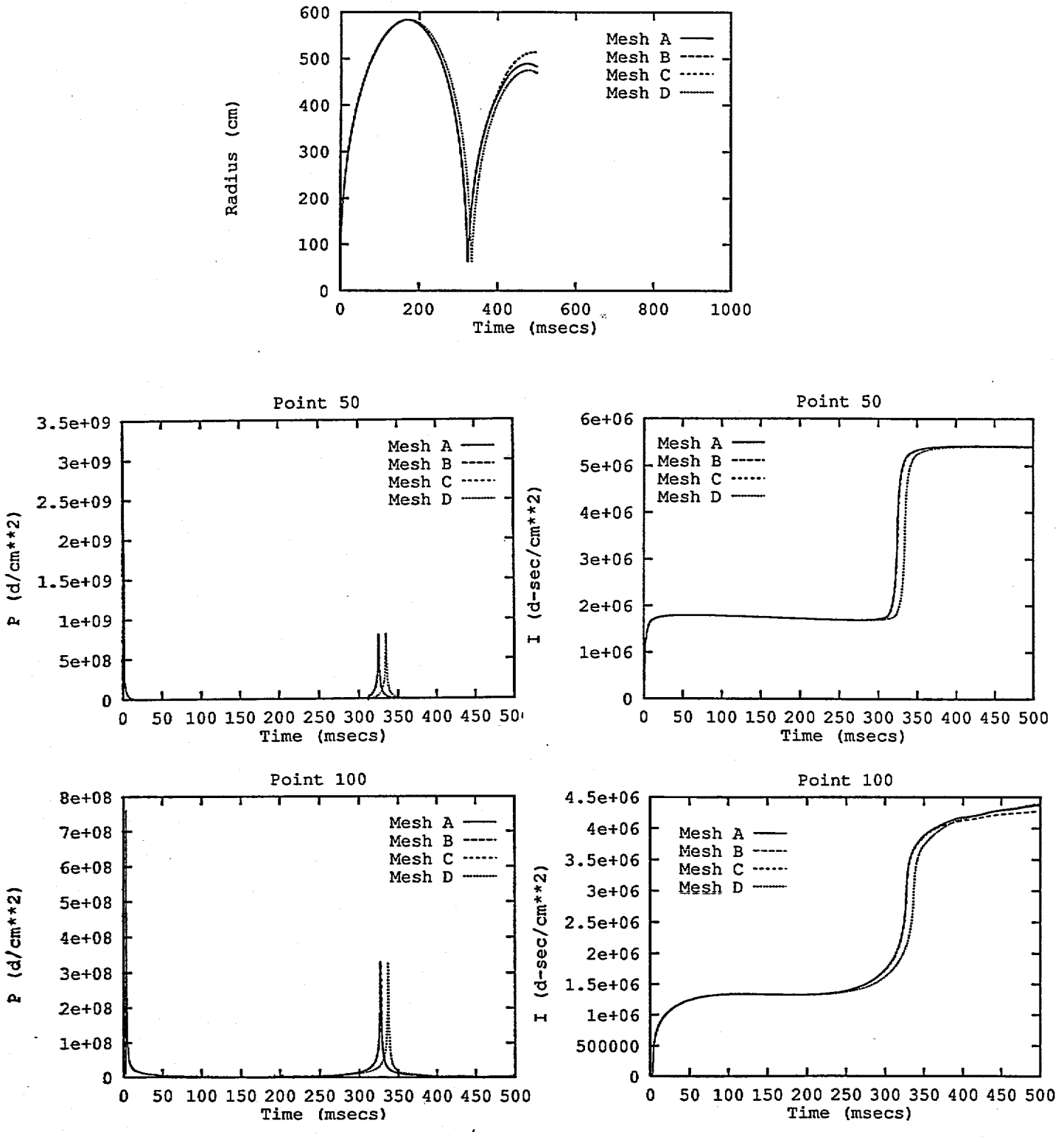

FIGURE 20. COMPARISON OF 1–D SPHERICAL BUBBLE PERIODS USING THE MESH SEQUENCE OF TABLE 3 FOR THE LONG PERIOD BUBBLE AT A DEPTH OF 103.6m, COMPUTED WITH $k_t = -1$, $k_u = 0$, $k_c = -2$

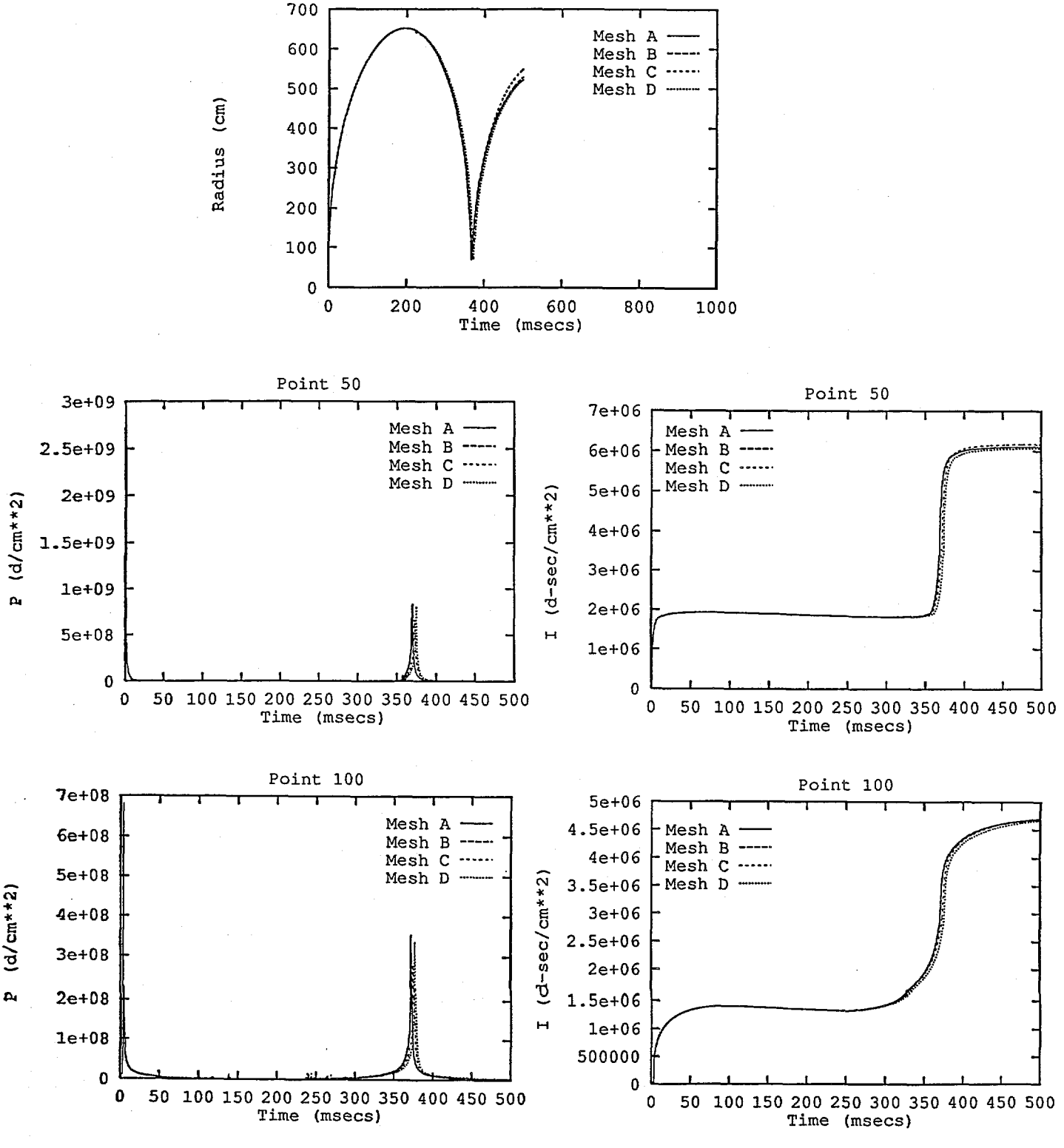

FIGURE 21. COMPARISON OF 1–D SPHERICAL BUBBLE PERIODS USING THE MESH SEQUENCE OF TABLE 4 FOR THE LONG PERIOD BUBBLE AT A DEPTH OF 103.6m, COMPUTED WITH $k_t = -1$, $k_u = 0$, $k_c = -2$

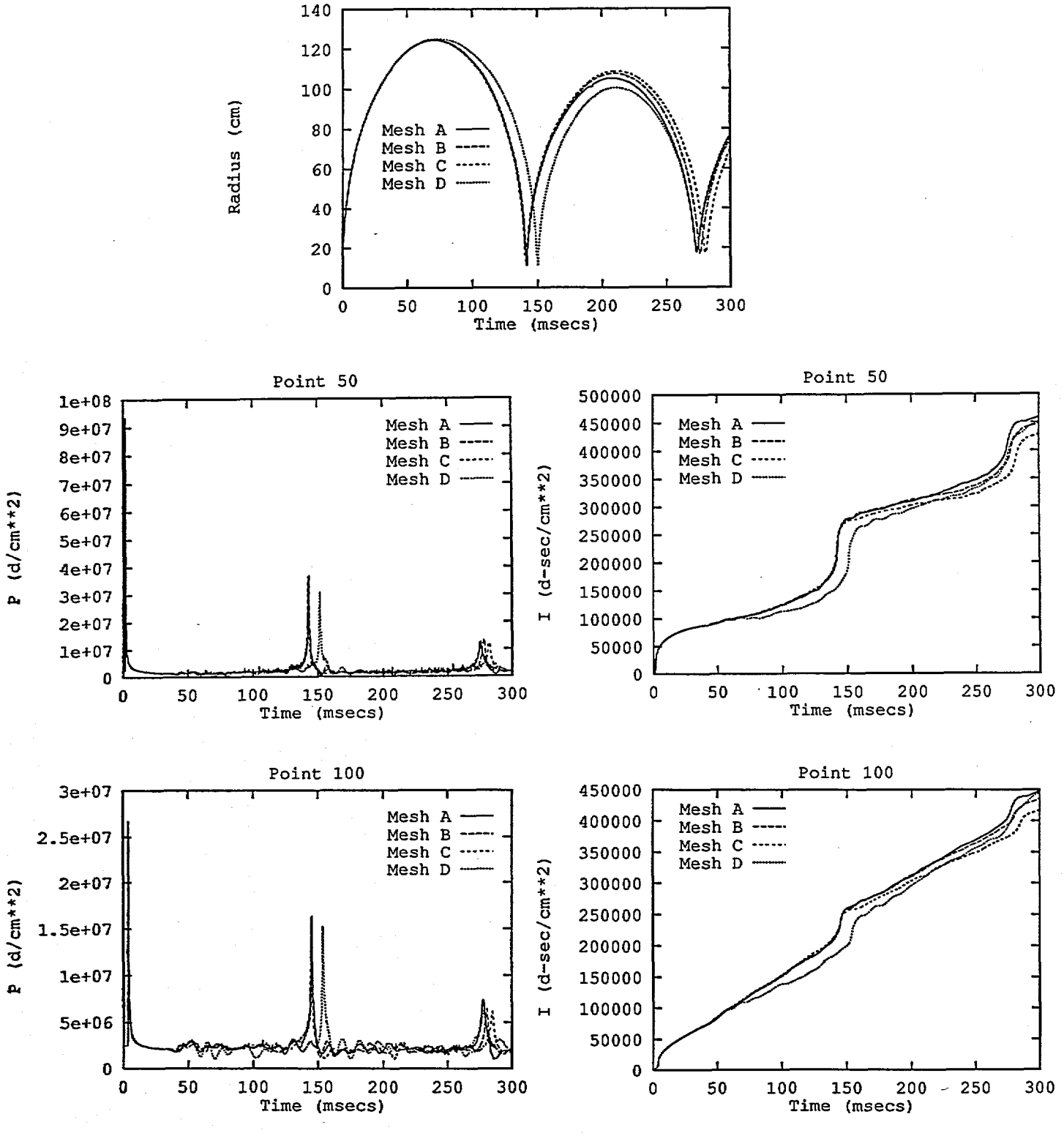

FIGURE 22. COMPARISON OF 1–D SPHERICAL BUBBLE PERIODS USING THE MESH SEQUENCE OF TABLE 2 FOR THE SHORT PERIOD BUBBLE AT A DEPTH OF 15.24m, COMPUTED WITH $k_t = -1$, $k_u = 0$, $k_c = -2$

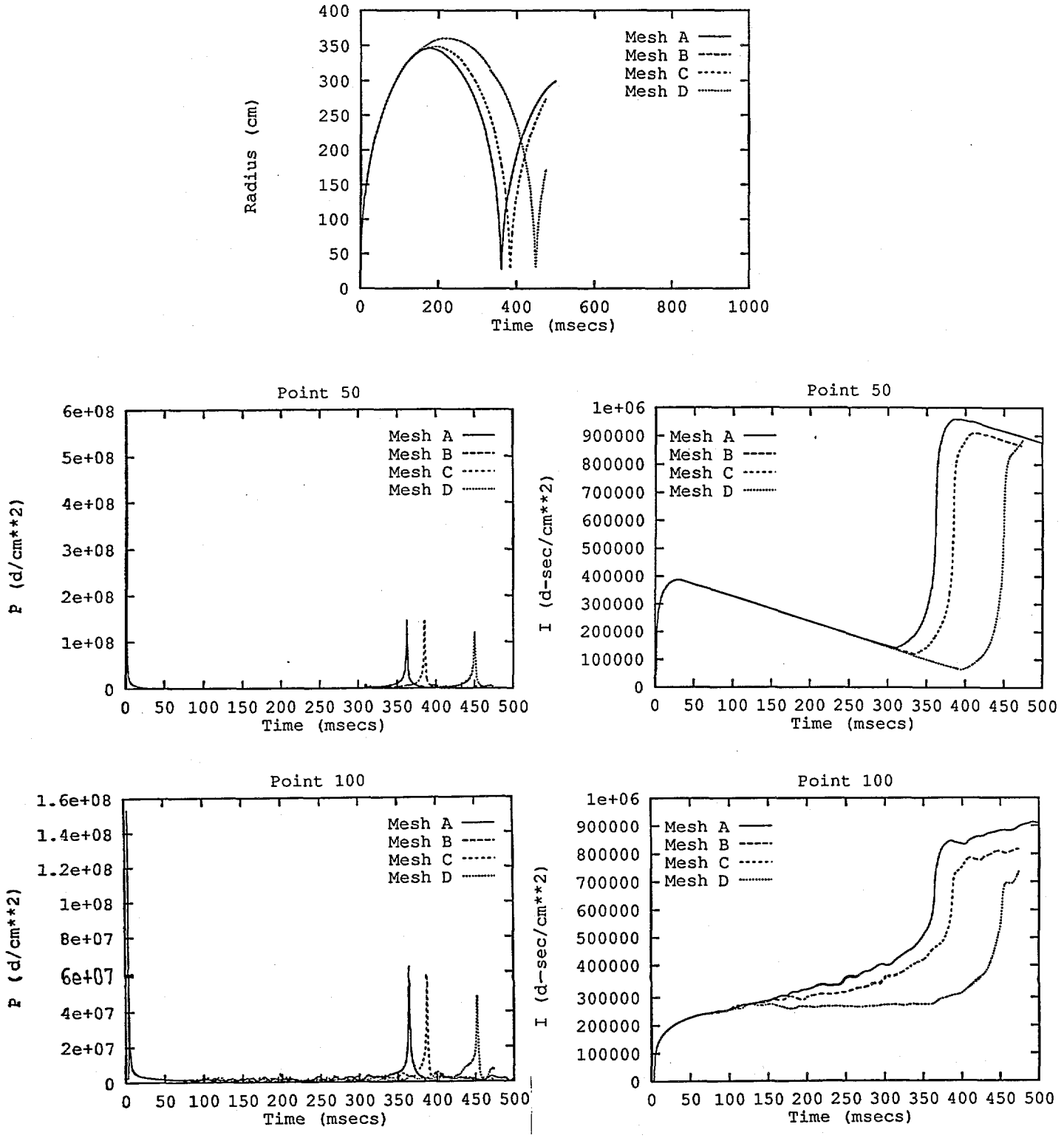

FIGURE 23. COMPARISON OF 1–D SPHERICAL BUBBLE PERIODS USING THE MESH SEQUENCE OF TABLE 3 FOR THE LONG PERIOD BUBBLE AT A DEPTH OF 15.24m, COMPUTED WITH $k_t = -1$, $k_u = 0$, $k_c = -2$

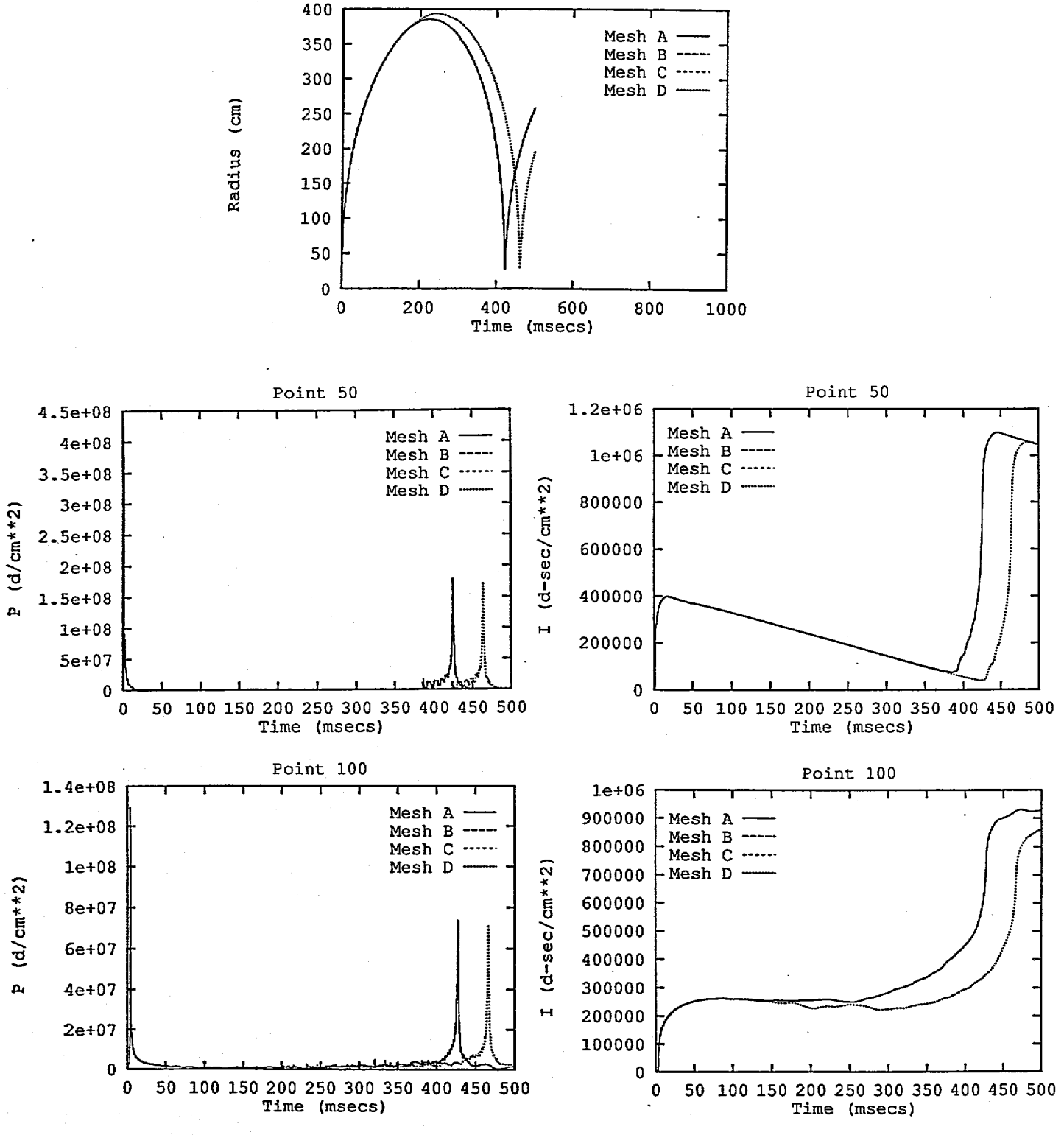

FIGURE 24. COMPARISON OF 1–D SPHERICAL BUBBLE PERIODS USING THE MESH SEQUENCE OF TABLE 5 FOR THE LONG PERIOD BUBBLE AT A DEPTH OF 15.24m, COMPUTED WITH $k_t = -1$, $k_u = 0$, $k_c = -2$

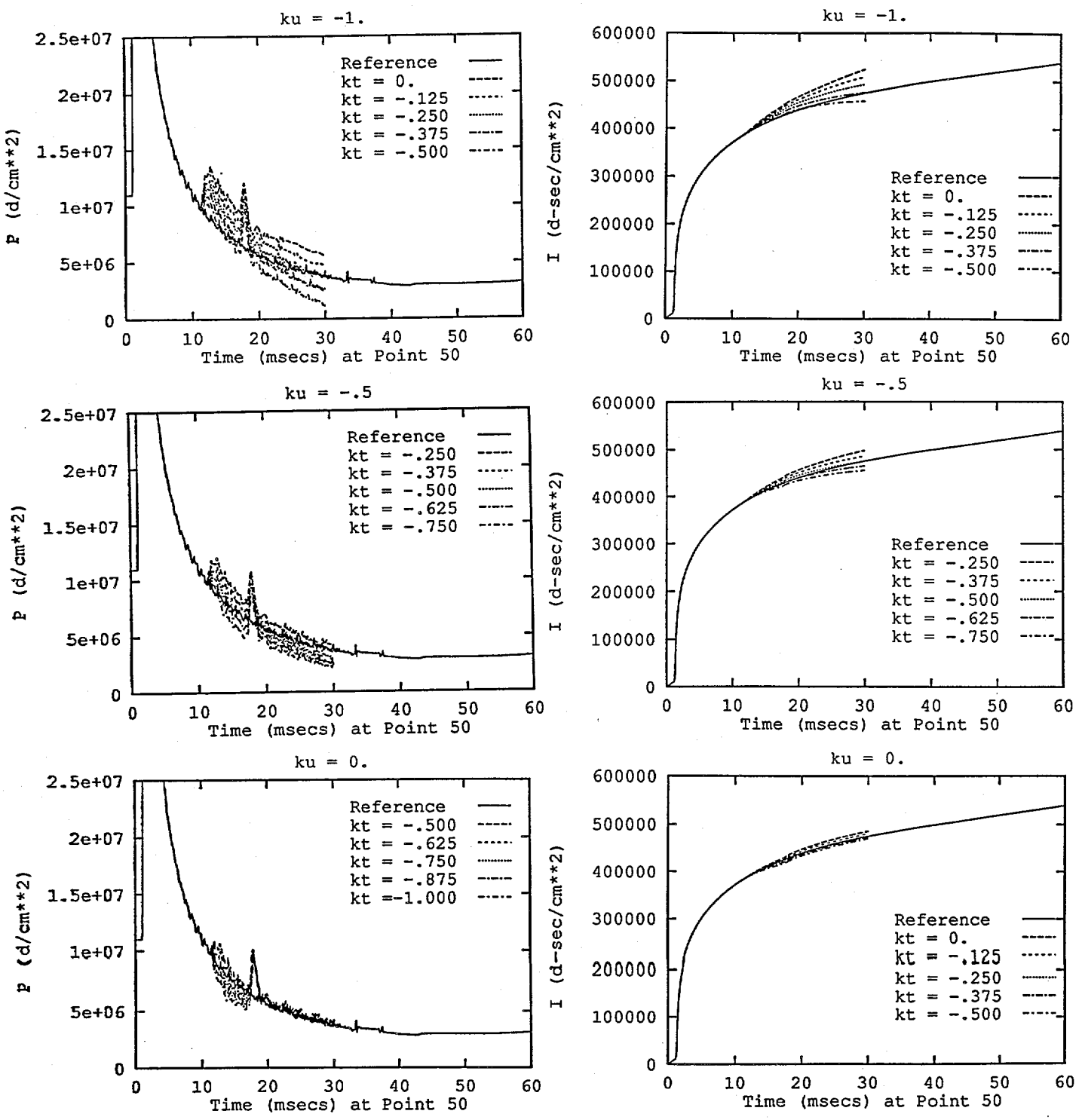

FIGURE 25. INFLUENCE OF k_t AND k_u ON THE 2–D CYLINDRICAL PRESSURE AND IMPULSE AT POINT (50,1) OF A 200X200 CELL UNIFORM MESH AT A DEPTH OF 103.6m

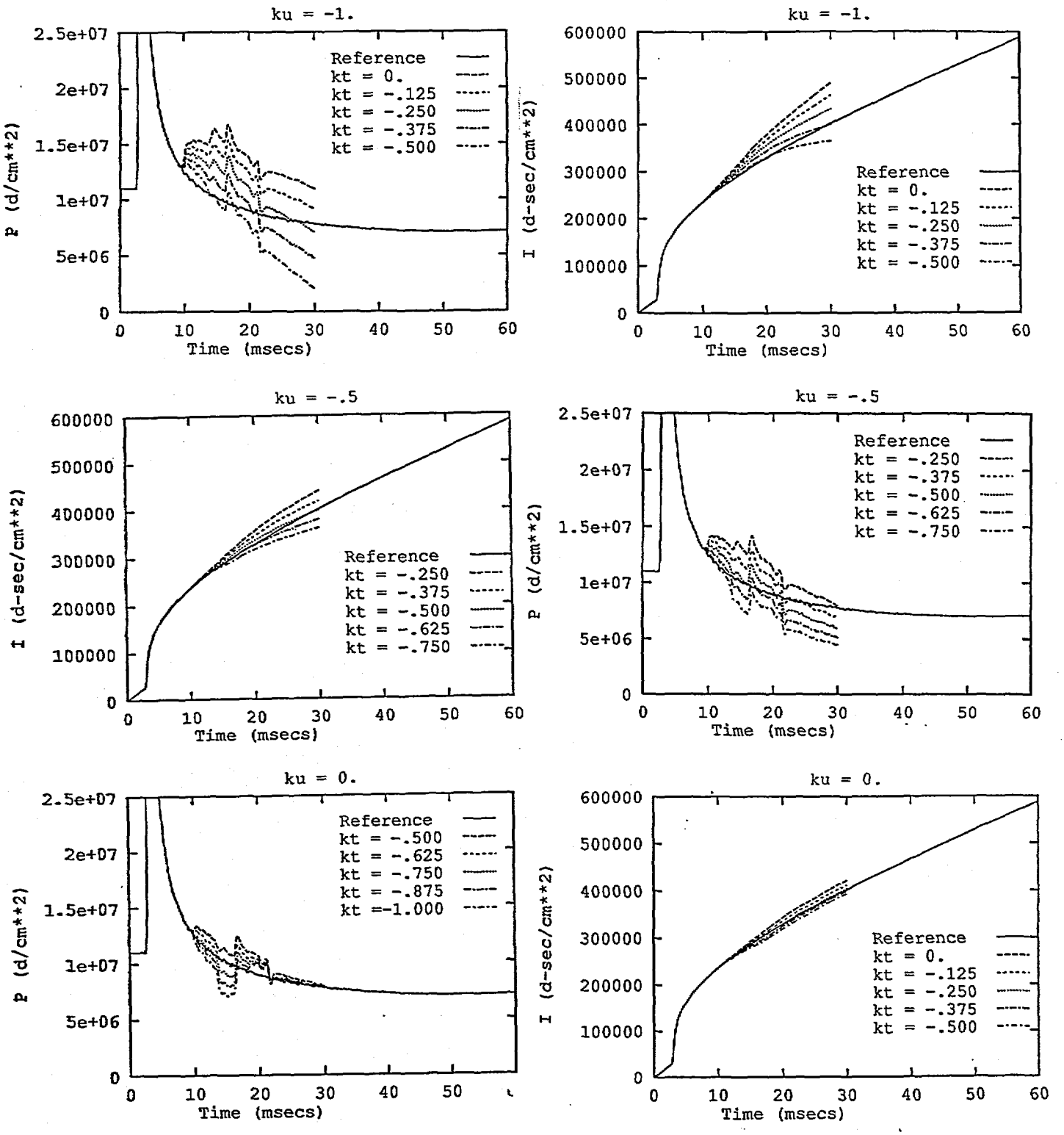

FIGURE 26. INFLUENCE OF k_t AND k_u ON THE 2-D CYLINDRICAL PRESSURE AND IMPULSE AT POINT (100,1) OF A 200X200 CELL UNIFORM MESH AT A DEPTH OF 103.6m

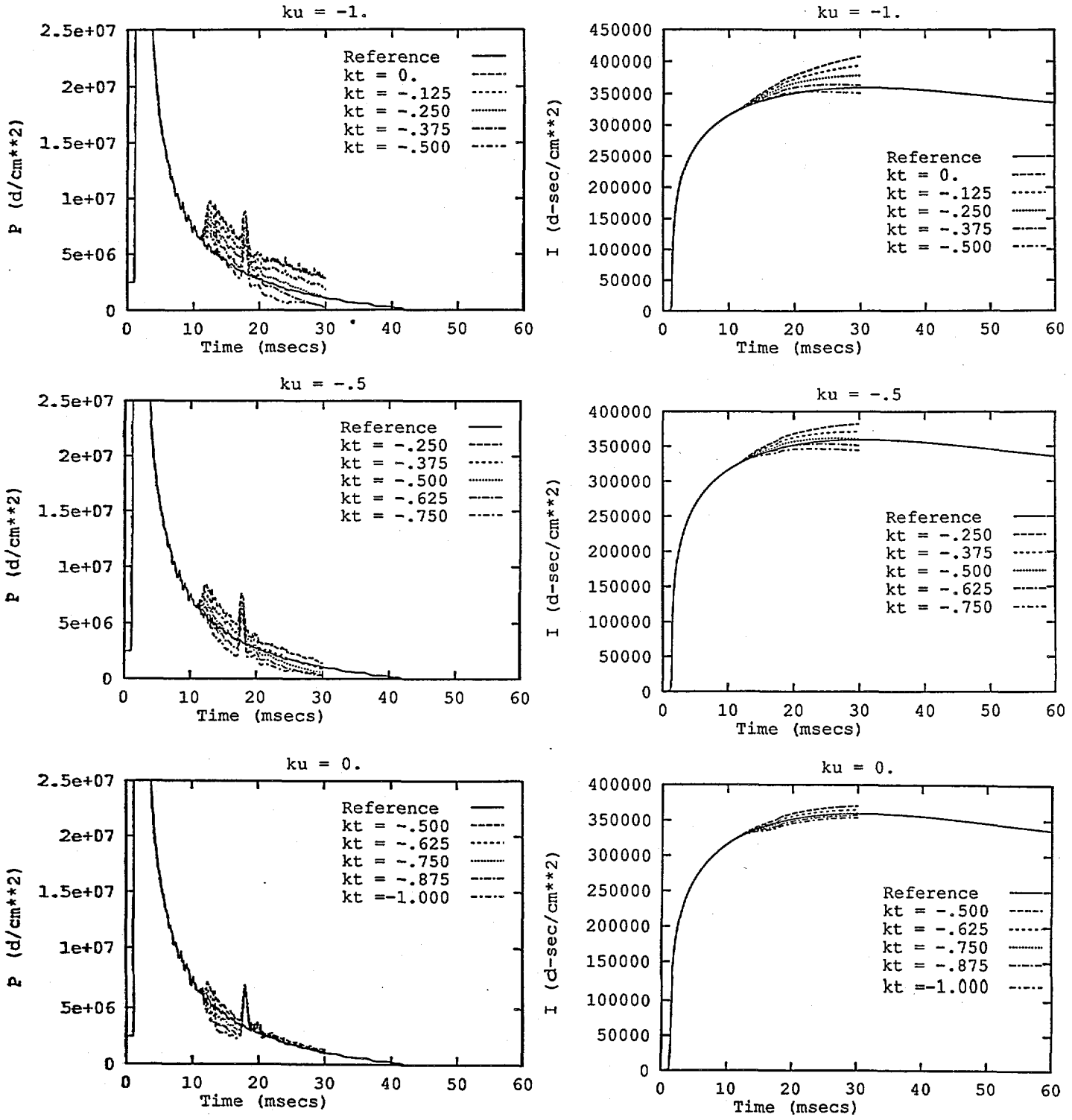

FIGURE 27. INFLUENCE OF k_t AND k_u ON THE 2–D CYLINDRICAL PRESSURE AND IMPULSE AT POINT (50,1) OF A 200X200 CELL UNIFORM MESH AT A DEPTH OF 15.24m

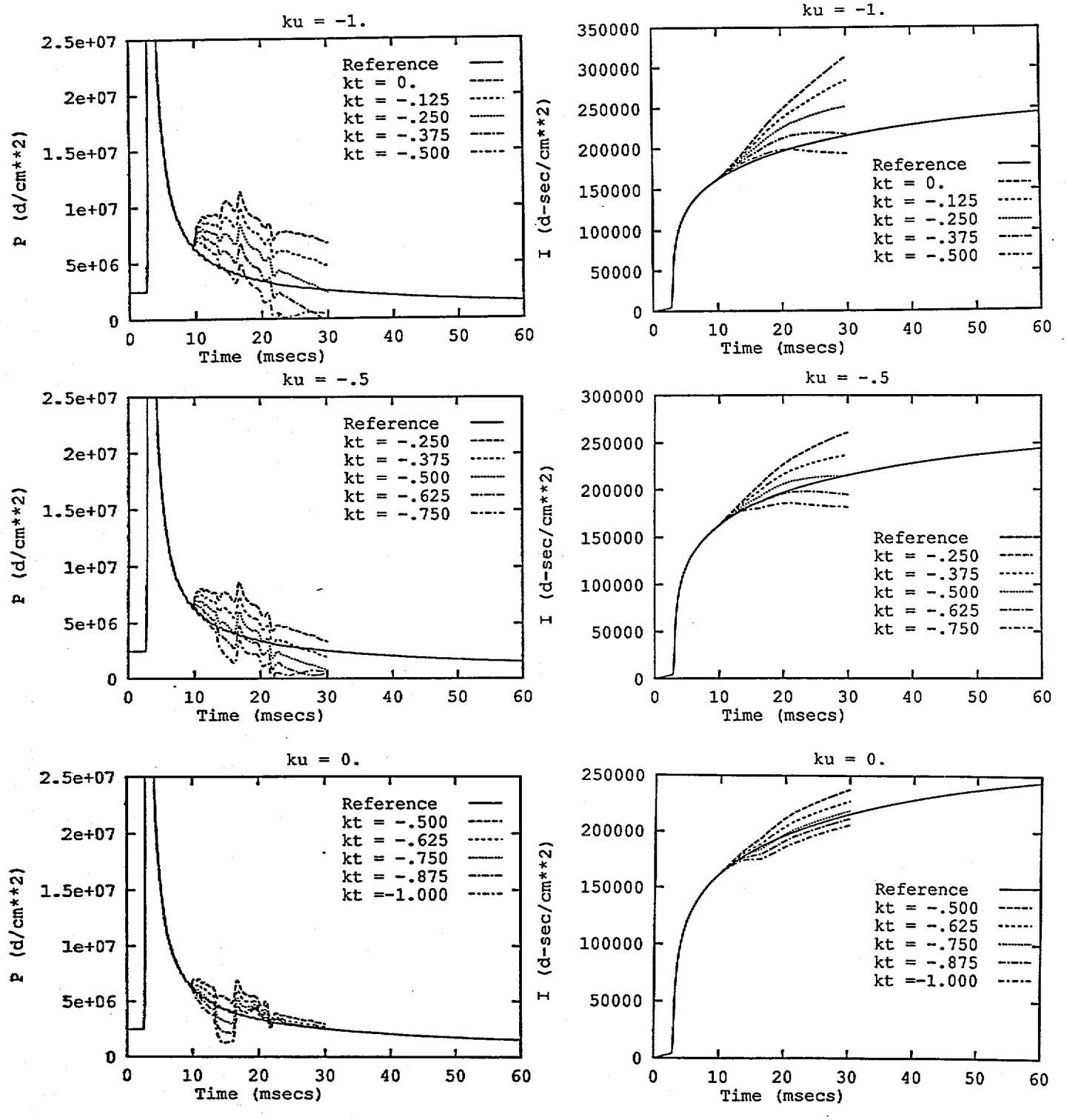

FIGURE 28. INFLUENCE OF k_t AND k_u ON THE 2-D CYLINDRICAL PRESSURE AND IMPULSE AT POINT (100,1) OF A 200X200 CELL UNIFORM MESH AT A DEPTH OF 15.24m

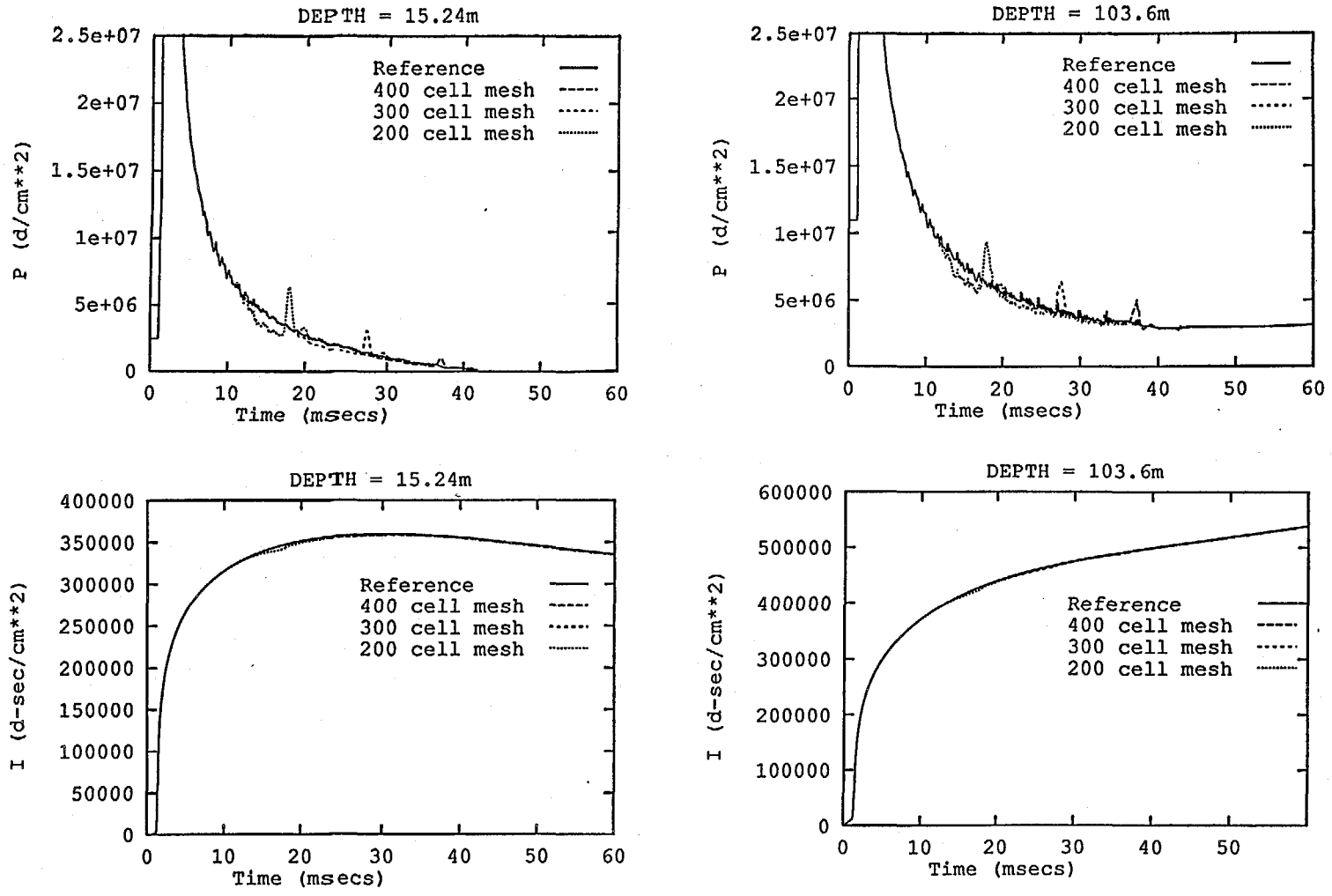

FIGURE 29. COMPARISON OF THE 2–D CYLINDRICAL REFERENCE AND TRIAL PRESSURE AND IMPULSE HISTORIES AT POINT (50,1), DEPTHS 15.24m AND 103.66m, USING DIFFERENT TRIAL MESHES, COMPUTED WITH $k_t = -.85$, $k_u = 0$, $k_c = -2$

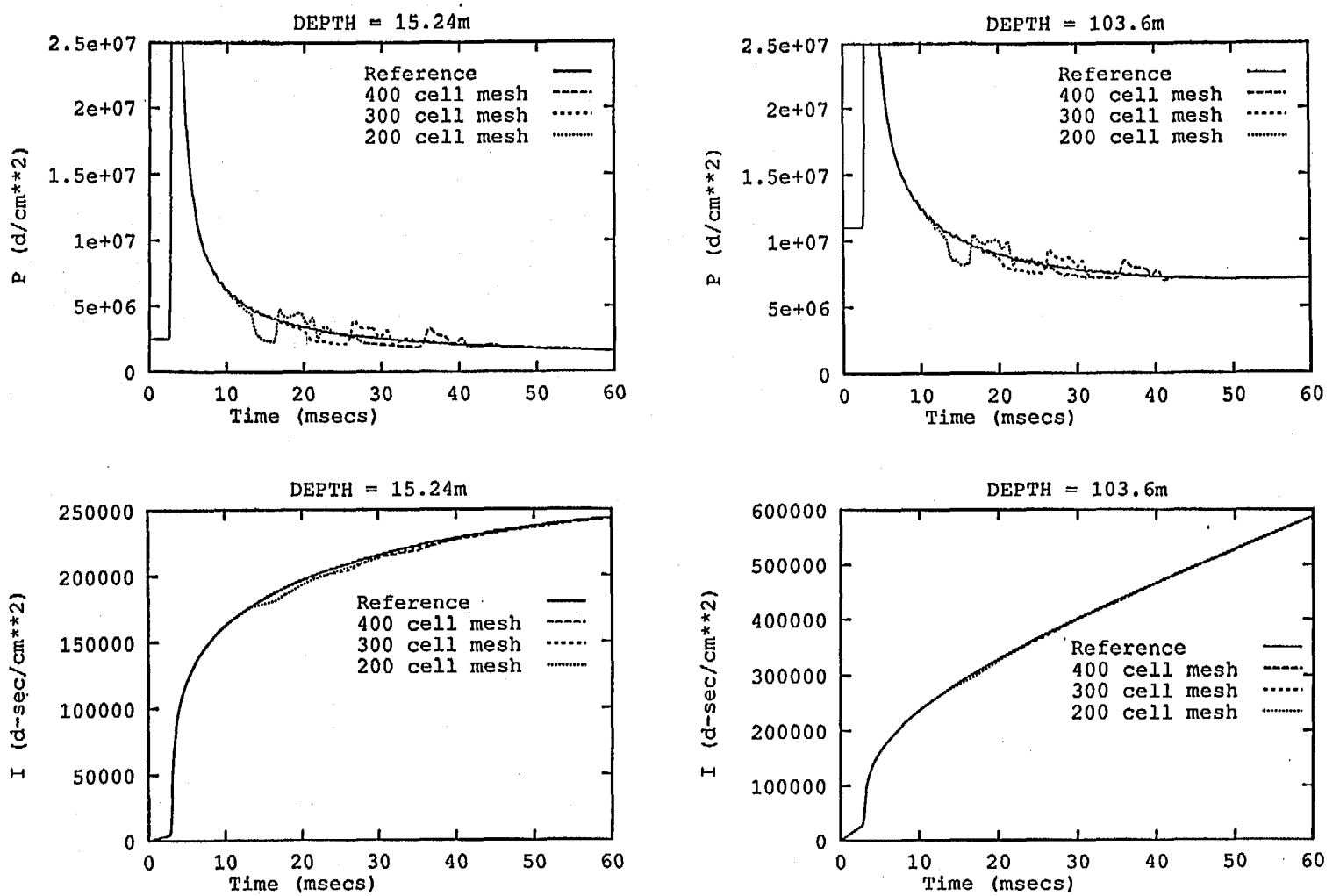

FIGURE 30. COMPARISON OF THE 2–D CYLINDRICAL REFERENCE AND TRIAL PRESSURE AND IMPULSE HISTORIES AT POINT (100,1), DEPTHS 15.24m AND 103.66m, USING DIFFERENT TRIAL MESHES, COMPUTED WITH $k_t = -.85$, $k_u = 0$, $k_c = -2$

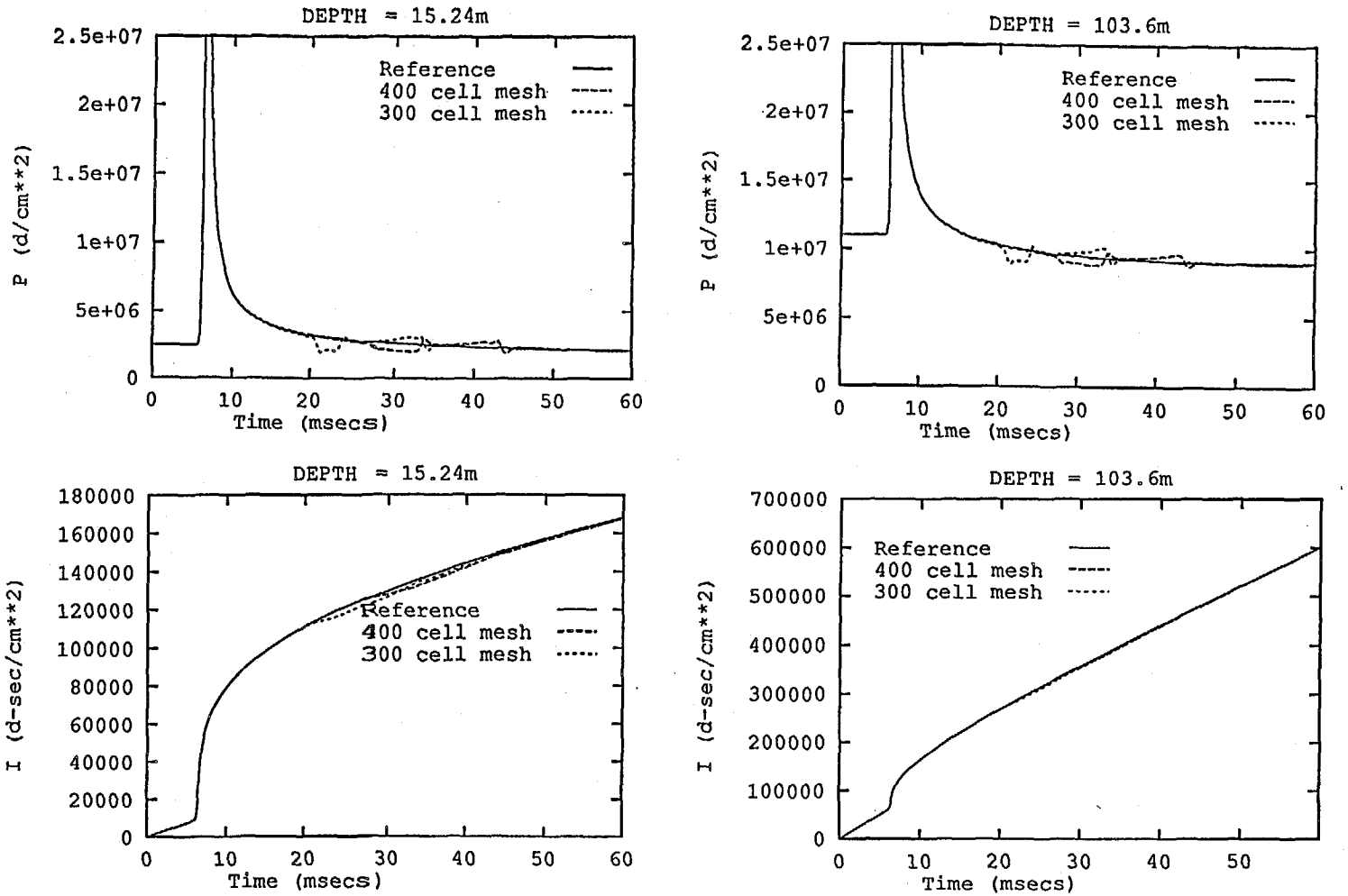

FIGURE 31. COMPARISON OF THE 2–D CYLINDRICAL REFERENCE AND TRIAL PRESSURE AND IMPULSE HISTORIES AT POINT (200,1), DEPTHS 15.24m AND 103.66m, USING DIFFERENT TRIAL MESHES, COMPUTED WITH $k_t = -.85$, $k_u = 0$, $k_c = -2$

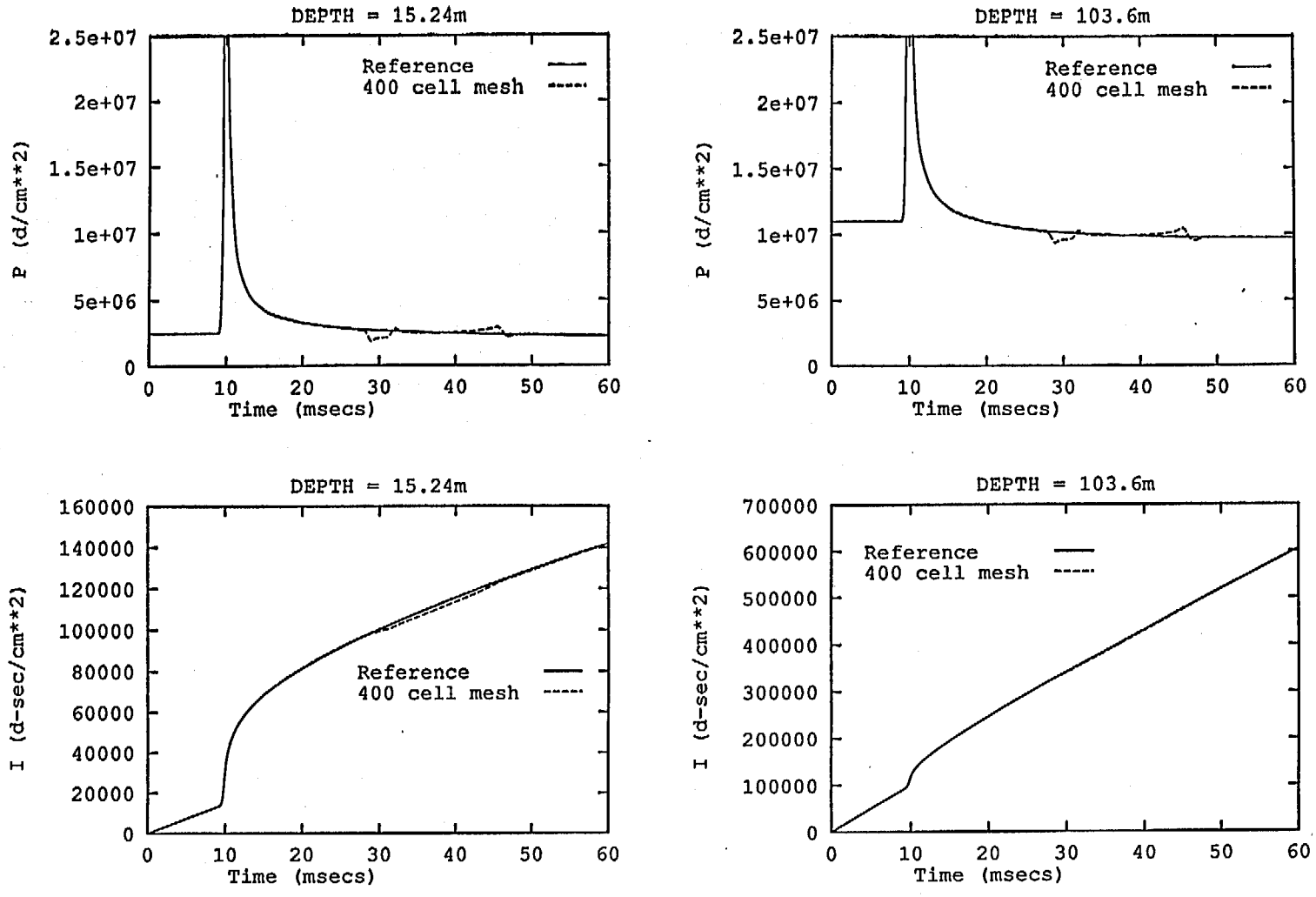

FIGURE 32. COMPARISON OF THE 2–D CYLINDRICAL REFERENCE AND TRIAL PRESSURE AND IMPULSE HISTORIES AT POINT (300,1), DEPTHS 15.24m AND 103.66m, USING A SINGLE TRIAL MESH, COMPUTED WITH $k_t = -.85$, $k_u = 0$, $k_c = -2$

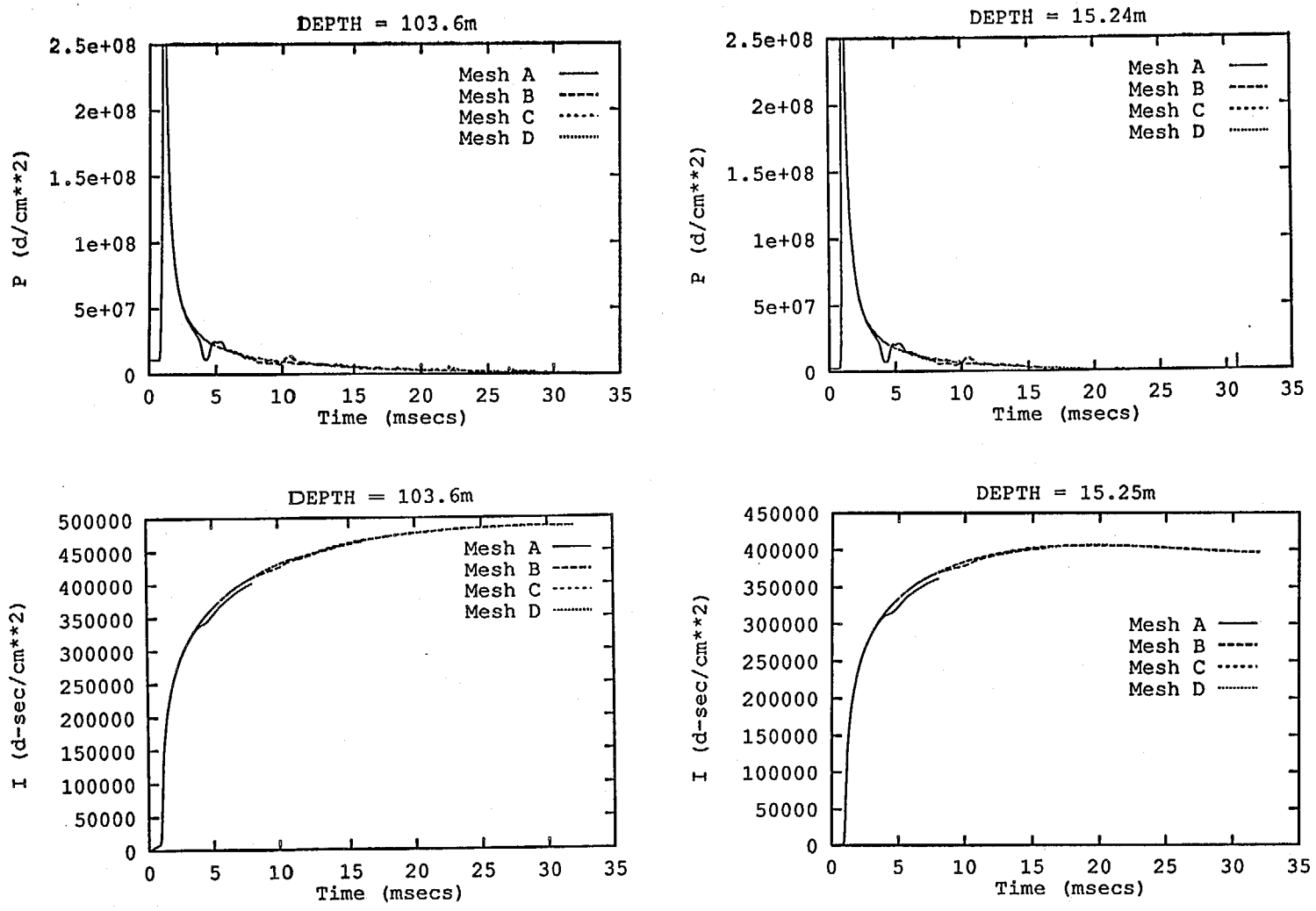

FIGURE 33. COMPARISON OF THE 2-D CYLINDRICAL REFERENCE AND TRIAL PRESSURE AND IMPULSE HISTORIES AT POINT (40,1) ON THE STRETCHED MESH SEQUENCE OF TABLE 1, AT DEPTHS OF 15.24m AND 103.66m, COMPUTED WITH $k_t = -.85$, $k_u = 0$, $k_c = -2$

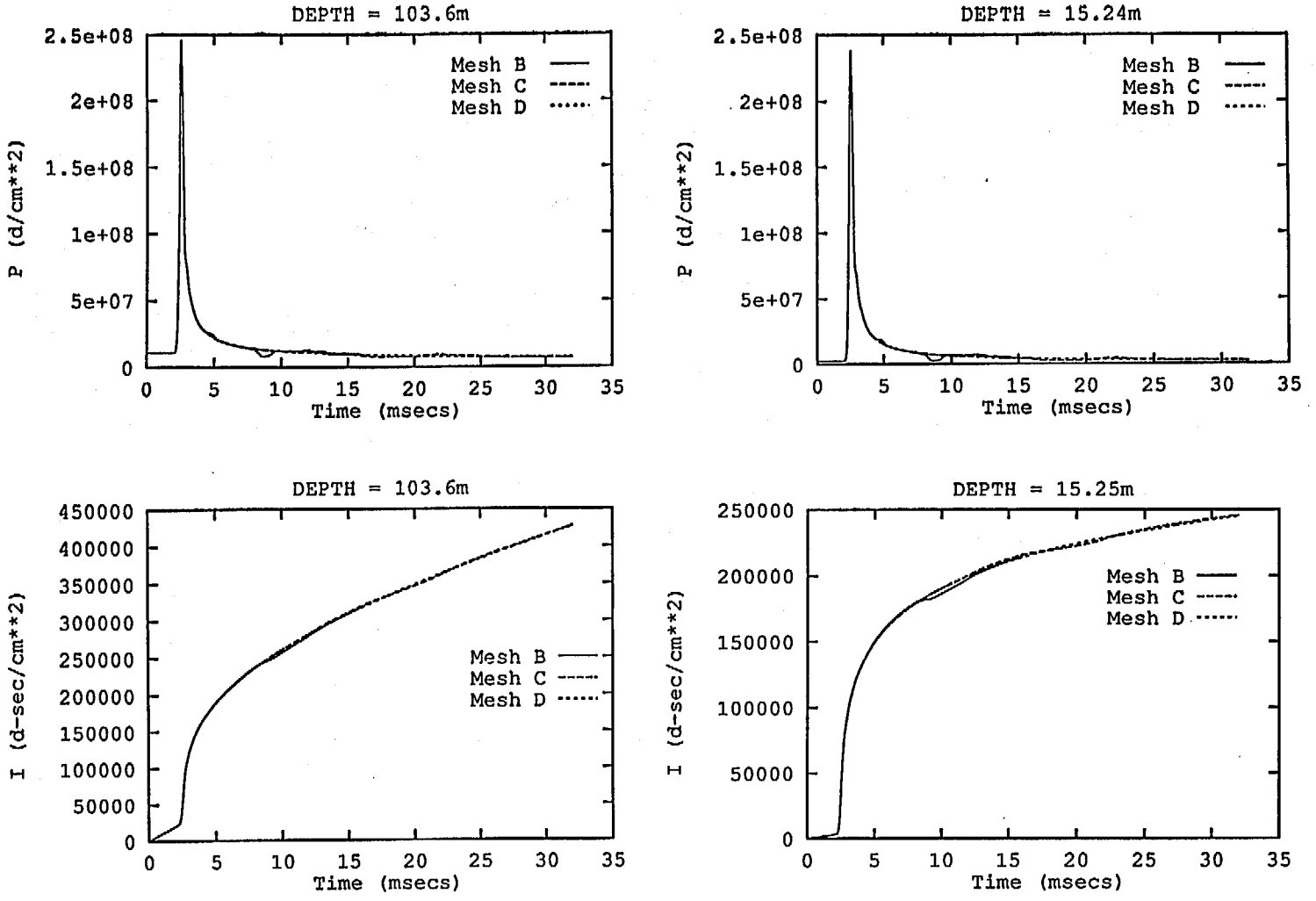

FIGURE 34. COMPARISON OF THE 2–D CYLINDRICAL REFERENCE AND TRIAL PRESSURE AND IMPULSE HISTORIES AT POINT (80,1) ON THE STRETCHED MESH SEQUENCE OF TABLE 1, AT DEPTHS OF 15.24m AND 103.66m, COMPUTED WITH $k_t = -.85$, $k_u = 0$, $k_c = -2$

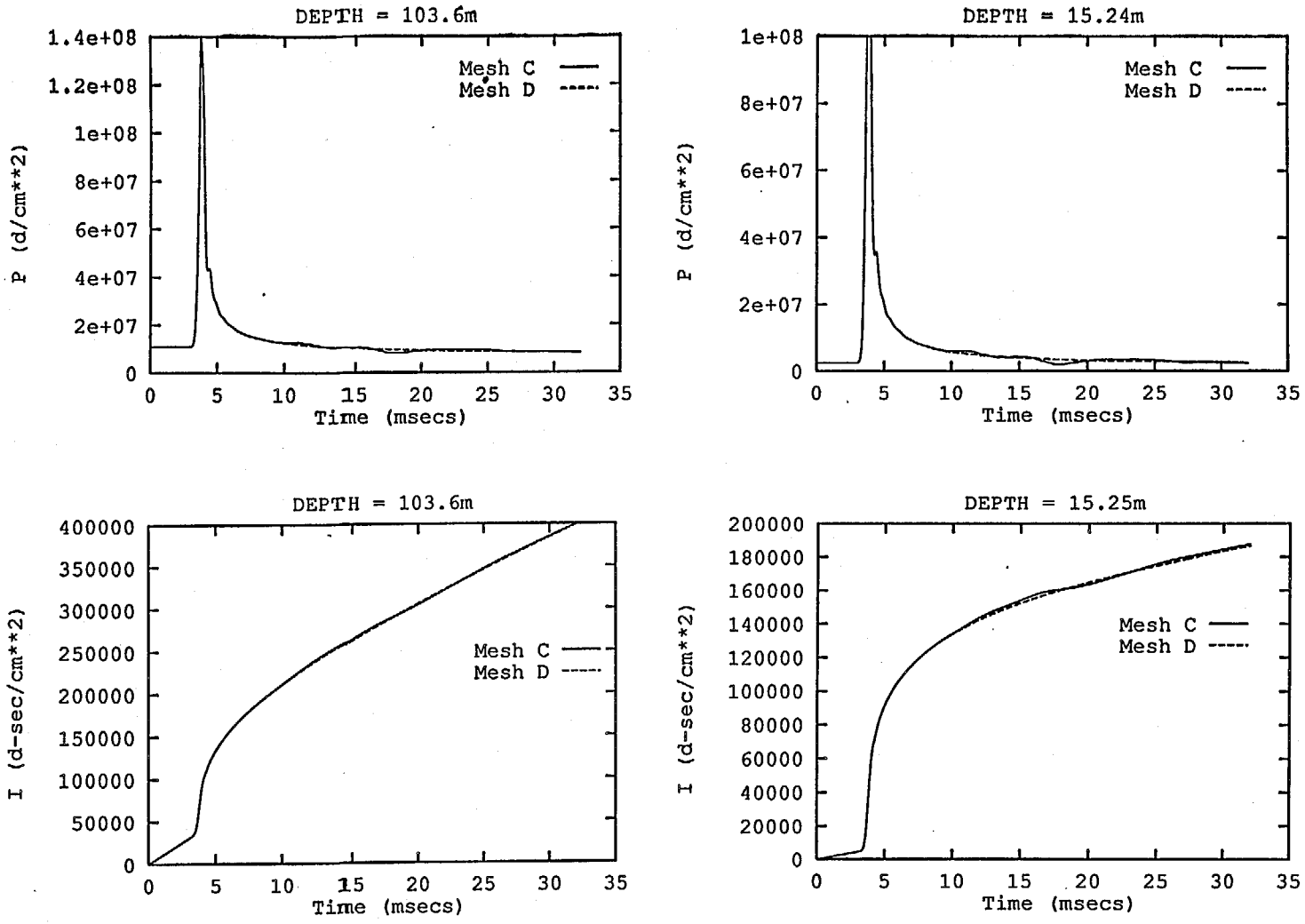

FIGURE 35. COMPARISON OF THE 2-D CYLINDRICAL REFERENCE AND TRIAL PRESSURE AND IMPULSE HISTORIES AT POINT (100,1) ON THE STRETCHED MESH SEQUENCE OF TABLE 1, AT DEPTHS OF 15.24m AND 103.66m, COMPUTED WITH $k_t = -.85$, $k_u = 0$, $k_c = -2$

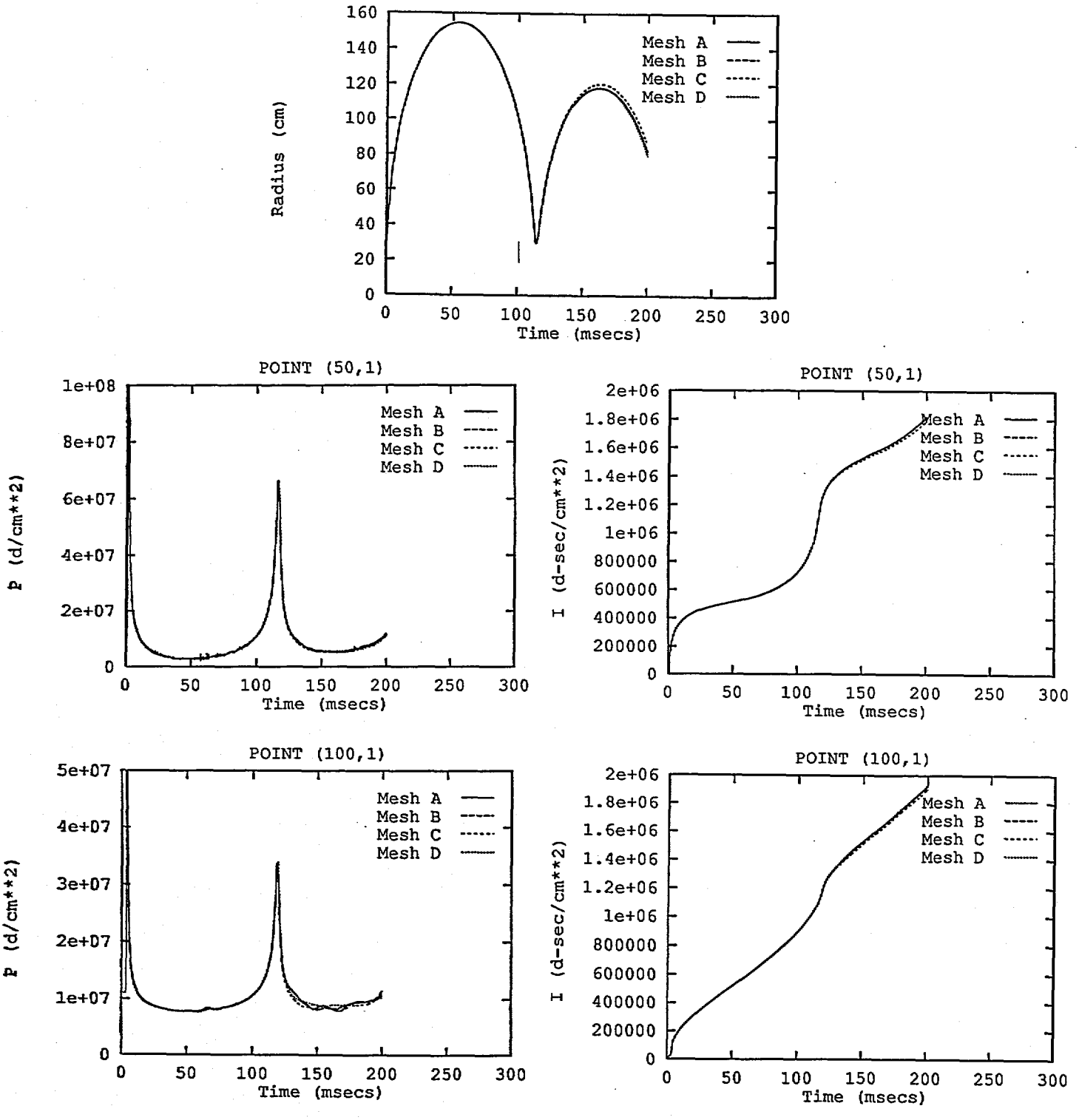

FIGURE 36. COMPARISON OF 2–D CYLINDRICAL BUBBLE PERIODS ON THE MESH SEQUENCE OF TABLE 2 AT A DEPTH OF 103.6m, SHORT PERIOD CASE, COMPUTED WITH $k_t = -.85$, $k_u = 0$, $k_c = -2$

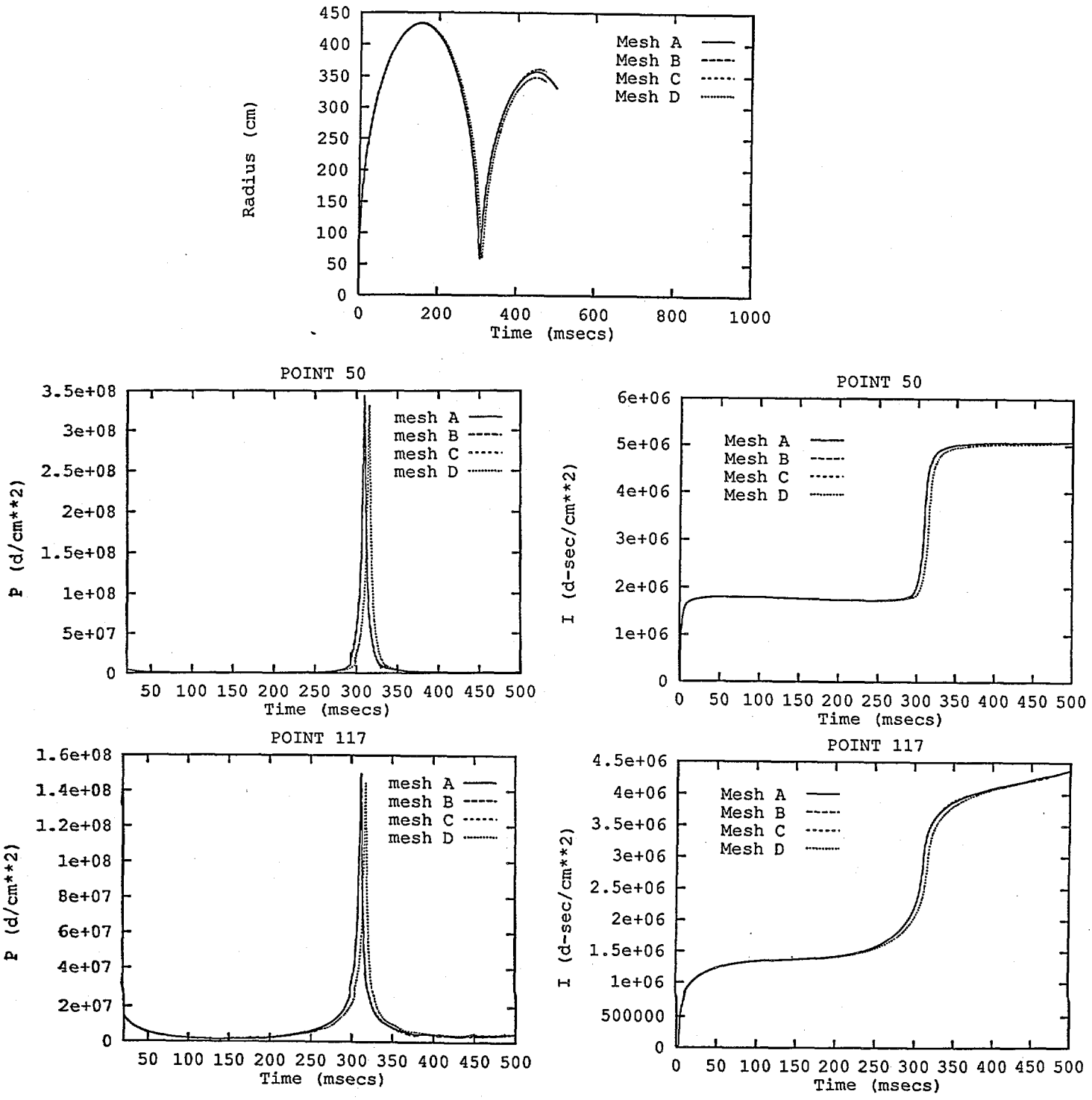

FIGURE 37. COMPARISON OF 2–D CYLINDRICAL BUBBLE PERIODS ON THE MESH SEQUENCE OF TABLE 3 AT A DEPTH OF 103.6m, LONG PERIOD CASE, COMPUTED WITH $k_t = -.85$, $k_u = 0$, $k_c = -2$.

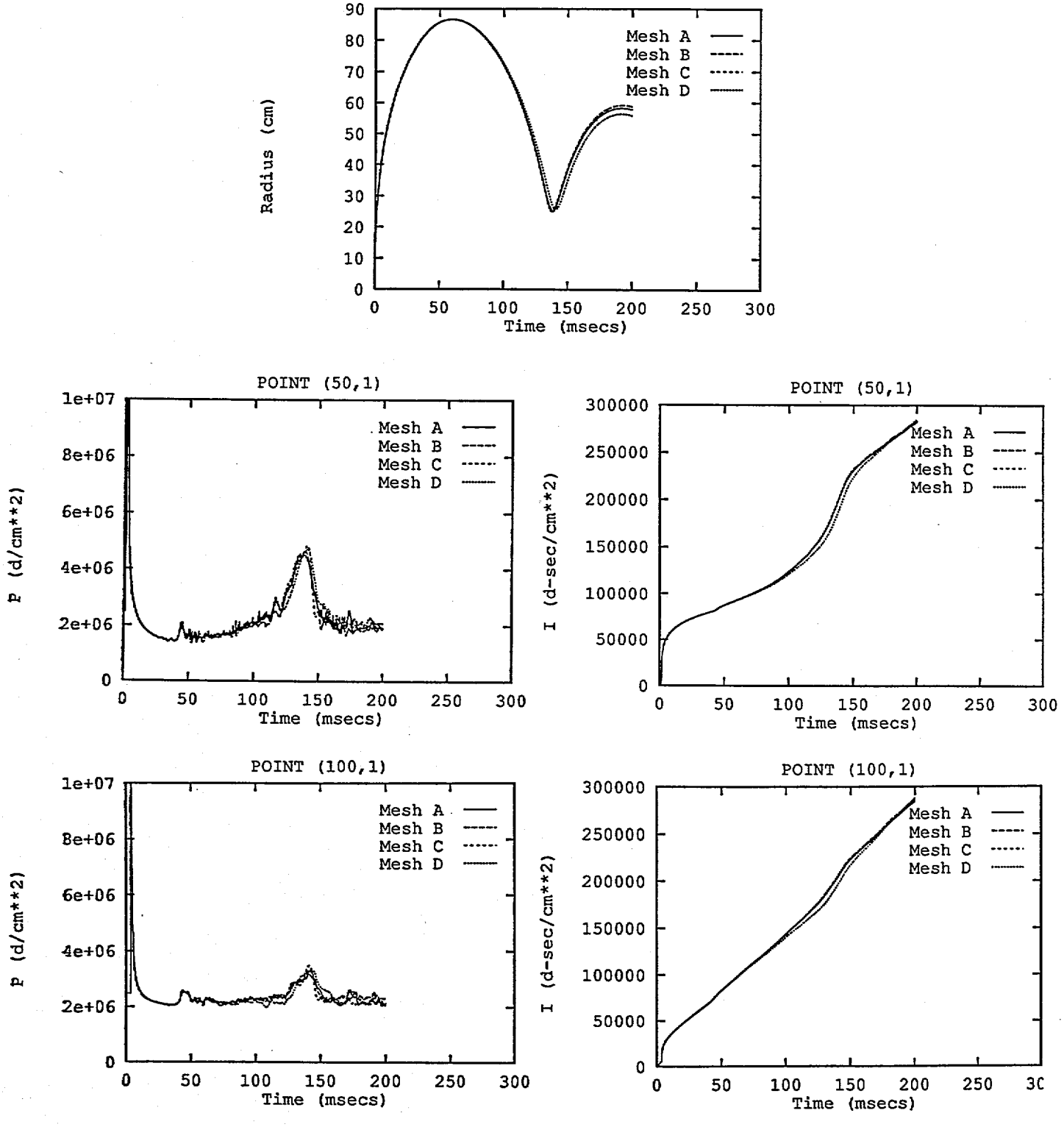

FIGURE 38. COMPARISON OF 2–D CYLINDRICAL BUBBLE PERIODS ON THE MESH SEQUENCE OF TABLE 2 AT A DEPTH OF 15.24m, SHORT PERIOD CASE, COMPUTED WITH $k_t = -.85$, $k_u = 0$, $k_c = -2$

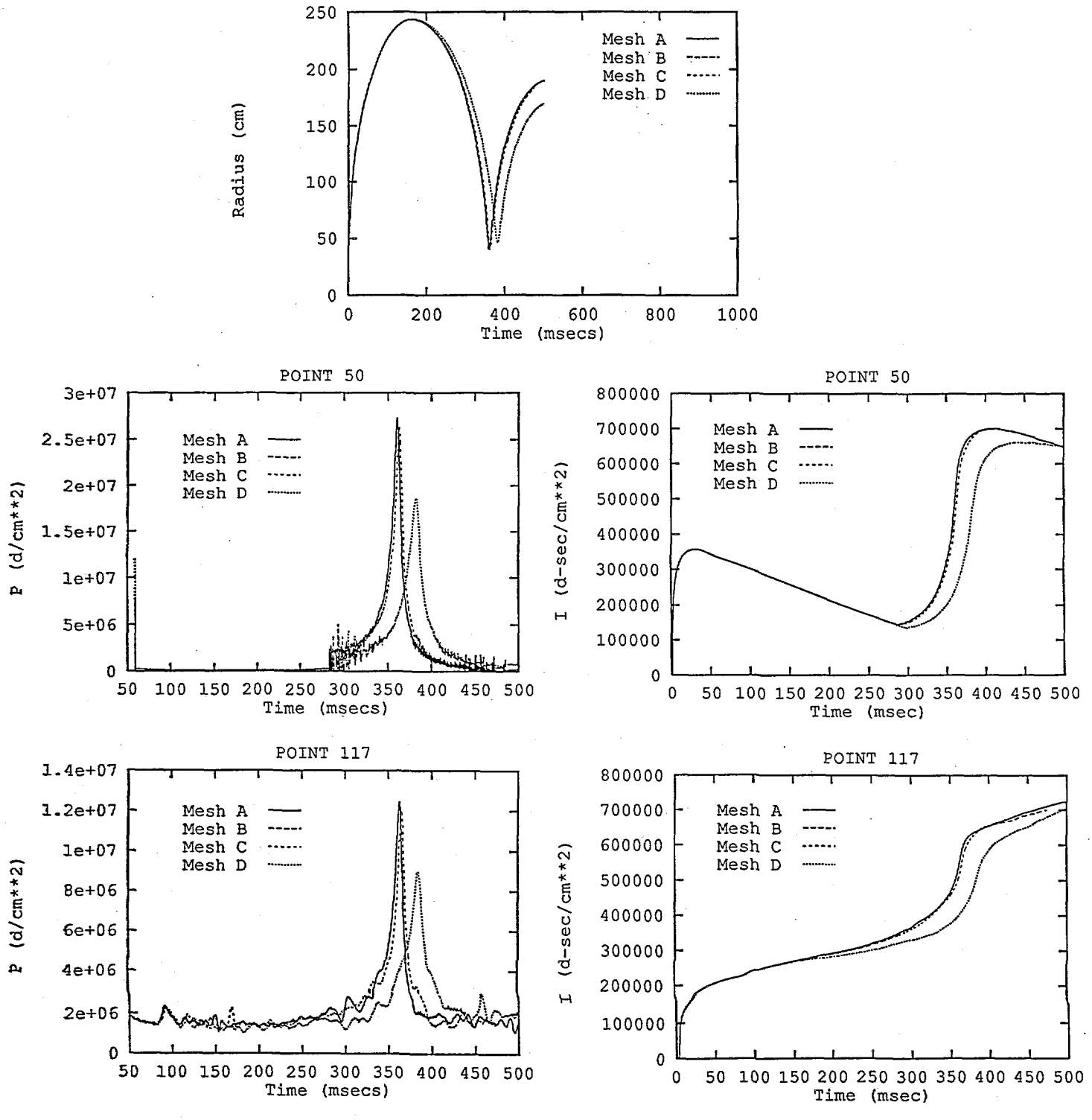

FIGURE 39. COMPARISON OF 2–D CYLINDRICAL BUBBLE PERIODS ON THE MESH SEQUENCE OF TABLE 3 AT A DEPTH OF 15.24m, LONG PERIOD CASE, COMPUTED WITH $k_t = -.85$, $k_u = 0$, $k_c = -2$

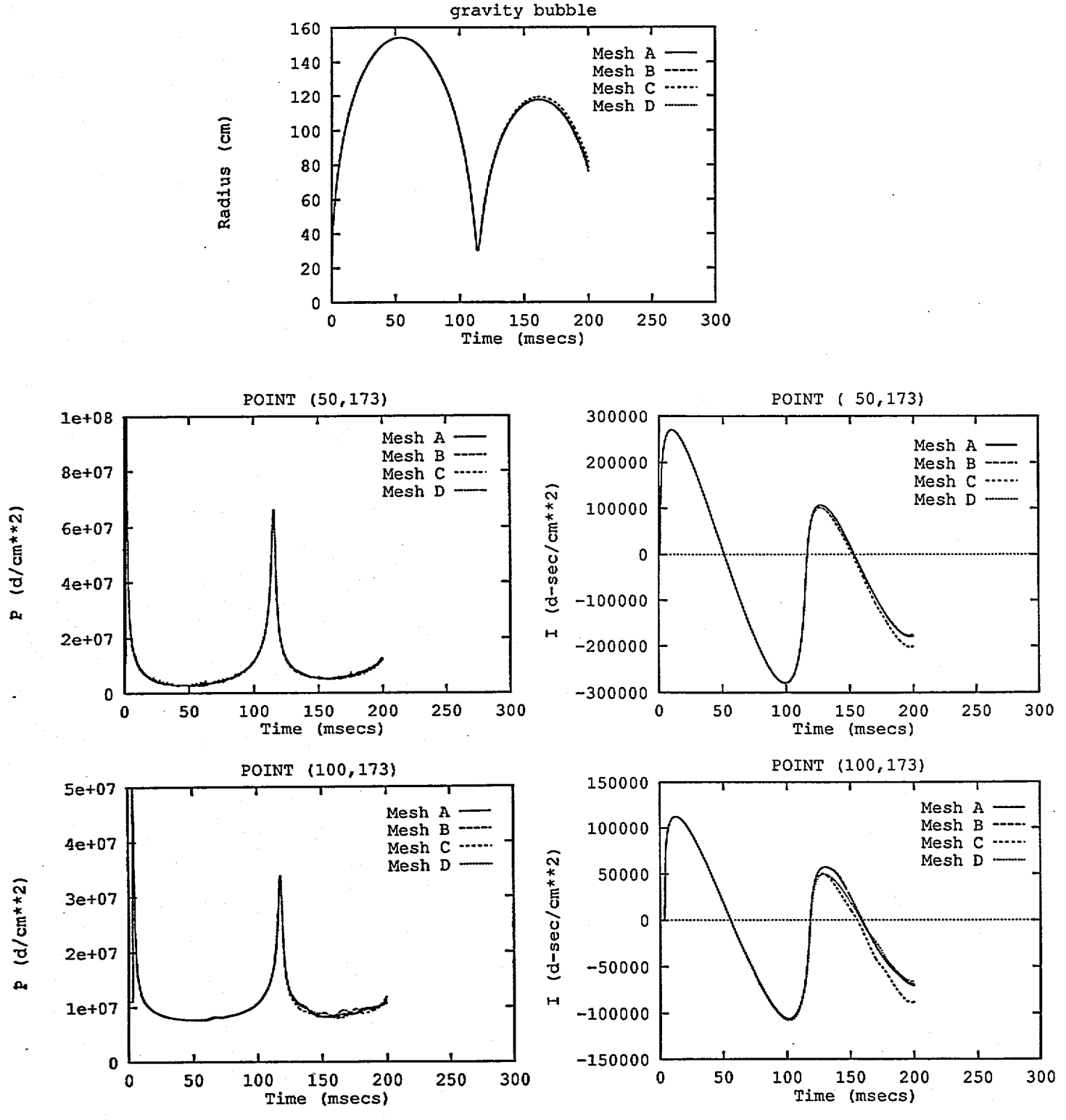

FIGURE 40. COMPARISON OF 2–D CYLINDRICAL BUBBLE PERIODS AT A DEPTH OF 103.6m, INCLUDING GRAVITY. TABLE 5 DEFINES THE r DIRECTION MESH SEQUENCE WHILE THE z DIRECTION MESH IS FIXED, COMPUTED WITH $k_t = -.85$, $k_u = 0$, $k_c = -2$.

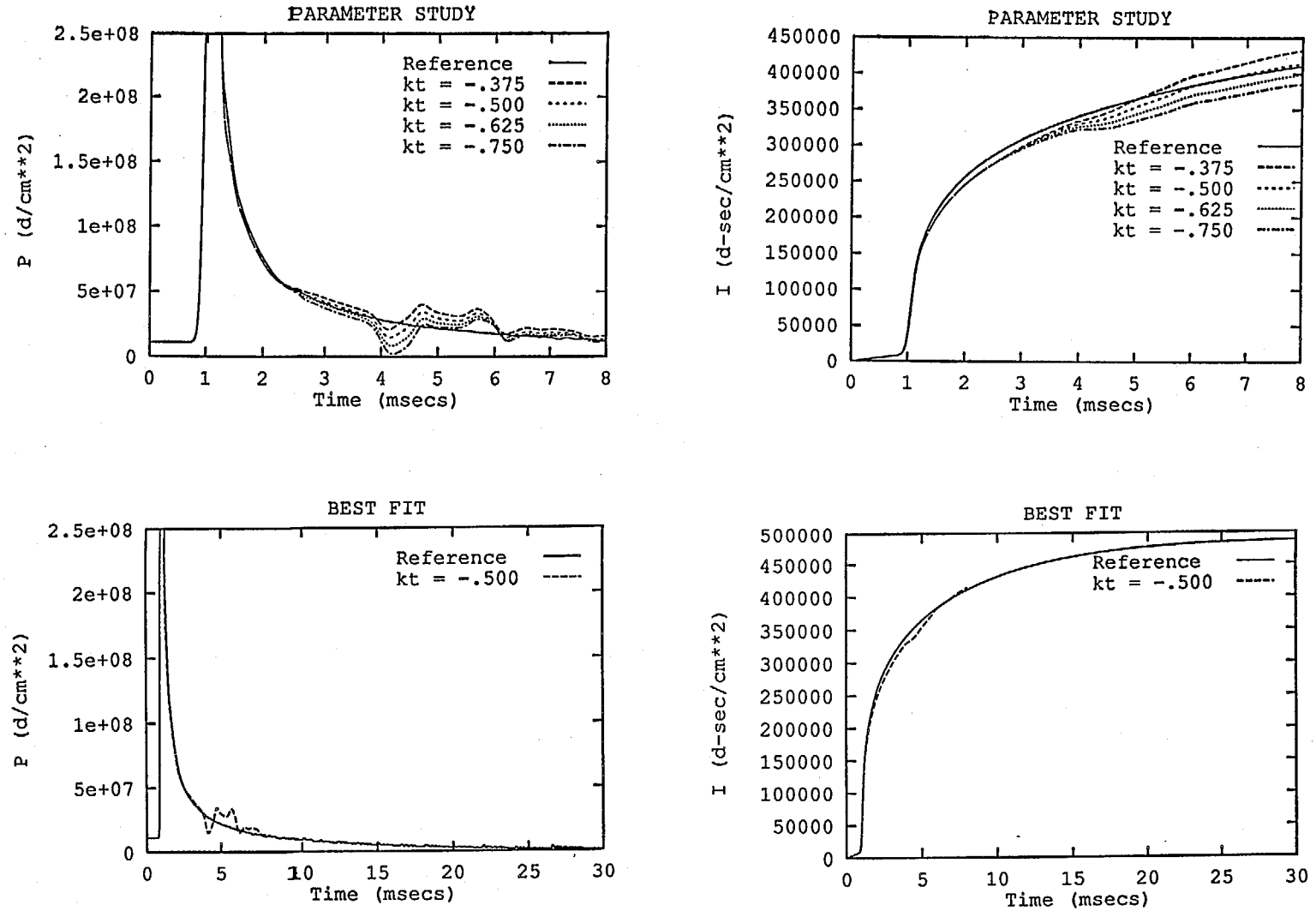

FIGURE 41. INFLUENCE OF k_t ON THE 3–D TRIAL PRESSURE AND IMPULSE HISTORY AT POINT (40,1,1) ON A 61X61X61 CELL UNIFORM MESH AT A DEPTH OF 103.6m, COMPUTED WITH $k_u = 0$ AND $k_c = -2$

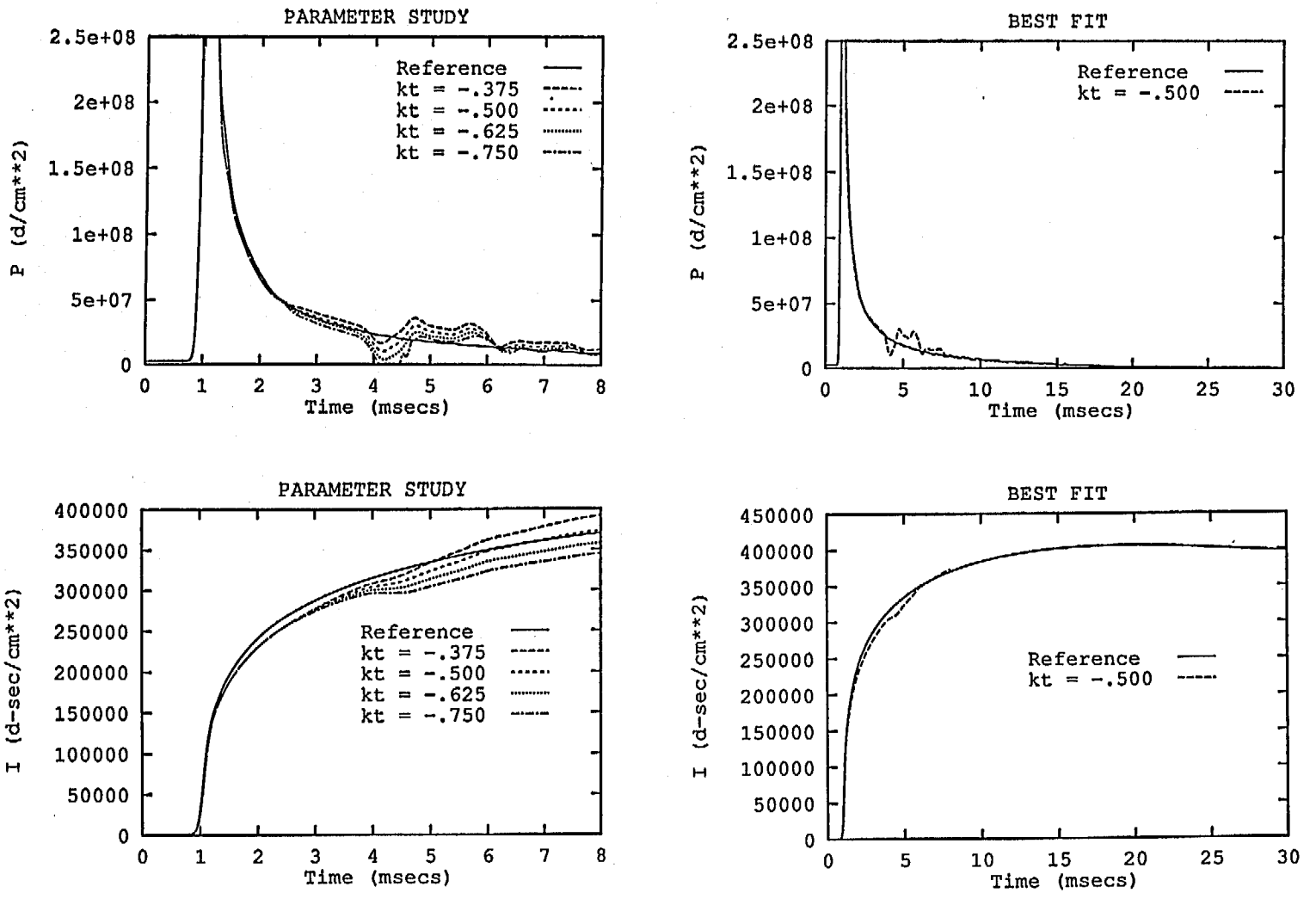

FIGURE 42. INFLUENCE OF k_t ON THE 3–D TRIAL PRESSURE AND IMPULSE HISTORY AT POINT (40,1,1) ON A 61X61X61 CELL UNIFORM MESH AT A DEPTH OF 15.24m, COMPUTED WITH $k_u = 0$ AND $k_c = -2$

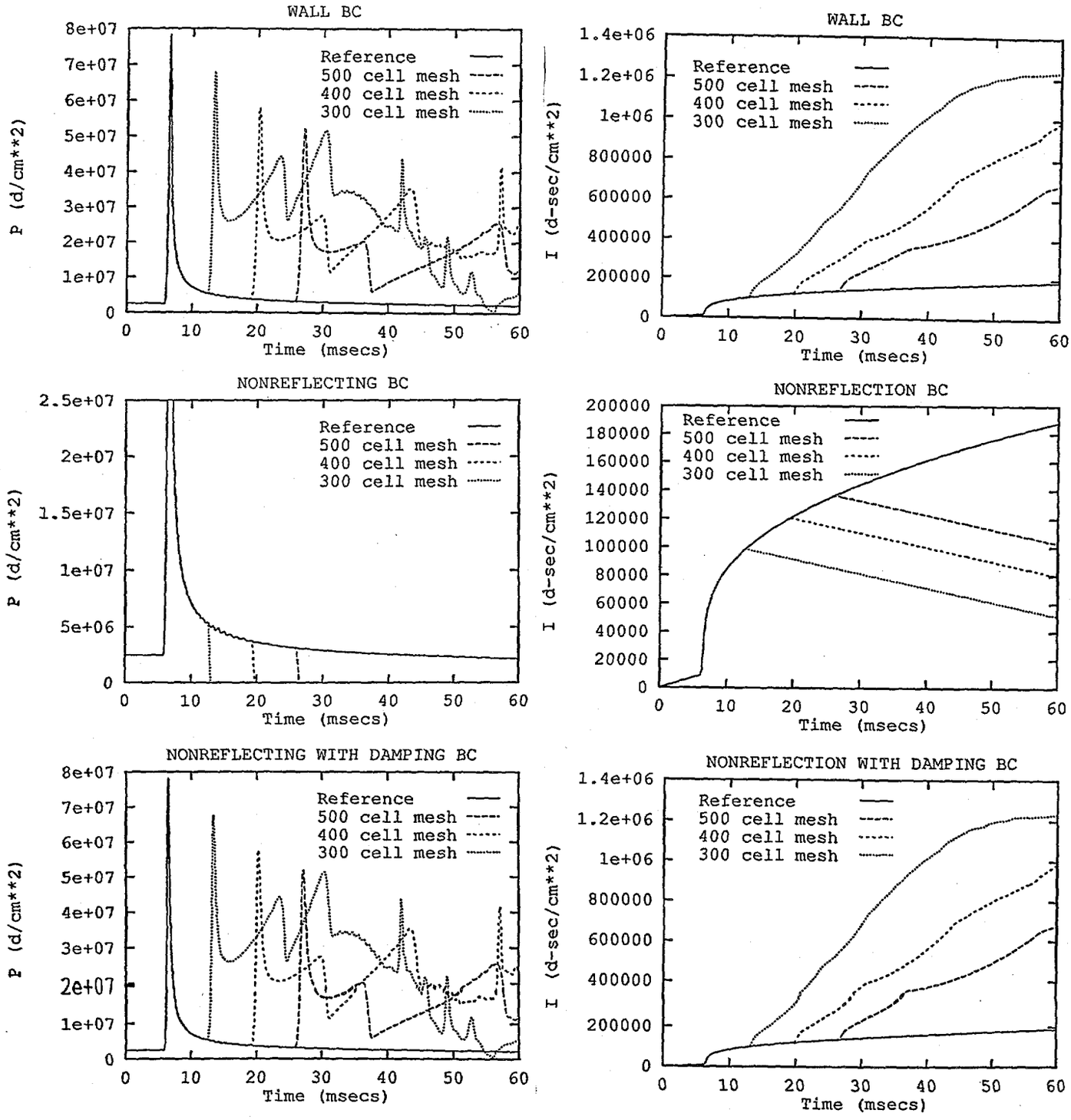

FIGURE 43. COMPARISON OF THE 1–D SPHERICAL REFERENCE AND TRIAL PRESSURE AND IMPULSE HISTORIES AT POINT 200, USING EXISTING DYSMAS BOUNDARY CONDITIONS OPTIONS, COMPUTED AT A DEPTH OF 15.24m WITH THE MESH SEQUENCE OF TABLE 2

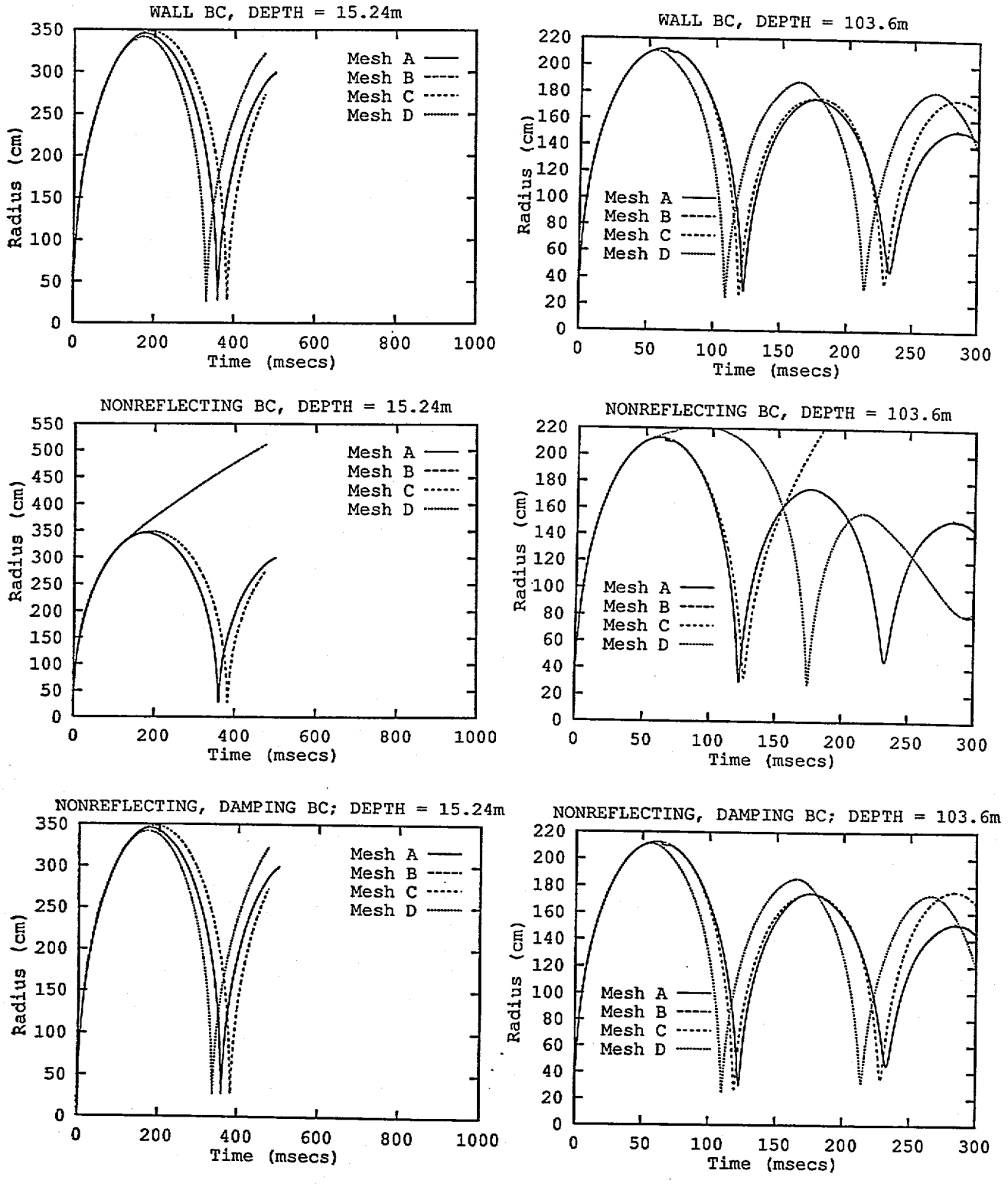

FIGURE 44. COMPARISON OF THE 1–D SPERICAL BUBBLE PERIODS ON THE MESH SEQUENCE OF TABLE 2, AT DEPTHS OF 15.24m AND 103.6m, USING THE EXISTING DYSMAS BOUNDARY CONDITION OPTIONS

TABLE 1 GRIDS FOR FIGURES 17 AND 18

GRID	Number of Points	Boundary Distance	Cells Per Block*			Tr/Tt
			R =1.00	R =1.02	R = 1.10	
A	61	308	61			.07
B	100	608	61	39		.13
C	119	1224	61	39	19	.26
D	130	2586	61	39	30	.55

*Grids consist of up to three blocks, each of which contains cells with the same stretching ratio R.

TABLE 2 GRIDS FOR FIGURES 19 AND 22

GRID	Number of Cells	Boundary Distance	Block 3 cells*	deep Tp/Tr	deep Ti secs.	shallow Tp/Tr	shallow Ti secs.
A	143	25102	43	1.37	.33	1.17	.29
B	137	11680	37	.64	.15	.55	.14
C	133	7113	33	.39	.094	.33	.082
D	129	4415	29	.24	.057	.21	.052

*Each grid consists of three blocks; the first two contain 61 and 39 cells, while the third has a variable number. The stretching factors for the blocks are 1.0, 1.02 and 1.14.

TABLE 3 GRIDS USED IN FIGURES 20 AND 23

GRID	Number of Cells	Boundary Distance	Block 3 cells*	deep Tp/Tr	deep Ti secs.	shallow Tp/Tr	shallow Ti secs.
A	190	62495	50	1.29	.83	1.15	.83
B	184	28762	44	.60	.39	.53	.38
C	181	19615	41	.41	.26	.36	.26
D	176	10506	36	.22	.14	.19	.14

*Each grid consists of three blocks; the first two contain 61 ans 39 celss, while the third has a variable number. The streching factors for the blocks are 1.0, 1.02, and 1.14

TABLE 4 GRIDS USED IN FIGURE 21

GRID	Number of Cells	Boundary Distance	Block 3 cells*	Tp/Tr	Ti secs.
A	117	66448	47	1.19	.88
B	110	26859	40	.48	.35
C	107	18321	37	.33	.25
D	103	11105	33	.20	.15

*Grid s consist of three blocks; the first two contain 49 and 21 cells, while the third has a variable number. The stretching factor for blocks 1, 2, and 3 are 1.0, 1.02, and 1.14.

TABLE 5 GRIDS USED IN FIGURE 24

GRID	Number of Cells	Boundary Distance	Block 3 Cells*	Tp/Tr	Ti secs.
A	96	64309	45	1.00	.85
B	90	29543	39	.46	.39
C	87	20114	36	.31	.26
D	83	12144	32	.19	.16

* Grids consist of three blocks; the first two contain 34 and 17 cells, while the third has a variable number. The stretching factors for blocks 1, 2 and 3 are 1.0, 1.02 and 1.14.

TABLE 6 OPTIMAL VALUES OF k_t k_u *and* k_c

Dimension	k_u	k_t	k_c
1-D planar	0.	0.	0.
1-D spherical	0.	-1.	-2.
2-D cylindrical	0.	-.85	-2.
2-D planar	0.	0.	0.
3-D cartesian	0.	-.5	-2.

Appendix A

User Manual Pages for the Far Field Boundary Conditions

Name: K F F B C
Activates the Far Field Boundary Conditions

Default: KFFBC = 0
Restrictions: 0 or 1
Recommendation: none

Remarks:

KFFBC only has an effect at boundaries which are defined as nonreflecting. At these cells, the new far field boundary conditions are only invoked if KFFBC = 1.

Name: X K C
Far Field Boundary Condition Adjustment

Default:	XKC = 0
Restrictions:	none
Recommendation:	1–D planar: XKC = 0.
	otherwise XKC = –2.

Remarks:

This parameter is k_c in Equation (28). For far field boundaries the behavior of the far field boundary conditions is not very sensitive to this parameter.

Name: X K T
Far Field Boundary Condition Adjustment

Default: XKT = 0
Restrictions: none
Recommendation: 1–D planar: XKT = 0.
1–D Spherical XKT = −1.
2–D XKT = −.85
3–D XKT = −.50

Remarks:

This parameter is k_t in Equation (27) and its value has a strong influence on the performance of the far field boundary conditions.

Name: X K U
Far Field Boundary Condition Adjustment

Default: XKT = 0
Restrictions: none
Recommendation: XKU=1

Remarks:

This parameter is k_u in Equation (27) and its value has a noticeable influence on the performance of the far field boundary conditions.

Appendix B

Implementation of the Far Field Boundary Conditions in DYSMAS

The far field boundary conditions are implemented from WORKEI by calling subroutine BOUNDA in phase 1 of the integration step. This calls the FFBC at each far field boundary point and stores the updated conditions in common block CBOUND. DYSMAS then completes the integration step using the old form of the outflow boundary conditions. At the end of phase 6, BOUNDL is called which, via subroutine LOADNR, which overwrites the far field boundary cells with the conditions computed in FFBC.

The far field boundary conditions require a knowledge of the ambient (initial) density at far field boundary points. The conditions is satisfied by storing the initial density during a cold start within the CELL array at the point previously occupied by PLMAX. This parameters appear to be unused except as a parameter in the SOILC routine. Accordingly, this soil model cannot be used in conjunction with the outflow boundary conditions.

The actual changes and additions made to DYSMAS to introduce the new far field boundary conditions are listed below. Two sets of line numbers are given; the first refers to HP version 402 while the second , which is in parenthesis, refers to the VMS version of 12/93.

```
==> SUBROUTINE BLDCC <==
line 71 (72):
        2      ,'KUN256','KUN257','KELLW ','KOPPL ','KSWINP'
has been replaced by:
        2      ,'KFFBC' ,'KUN257','KELLW ','KOPPL ','KSWINP'

line 91 (92):
        2      ,'XUN356','YUN357','YUN358','ZUN359','ZUN360'/
has been replaced by:
        2      ,'XKC   ','XKT   ','XKU   ','ZUN359','ZUN360'/
```

```
==> SUBROUTINE BOUNDA <==
This subroutine has been added
      SUBROUTINE BOUNDA
C     LOAD FAR FIELD BOUNDARY SOLUTION FOR BOUNDARY GRID POINTS
      INCLUDE 'comdim.cmn'
      INCLUDE 'matdim.cmn'
      COMMON /CSCELL/ CSCEL(MAXCEL)
C     INITIALIZE INDEX
      INDEXB=0
C     FACES 1 AND 4
      ICORDIR=1
      LFACE=7
      DO I=1,IMAX,(IMAX-1)
         LFACE=LFACE-3
         IF(REFLCT(LFACE).EQ.0)THEN
            DO K=1,KMAX
               DO J=1,JMAX
                  IJK=IJKSTA(IGRID)+I+(J-1)*IMAX+(K-1)*IMAX*JMAX
                  MPK=MPKLO(IJK)
                  IF(MPK.GT.0.AND.MPK.LE.NMAT)THEN
                     INDEXB=INDEXB+1
                     CALL NONREF(I,LFACE,ICORDIR,INDEXB)
                  ENDIF
               ENDDO
            ENDDO
         ENDIF
      ENDDO
C     FACES 2 AND 5
      IF(NDIM.GT.1)THEN
         ICORDIR=2
         LFACE=8
         DO J=1,JMAX,(JMAX-1)
            LFACE=LFACE-3
            IF(REFLCT(LFACE).EQ.0)THEN
               DO K=1,KMAX
                  DO I=1,IMAX
                     IJK=IJKSTA(IGRID)+I+(J-1)*IMAX+(K-1)*IMAX*JMAX
                     MPK=MPKLO(IJK)
                     IF(MPK.GT.0.AND.MPK.LE.NMAT)THEN
                        INDEXB=INDEXB+1
                        CALL NONREF(J,LFACE,ICORDIR,INDEXB)
                     ENDIF
                  ENDDO
               ENDDO
            ENDIF
         ENDDO
      ENDIF
C     FACES 3 and 6
      IF(NDIM.GT.2)THEN
         ICORDIR=3
         LFACE=9
         DO K=1,KMAX,(KMAX-1)
            LFACE=LFACE-3
            IF(REFLCT(LFACE).EQ.0)THEN
```

```
               DO J=1,JMAX
                  DO I=1,IMAX
                     IJK=IJKSTA(IGRID)+I+(J-1)*IMAX+(K-1)*IMAX*JMAX
                     MPK=MPKLO(IJK)
                     IF(MPK.GT.0.AND.MPK.LE.NMAT)THEN
                        INDEXB=INDEXB+1
                        CALL NONREF(K,LFACE,ICORDIR,INDEXB)
                     ENDIF
                  ENDDO
               ENDDO
            ENDIF
         ENDDO
      ENDIF

      RETURN
      END


==> SUBROUTINE BOUNDL <==
This subroutine has been added
      SUBROUTINE BOUNDL
C     RELOAD FAR FIELD BOUNDARY SOLUTION FOR BOUNDARY GRID POINTS
      INCLUDE 'comdim.cmn'
C     INITIALIZE INDEX
      INDEXB=0
C     FACES 1 AND 4
      LFACE=7
      ICORDIR=1
      DO I=1,IMAX,(IMAX-1)
         LFACE=LFACE-3
         IF(REFLCT(LFACE).EQ.0)THEN
            DO K=1,KMAX
               DO J=1,JMAX
                  IJK=IJKSTA(IGRID)+I+(J-1)*IMAX+(K-1)*IMAX*JMAX
                  MPK=MPKLO(IJK)
                  IF(MPK.GT.0.AND.MPK.LE.NMAT)THEN
                     INDEXB=INDEXB+1
                     CALL LOADNR(INDEXB,ICORDIR)
                  ENDIF
               ENDDO
            ENDDO
         ENDIF
      ENDDO
C     FACES 2 AND 5
      IF(NDIM.GT.1)THEN
         ICORDIR=2
         LFACE=8
         DO J=1,JMAX,(JMAX-1)
            LFACE=LFACE-3
            IF(REFLCT(LFACE).EQ.0)THEN
               DO K=1,KMAX
                  DO I=1,IMAX
                     IJK=IJKSTA(IGRID)+I+(J-1)*IMAX+(K-1)*IMAX*JMAX
                     MPK=MPKLO(IJK)
```

```
                  IF(MPK.GT.0.AND.MPK.LE.NMAT)THEN
                     INDEXB=INDEXB+1
                     CALL LOADNR(INDEXB,ICORDIR)
                  ENDIF
               ENDDO
            ENDDO
         ENDIF
      ENDDO
   ENDIF
C  FACES 3 and 6
   IF(NDIM.GT.2)THEN
      ICORDIR=3
      LFACE=9
      DO K=1,KMAX,(KMAX-1)
         LFACE=LFACE-3
         IF(REFLCT(LFACE).EQ.0)THEN
            DO J=1,JMAX
               DO I=1,IMAX
                  IJK=IJKSTA(IGRID)+I+(J-1)*IMAX+(K-1)*IMAX*JMAX
                  MPK=MPKLO(IJK)
                  IF(MPK.GT.0.AND.MPK.LE.NMAT)THEN
                     INDEXB=INDEXB+1
                     CALL LOADNR(INDEXB,ICORDIR)
                  ENDIF
               ENDDO
            ENDDO
         ENDIF
      ENDDO
   ENDIF

   RETURN
   END
```

```
==> SUBROUTINE INPDST <==
following line 182 (183), the following new lines have been inserted
        IF (MAT(NP).EQ.1.OR.MAT(NP).EQ.8) THEN
           PLMAX = DRHOC(NP)
        ENDIF

==> SUBROUTINE INPPST <==
following line 204 (205), the following new lines have been inserted
        IF (MAT(NP).EQ.1.OR.MAT(NP).EQ.8) THEN
           PLMAX = DRHOC(NP)
        ENDIF

==> SUBROUTINE LOADNR <==
This subroutine has been added
```

```
      SUBROUTINE LOADNR(INDEXB,ICORDIR)
C     LOAD MOC VALUES FOR BOUNDARY POINT
      INCLUDE 'comdim.cmn'
      INCLUDE 'cbound.cmn'
         LOC=KELLO(IJK)
         CELL(LOC+2)=DEEX(INDEXB)
         CELL(LOC+3)=DRHOEX(INDEXB)
         CELL(LOC+3+ICORDIR)=VELEX(INDEXB)
         CELL(LOC+4+NDIM)=PEX(INDEXB)
      RETURN
      END
```

==> SUBROUTINE NONREF <==
This subroutine has been added

```
      SUBROUTINE NONREF(INDIJK,LFACE,ICORDIR,INDEXB)
C     MOC SOLUTION FOR OUTER GRID POINT. REFERENCE NSWC/TR-94/20
C     ARGUMENTS:
C        INDIJK - I,J or K index of boundary point for (J,K),(I,K),(I,J)
C                 surfaces respectively
C        LFACE - Grid face of point IJK (e.g. 1 for point (IMAX,J1,K1))
C                follows numbering convention for cell faces.
C        ICORDIR - Coordinate direction: 1,2,3 for x,y,z respectively
C        INDEXB - storage index for results from MOC solution
C
C     APPLICABLE ONLY TO PURE CELLS
      INCLUDE 'comdim.cmn'
      INCLUDE 'matdim.cmn'
      COMMON /CSCELL/ CSCEL(MAXCEL)
      INCLUDE 'cbound.cmn'
C     Check available boundary cell storage
      IF(INDEXB.GT.NSIZE)STOP'TOO MANY BOUNDARY CELLS,INCREASE NSIZE'
C     Determine Neighbor Face INDEX
         NFACE=(LFACE+3)-6*((LFACE+3)/7)
         IJKNB=KONNEC(NFACE,IJK)
         NDIS=-1+2*(LFACE/4)
         ISIGN=-NDIS
C     Load Cell Geometry
         RADIUS=CELL(LXYZ(ICORDIR)+INDIJK)
         DELTAR=.5*( CELL(LDCL(ICORDIR)+INDIJK+NDIS)
     &              +CELL(LDCL(ICORDIR)+INDIJK     ))
C     Load Cell Properties
         CALL CELGET
         RHOINF=PLMAX+RHO0(MPK)
C     Load neighboring cell properties
         CALL NGHBRS
C     Compute source terms for Equations 27 and 28 of NSWC/TR-94/20
         DUDR= ISIGN*(VELACT(ICORDIR)-VELNB(ICORDIR,NFACE))/DELTAR
         DPDR= ISIGN*(PRESUR          -PRSNB(NFACE)        )/DELTAR
         TRHO= (DRHOC(MPK)+RHO0(MPK))
         CRHO= TRHO*CSCEL(IJK)
C        known Q
         TERMK=XKC*CRHO*CSCEL(IJK)*VELACT(ICORDIR)/RADIUS
         XLAMDA=VELACT(ICORDIR)+ISIGN*CSCEL(IJK)
```

```
          QKNOW=TERMK-XLAMDA*(DPDR+ISIGN*CRHO*DUDR)
C         unknown Q
          TERMU=CRHO*CSCEL(IJK)/RADIUS
          CBARU=CSCEL(IJK)*ALOG(TRHO/RHOINF)
          QMISS=XKT*TERMU*(XKU*VELACT(ICORDIR)+(1.-XKU)*CBARU)
          IF(ISIGN.GT.0)THEN
             QPLUS=QKNOW
             QMINUS=QMISS
          ELSE
             QPLUS=QMISS
             QMINUS=QKNOW
          ENDIF
C     Compute p u derivatives, Equations 26 and 25 of NSWC/TR-94/20
          DPDT=.5*(QPLUS+QMINUS)
          DUDT=.5*(QPLUS-QMINUS)/CRHO+GRAV(ICORDIR)
C     Advance p, u, rho, and e from Equations 29 of NSWC/TR-94/20
          PEX(INDEXB)=PRESUR+DT*DPDT
          VELEX(INDEXB)=VELACT(ICORDIR)+DT*DUDT
          DRHOEX(INDEXB)=DRHOC(MPK)+DT*DPDT/CSCEL(IJK)**2
          COEFEXP=.5*(PRESUR+PEX(INDEXB))/
     &               (RHO0(MPK)+.5*(DRHOC(MPK)+DRHOEX(INDEXB)))**2
          DEEX(INDEXB)=DSIEC(MPK)+COEFEXP*(DRHOEX(INDEXB)-DRHOC(MPK))S ()
       RETURN
       END

==> SUBROUTINE PRSCEL <==
Line 340 (341) of has been deleted
        PLMAX = AMAX1(PLMAX,PRESUR)

==> SUBROUTINE PRSINI <==
Line 69 (70):
     50          PLMAX = AMAX1(PRESUR,PLMAX)
has been replaced by
     50          CONTINUE

==> SUBROUTINE UPDGRV <==
After line 105 (106), the following line has been added:
        PLMAX=DRHO
After line 119 (120), the following line has been added:
        PLMAX=DRHO

==> SUBROUTINE WORKEI <==
After line 148 (150), the folloing lines have been added:
  C     Compute New Outflow BC if KFFBC=1
        IF(KFFBC.EQ.1)CALL BOUNDA
After line 229 (231), the folloing lines have been added:
  C     Load New Outflow BC if KFFBC=1
        IF(KFFBC.EQ.1)CALL BOUNDL

==> INCLUDE FILE comdim.cmn <==
Line 107 (107):
       2      ,KUN256   ,KUN257   ,KELLW    ,KOPPL    ,KSWINP
has been replaced by:
       2      ,KFFBC    ,KUN257   ,KELLW    ,KOPPL    ,KSWINP
```

```
Line 127 (127):
      2      ,XUN356    ,YUN357    ,YUN358    ,ZUN359    ,ZUN360
has been replaced by:
      2      ,XKC       ,XKT       ,XKU       ,ZUN359    ,ZUN360

==> INCLUDE FILE cbound.cmn <==
This file has been added:

       PARAMETER(NSIZE = 40000)
       COMMON /CBOUND/UEX(NSIZE),VELEX(NSIZE),PEX(NSIZE),DRHOEX(NSIZE),
      &               DEEX(NSIZE)
```

Appendix C

The Impact of Mesh Stretching on Bubble Period and Peak Pressure

An alternative to using a FFBC is to employ a mesh which is highly stretched near the outer boundary. For a short calculation the FFBC performs well and such an approach is not necessary. However, for long calculations at shallow depth, the FFBC is less effective and mesh stretching may be a viable alternative. Figure C-1 examines the influence of mesh stretching on the computed bubble period and peak pressure. The six different stretchings given in Table C-1 are applied to the outer cells, in conjunction with wall boundary conditions. In each case the mesh consists of the same inner region followed by a region of highly stretched cells, subject to the constraint of a fixed mesh width. This width is large enough to prevent the influence of the refected shock from arriving back at the bubble before the end of the calculation. Hence, any differences between the computations on these meshes is a consequence of the stretched mesh. As is indicated by the results in Figure C-1, the error induced by the stretched outer mesh has only a small effect on the bubble period, but a larger influence on the maximum pressure.

TABLE C-1. GRIDS USED IN THE STRETCHED MESH STUDY

Grid	Number of cells in outer region*	Outer region stretching ratio	Maximum (outer) cell width	Total mesh width
A	156	1.100	2275	24911
B	143	1.141	3093	24911
C	136	1.176	3736	24903
D	130	1.223	4546	24908
E	125	1.282	5502	24929

*Each mesh consists of 61 uniform cells, followed by 39 cells with a stretching ratio of 1.02, and concluded with an outer region with a variable number of cells.

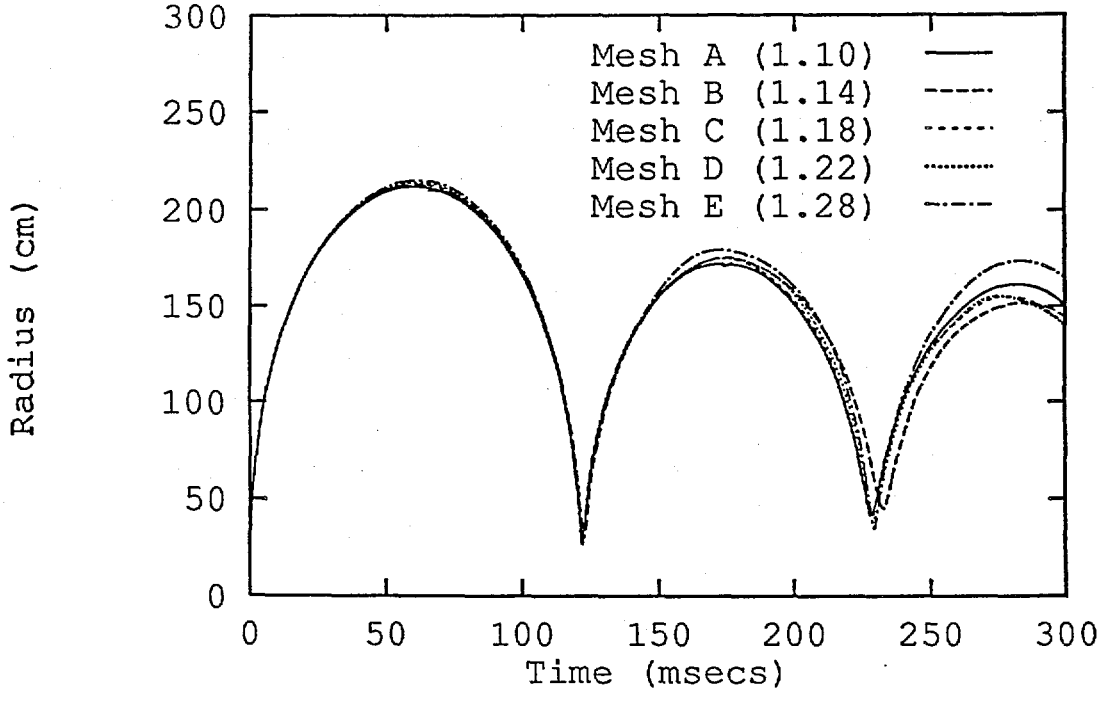

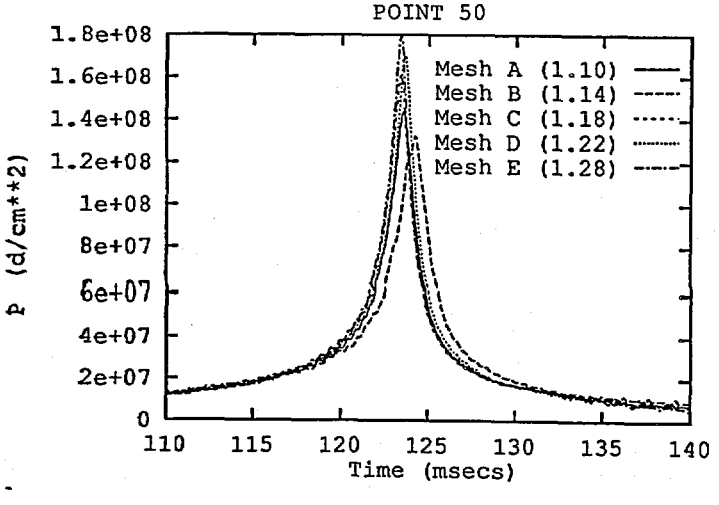

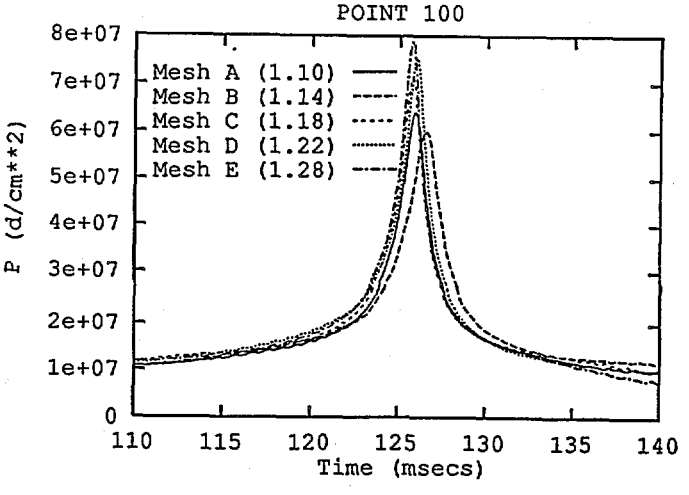

FIGURE C-1 COMPARISON OF THE 1–D SPHERICAL BUBBLE PERIODS AND PEAK PRESSURES ON THE MESH SEQUENCE OF TABLE C–1, WITH DIFFERENT OUTER REGION STRETCHING, AT A DEPTH OF 106.6m, SHORT PERIOD CASE, USING WALL BOUNDARY CONDITIONS

DISTRIBUTION

	Copies
DISTRIBUTION	
DOD ACTIVITIES (CONUS):	
DTIC	
CAMERON STATION	
ALEXANDRIA VA 22304-6145	12
ATTN: 33 (S. LEKOUDIS)	1
33 (G. MAIN)	1
33 (D. HOUSER)	1
OFFICE OF NAVAL RESEARCH	
BALLSTON TOWER 1	
800 NORTH QUINCY STREET	
ARLINGTON VA 22217-5660	
ATTN: SEA-03P3 (R. BOWSER)	1
SEA-03P33 (P. WU)	1
PMO-407 (W. HINCKLEY)	1
COMMANDER	
NAVAL SEA SYSTEMS COMMAND	
2531 JEFFERSON DAVIS HIGHWAY	
ARLINGTON VA 22242-5160	
ATTN: P7 (R. KAVETSKY)	1
40 (W. WASSMANN)	1
40E (E. JOHNSON)	1
40P (P. MARSHALL)	1
40P (P. MORRISON)	1
4140 (R. GARRETT)	1
4140 (R. GRANDE)	1
4140 (R. JONES)	1
420 (L. TAYLOR)	1
4201 (R. MCKEOWN)	1
4210 (D. TAM)	1
4210 (S. VAN DENK)	1
4220 (J. BURNS)	1
4220 (B. ALMQUIST)	1
4220 (D. BARBAZA)	1
4220 (D. BETANCOURT)	1
4220 (H. CHEN)	1
4220 (J. MCKIRGAN)	1
4220 (W. WALKER)	1
460 (H. HUANG)	1
4610 (H. MAIR)	1
4620 (M. MOUSSOUROS)	1
4620 (D. HAN)	1
4620 (K. KIDDY)	1
4630 (G. HARRIS)	1
904 (D. PHILLIPS)	1
911 (J. GOLDWASSER)	1
9210 (R. GUIRGUIS)	1
COMMANDER	
INDIAN HEAD DIVISION	
NAVAL SURFACE WARFARE CENTER	
SILVER SPRING MD 20903-5640	
ATTN: TECHNICAL LIBRARY	1
67.1 (B. WHANG)	1
67.1 (C. MILLIGAN)	1
67.1 (S. ZILLIACUS)	1
67.2 (G. WALDO)	1
COMMANDER	
CARDEROCK DIVISION	
NAVAL SURFACE WARFARE CENTER	
9500 MACARTHUR BLVD	
BETHESDA MD 20084-5000	
ATTN: TECHNICAL LIBRARY	1
6400 (J.P. BORIS)	1
6440 (M. EMERY)	1
NAVAL RESEARCH LABORATORY	
4555 OVERLOOK DR SW	
WASHINGTON DC 20375-5320	
ATTN: TECHNICAL LIBRARY	1
69SG (Y. KWON)	1
69SG (Y. SHIN)	1
SUPERINTENDENT	
NAVAL POSTGRADUATE SCHOOL	
MONTEREY CA 93940	
ATTN: TECHNICAL LIBRARY	1
SPSD (K. GOERING)	1
SPSD (D. BRUDER)	1
SPSD (M. GILTRUD)	1
DIRECTOR	
DEFENSE NUCLEAR AGENCY	
6801 TELEGRAPH RD.	
ALEXANDRIA VA 22310-3398	

DISTRIBUTION

	Copies
ATTN: MNMW (J. COLLINS)	1
MNMW (J. FOSTER)	1
WRIGHT LABORATORY	
EGLIN AFB FL 32542-5434	
ATTN: TECHNICAL LIBRARY	1
WT-PD (S. WILKERSON)	1
WT-TC (K. KIMSEY)	1
WT-TD (G. RANDERS-PEHRSON)	1
DIRECTOR	
U.S. ARMY RESEARCH LAB	
APG MD 21005-5066	
NON-DOD ACTIVITIES:	
CENTER FOR NAVAL ANALYSES	
4401 FORD AVENUE	
ALEXANDRIA VA 22302-0268	1
ATTN: GIFT AND EXCHANGE	4
LIBRARY OF CONGRESS	
WASHINGTON DC 20540	
ATTN: TECHNICAL LIBRARY	1
B216 (B.A. KASHIWA)	1
F663 (T. ADAMS)	1
J576 (M. LEWIS)	1
J576 (D. RABERN)	1
LOS ALAMOS NATIONAL LABORATORY	
PO BOX 1663	
LOS ALAMOS NM 87545	
ATTN: 1425 (S. ATTAWAY)	1
1431 (J.M. MCGLAUN)	1
1431 (E.S. HERTEL)	1
1432 (S. SILLING)	1
1542 (P. YARRINGTON)	1
7141 (TECHNICAL LIBRARY)	1
SANDIA NATIONAL LABORATORIES	
PO BOX 5800	
ALBUQUERQUE NM 87185-5800	

	Copies
ATTN: TECHNICAL LIBRARY	1
8742 (J.J. DIKE)	1
8742 (V. REVELLI)	1
8742 (L. WEINGARTEN)	1
SANDIA NATIONAL LABORATORIES	
PO BOX 969	
LIVERMORE CA 94551-0969	
ATTN: L-313 (LIBRARY)	1
L-35 (R. COUCH)	1
L-84 (K. ROSENKILDE)	1
LAWRENCE LIVERMORE NATIONAL LABORATORY	
PO BOX 808	
LIVERMORE CA 94550-0622	
ATTN: T. GEERS	1
MECHANICAL ENGINEERING	
UNIVERSITY OF COLORADO	
BOULDER CO 80309-0427	
ATTN: 0411 (D. BENSON)	1
DEPT OF AMES	
UNIVERSITY OF CALIFORNIA	
LA JOLLA CA 92093-0411	
ATTN: R. LHNER	1
GEORGE MASON UNIVERSITY	
FAIRFAX VA 22030-4444	
ATTN: T. BELYTSCHKO	1
MECHANICAL ENGINEERING	
NORTHWESTERN UNIVERSITY	
2145 SHERIDAN RD	
EVANSTON IL 60208-3111	
ATTN: T.J.R. HUGHES	1
MECHANICAL ENGINEERING	
STANFORD UNIVERSITY	
PALO ALTO CA 94306	
ATTN: A. PROSPERETTI	1
MECHANICAL ENGINEERING	
JOHNS HOPKINS UNIVERSITY	
BALTIMORE MD 21218	

DISTRIBUTION

	Copies
ATTN: J. STUHMILLER JAYCOR 11011 TORREYANA RD PO BOX 85154 SAN DIEGO CA 92138-9259	1
ATTN: K. KAN JAYCOR 1608 SPRING HILL RD VIENNA VA 22182-2270	1
ATTN: G.L. CHAHINE R. DURAISWAMI K.M. KALUMUCK DYNAFLOW INC 7210 PINDELL SCHOOL RD FULTON MD 20759	1 1 1
ATTN: J. DERUNTZ USA 19875 INDIAN SUMMER LANE MONUMENT CO 80132	1
ATTN: J. ENIG ENIG ASSOCIATES 11120 NEW HAMPSHIRE AVE SUITE 500 SILVER SPRING MD 20904-2633	1
ATTN: V. GODINO T. LITTLEWOOD A&T ENGINEERING TECH CENTER 240 ORAL SCHOOL RD SUITE 105 MYSTIC CT 06355-1208	1 1
ATTN: M. BARON R. ATKATSH R. DADDAZIO I. SANDLER R. SMILOWITZ WEIDLINGER ASSOCIATES 333 SEVENTH AV NEW YORK NY 10001	1 1 1 1 1
ATTN: K. STULTZ WEIDLINGER ASSOCIATES 1735 JEFFERSON DAVIS HWY SUITE 1002 ARLINGTON VA 22202	1
ATTN: G. JOHNSON ALLIANT TECHSYSTEMS INC MN11-2925 600 SECOND ST NE HOPKINS MN 554343	1
ATTN: J. HALLQUIST D. STILLMAN LSTC 2876 WAVERLEY WAY LIVERMORE CA 94550	1 1
ATTN: MS 2-3-1 (J. BAUM) SAIC 1710 GOODRIDGE DR MCLEAN VA 22102	1
ATTN: R. BRITT SAIC P O BOX 469 ST JOSEPH LA 71366-0469	1
ATTN: O. DENGEL ROUTE 1 BOX 200 FRONT ROYAL VA 22630	1
ATTN: D. CURTIS T. MOYER R. MILLER NKF ENGINEERING 4200 WILSON BLVD SUITE 900 ARLINGTON VA 22203-1800	1 1 1
ATTN: T. CULLY F. CHANG	1 1

DISTRIBUTION

	Copies
MACNEAL-SCHWENDLER CORP. 1000 HOWARD BLVD SUITE 105 MT LAUREL NJ 08054	
ATTN: K. FLORIE	1
MACNEAL-SCHWENDLER CORP GRONINGENWEG	6
2803 PV GOUDA THE NETHERLANDS	
ATTN: J. GREENHORN	1
R. HAXTON	1
DRA ST LEONARDS HILL DUNFERMLINE FIFE KY11 5PW SCOTLAND UNITED KINGDOM	
ATTN: I. CULLIS	1
DRA FT HALSTEAD SEVENOAKS KENT TN14 7BP ENGLAND UNITED KINGDOM	
ATTN: J. BLAKE	1
MATHEMATICS AND STATISTICS UNIVERSITY OF BIRMINGHAM EDGBASTON BIRMINGHAM BI5 2TT ENGLAND UNITED KINGDOM	
ATTN: D. RITZEL	1
DRE SUFFIELD BOX 4000 MEDICINE HAT ALBERTA T1A 8K6 CANADA	
ATTN: J.P.BEST	1
UNDERWATER SYSTEMS DIVISION MATERIALS RESEARCH LAB PO BOX 50 ASCOT VALE VIC 3032 AUSTRALIA	

	Copies
ATTN: P. CLASSEN	1
U. VOGEL	1
BMVG R T II 3 POSTFACH 1328 DW-53003 BONN 1 GERMANY	
ATTN: J. FREERCKS	1
BWB-SG14 POSTFACH 7360 D-56068 KOBLENZ 1 GERMANY	
ATTN: W. RYBAKOWSKI	1
WTD-71 BERLINERSTRASSE 115 D-24340 ECKERNFRDE GERMANY	
ATTN: MOD/WSB (W. KANOLD)	1
TA (W. PFRANG)	1
TA (W. MOHR)	1
TAF (H.J. DIEKHOFF)	1
TAF (U. ANDELFINGER)	1
TAF (M. BORRMANN)	1
TAF (H. MADER)	1
TAF (B. FIESSLER)	1
TAF (R. CHWALINSKI)	1
TAF (E. WACHSMANN)	1
IABG EINSTEINSTRASSE 20 D-85521 OTTOBRUNN GERMANY	
INTERNAL:	
E231	2
E232	3
E29L	2
B44 (T.F. ZIEN)	1
B44 (J.P. COLLINS)	1
B44 (F. PRIOLO)	1
B44 (W. SZYMCZAK)	1
B44 (A. WARDLAW)	10

REPORT DOCUMENTATION PAGE

Form Approved OMB No. 0704-0188

1. AGENCY USE ONLY *(Leave blank)*	2. REPORT DATE	3. REPORT TYPE AND DATES COVERED

4. TITLE AND SUBTITLE
Far Field Boundary Conditions for Underwater Explosions

5. FUNDING NUMBERS

6. AUTHOR(S)
A. B. Wardlaw

7. PERFORMING ORGANIZATION NAME(S) AND ADDRESS(ES)
Naval Surface Warfare Center
Dahlgren Division, White Oak Detachment
10901 New Hampshire Avenue

8. PERFORMING ORGANIZATION REPORT NUMBER
NSWCDD/TR-94/20

9. SPONSORING/MONITORING AGENCY NAME(S) AND ADDRESS(ES)

10. SPONSORING/MONITORING AGENCY REPORT NUMBER

11. SUPPLEMENTARY NOTES

12a. DISTRIBUTION/AVAILABILITY STATEMENT
Approved for public release; distribution is unlimited.

12b. DISTRIBUTION CODE

13. ABSTRACT *(Maximum 200 words)*

This work investigates a far field boundary condition (FFBC) designed to suppress the reflection of shocks and other waves from the outer computational boundaries. The general form of this condition is based on characteristic analysis and is based on a nonreflecting formulation in conjunction with an asymptotic analysis. The FFBC has been implemented in the DYSMAS code and applied to underwater explosion problems; both the short-term shock phase and the long-term bubble pulse problems are considered. Excellent results were obtained for shock problems in 1, 2, and 3 dimensions. The performance of these boundary conditions were mixed for the bubble pulse application with best results being obtained for relatively short periods, deep explosions, computed in multiple dimensions. It is concluded that the maximum mesh reduction in the bubble case is achieved when the far field boundary conditions are used in conjunction with a stretched mesh.

14. SUBJECT TERMS

15. NUMBER OF PAGES

16. PRICE CODE

17. SECURITY CLASSIFICATION OF REPORT	18. SECURITY CLASSIFICATION OF THIS PAGE	19. SECURITY CLASSIFICATION OF ABSTRACT	20. LIMITATION OF ABSTRACT
UNCLASSIFIED	UNCLASSIFIED	UNCLASSIFIED	SAR

GENERAL INSTRUCTIONS FOR COMPLETING SF 298

The Report Documentation Page (RDP) is used in announcing and cataloging reports. It is important that this information be consistent with the rest of the report, particularly the cover and its title page. Instructions for filling in each block of the form follow. It is important to ***stay within the lines*** to meet ***optical scanning requirements***.

Block 1. Agency Use Only *(Leave blank)*.

Block 2. Report Date. Full publication date including day, month, and year, if available (e.g. 1 Jan 88). Must cite at least the year.

Block 3. Type of Report and Dates Covered. State whether report is interim, final, etc. If applicable, enter inclusive report dates (e.g. 10 Jun 87 - 30 Jun 88).

Block 4. Title and Subtitle. A title is taken from the part of the report that provides the most meaningful and complete information. When a report is prepared in more than one volume, repeat the primary title, add volume number, and include subtitle for the specific volume. On classified documents enter the title classification in parentheses.

Block 5. Funding Numbers. To include contract and grant numbers; may include program element number(s), project number(s), task number(s), and work unit number(s). Use the following labels:

C	- Contract	**PR**	- Project
G	- Grant	**TA**	- Task
PE	- Program Element	**WU**	- Work Unit Accession No.

BLOCK 6. Author(s). Name(s) of person(s) responsible for writing the report, performing the research, or credited with the content of the report. If editor or compiler, this should follow the name(s).

Block 7. Performing Organization Name(s) and Address(es). Self-explanatory.

Block 8. Performing Organization Report Number. Enter the unique alphanumeric report number(s) assigned by the organization performing the report.

Block 9. Sponsoring/Monitoring Agency Name(s) and Address(es). Self-explanatory.

Block 10. Sponsoring/Monitoring Agency Report Number. *(If Known)*

Block 11. Supplementary Notes. Enter information not included elsewhere such as: Prepared in cooperation with...; Trans. of...; To be published in.... When a report is revised, include a statement whether the new report supersedes or supplements the older report.

Block 12a. Distribution/Availability Statement. Denotes public availability or limitations. Cite any availability to the public. Enter additional limitations or special markings in all capitals (e.g. NOFORN, REL, ITAR).

DOD	- See DoDD 5230.24, "Distribution Statements on Technical Documents."
DOE	- See authorities.
NASA	- See Handbook NHB 2200.2
NTIS	- Leave blank.

Block 12b. Distribution Code.

DOD	- Leave blank.
DOE	- Enter DOE distribution categories from the Standard Distribution for Unclassified Scientific and Technical Reports.
NASA	- Leave blank.
NTIS	- Leave blank.

Block 13. Abstract. Include a brief ***(Maximum 200 words)*** factual summary of the most significant information contained in the report.

Block 14. Subject Terms. Keywords or phrases identifying major subjects in the report.

Block 15. Number of Pages. Enter the total number of pages.

Block 16. Price Code. Enter appropriate price code ***(NTIS only)***

Blocks 17.-19. Security Classifications. Self-explanatory. Enter U.S. Security Classification in accordance with U.S. Security Regulations (i.e., UNCLASSIFIED). If form contains classified information, stamp classification on the top and bottom of the page.

Block 20. Limitation of Abstract. This block must be completed to assign a limitation to the abstract. Enter either UL (unlimited) or SAR (same as report). An entry in this block is necessary if the abstract is to be limited. If blank, the abstract is assumed to be unlimited.


UNITED STATES NAVY
SURFACE WARFARE CENTER